



Annual Report 2016

MLZ is a cooperation between:

Bayerisches Staatsministerium für
Bildung und Kultus, Wissenschaft und Kunst



SPONSORED BY THE



Federal Ministry
of Education
and Research

The Heinz Maier-Leibnitz Zentrum (MLZ):

The Heinz Maier-Leibnitz Zentrum is a leading centre for cutting-edge research with neutrons and positrons. Operating as a user facility, the MLZ offers a unique suite of high-performance neutron scattering instruments. This cooperation involves the Technische Universität München, the Forschungszentrum Jülich and the Helmholtz-Zentrum Geesthacht. The MLZ is funded by the German Federal Ministry of Education and Research, together with the Bavarian State Ministry of Education, Science and the Arts and the partners of the cooperation.

The Forschungs-Neutronenquelle Heinz-Maier-Leibnitz (FRM II):

The Forschungs-Neutronenquelle Heinz-Maier-Leibnitz provides neutron beams for the scientific experiments at the MLZ. The FRM II is operated by the Technische Universität München and is funded by the Bavarian State Ministry of Education, Science and the Arts.

Joint Annual Report 2016
of the MLZ and FRM II



A solid base for the future

Ten different universities investing in neutron and positron research at the MLZ were successful in their collaborative projects. The German Federal Ministry of Education and Research (BMBF) has allocated 13.5 million Euros for method and instrument development to be realized over the next three years by our university partners, including seven projects involving the participation of the Technical University of Munich (TUM), and four the participation of the Jülich Centre for Neutron Science (JCNS). The Ministry will also support the integration of instruments in the new Neutron Guide Hall East to the tune of 2.7 million Euros.

Several other MLZ projects received funding from the German research foundation DFG in 2016, the most prominent being the “Creation of intense positron pulses on NEPOMUC”. The University of Greifswald, the Max Planck Institute for Plasma Physics, and the TUM will team up to develop a device to accumulate and store positrons and deliver these in pulses of unprecedented intensity.

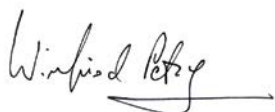
After almost ten years working with the neutron source, administrative director Klaus Seebach retired in December and passed the baton on to Johannes Nußbickel. Klaus Seebach’s tenure began with the most important financial project, the MLZ cooperation’s design and contract, but he also managed the administration of the FRM II as well as maintaining excellent contacts with industrial partners and other neutron centres in Europe. We would like to thank him for his indefatigable efforts and wish him all the best for his retirement. We extend a warm welcome to his successor, Johannes Nußbickel, who has a distinguished background in industry, having been responsible for the finance and administration of mid-sized companies in the technology sector.

The MLZ is, and will continue to be, a full service provider for neutrons and positrons. With the foreseeable closure of ORPHÉE, France, and BER II, Germany, in late 2019, the European neutron landscape will change dramatically. The MLZ is prepared to assume the added responsibility for the neutron user community resulting from these regrettable developments. In order to salvage the BER II instruments for the national and international user community, the MLZ is currently exploring the possibility of transferring the excellent, and in most cases brand new, instruments from BER II to MLZ. Such a transfer of know-how and high-quality instrumentation has already been achieved some years ago, when DIDO in Jülich as well as FRG-2 in Geesthacht were shut down. This serves as a blueprint for a potential instrument transfer from BER II. The task is challenging, but is being well planned in collaboration with the HZB.

An important milestone in the quest to extend our capacity was reached in April this year by the exchange of the beam plug of SR5, enabling three thermal neutron beams to be guided into the future Neutron Guide Hall East. The foundation-laying ceremony for our two new office, laboratory and workshop buildings in early 2017 is another step towards an expansion – in both staff and know-how. The move-in is anticipated for 2019.

Three full cycles of neutrons are planned for 2017. At the end of the year we will exchange another beam plug, at beam tube number SR 6a, in preparation for the future installation of the ultra-cold neutron source UCN.

The long-term perspective of the MLZ will deliver competence and support for our German and international users. You will find many examples of outstanding experimental results in the newly designed chapters “Scientific Highlights” and “Scientific Reports” of this Annual Report, as well as information on our advanced instrumentation.



Winfried Petry



Thomas Brüchel



Johannes Nußbickel



Anton Kastenmüller

Scientific Highlights

Exploring the origin of high-temperature superconductivity.....	10
A complete survey of copper selenate.....	10
Pathways in 3D for future battery materials.....	11
Inhomogeneities in lithium-ion batteries	11
Spin liquids show order in chaos	12
Looking inside ice clouds.....	12
Safer underground storage of carbon dioxide	13
Motion pattern of large molecules	13

Scientific Reports

Materials Science

Field-induced self-assembly of iron oxide nanoparticles	14
Isothermal transformation kinetics in the research reactor fuel candidate U–8wt%Mo	15
Self-diffusion in amorphous silicon probed by neutron reflectometry	16
Determination of impurities in multi-crystalline solar silicon	17
Defect spectroscopy with positrons supports kinetic barriers in NMC-type electrodes	18
Migration of Ni atoms on Pd observed by the positron annihilation induced Auger process	19
Mechanical properties of multiferroic $\text{Bi}_2\text{Mn}_4\text{O}_{10}$ determined by inelastic neutron scattering	20

Quantum Phenomena

Antiphase boundaries in CaFe_2O_4 probed with polarized neutron diffuse scattering	21
Transition from sign-reversed to sign-preserved cooper-pairing symmetry in $\text{K}_x\text{Fe}_{2-y}(\text{Se}_{1-z}\text{S}_z)_2$	22
Effect of nematic order on the low-energy spin fluctuations in $\text{BaFe}_{1.935}\text{Ni}_{0.065}\text{As}_2$	23
SANS study of vortex lattice structural transition in optimally doped $(\text{Ba}_{1-x}\text{K}_x)\text{Fe}_2\text{As}_2$	24
Magnetic excitations of strongly dimerized quantum magnet $\text{BaCu}_2\text{V}_2\text{O}_8$	25
Spin waves in full-polarized state of Dzyaloshinskii-Moriya helimagnets: A SANS study.....	26
Suppression of spin-exciton state in hole overdoped iron-based superconductors	27
Impact of uniaxial stress on structural transitions of iron pnictides.....	28

Soft Matter

Thermal activation of large-scale motions in a eukaryotic lactate dehydrogenase	29
Water dynamics in <i>Shewanella oneidensis</i> at ambient and high pressure using QENS.....	30
Aqueous solutions of poly(ethylene oxide) — from ordinary to tricritical behavior	31
Disintegration of beech wood with ionic liquid/water mixtures.....	32
Self-assembled nanoparticles from weakly amphiphilic triblock copolymers as drug carriers	33
Combining the strengths of neutrons and molecular dynamics for the study of biomembranes	34
Study on self-assembly of diblock copolymer–maghemite nanoparticle hybrid thin films	35

Structure Research

Concentration and distribution of oxygen interstitials in an electrolyte	36
Phase diagram of Eu magnetic ordering in Sn-flux-grown $\text{Eu}(\text{Fe}_{1-x}\text{Co}_x)_2\text{As}_2$ single crystals	37
Low-temperature commensurately modulated structure of the multiferroic melilite $\text{Ca}_2\text{CoSi}_2\text{O}_7$	38
Old data, new methods — discovering lithium diffusion pathways in $\gamma\text{-LiAlO}_2$ single-crystals	39
On the complex H-bonding network in hureaulite, $(\text{Mn,Fe})_5(\text{PO}_4)_2(\text{HPO}_4)_2(\text{H}_2\text{O})_4$	40

Neutron Methods

Studying the micrometer range by means of neutron imaging	41
TISANE @ SANS-1: Kinetics with μs time resolution	42
Determination of radiative thermal neutron capture cross sections for low-Z isotopes	43
First spatially-resolved positron annihilation lifetime measurements at NEPOMUC	44

Instrumental Upgrades & Services

News from the instruments	48
Support for MLZ from Jülich: engineering and electronics	56
When the instruments operate smoothly	60
Exchanging the plug JMA05 in the beam tube SR5 at FRM II	66

Reactor & Industry

Operating, enhancing and maintaining the FRM II in 2016	72
Fabrication of monolithic U-Mo plates for the EMPIRE experiment	74
The Ultra-Cold Neutron Source at the FRM II begins its non-nuclear test phase	76

Facts & Figures

The year in pictures	80
Workshops, Conferences and Schools	84
Awards	86
From science to media: the public relations office	88
The year from the User Office's point of view	90
Staff	94
Budget	95
Publications & Theses	96
Partner institutions	104
Imprint	108

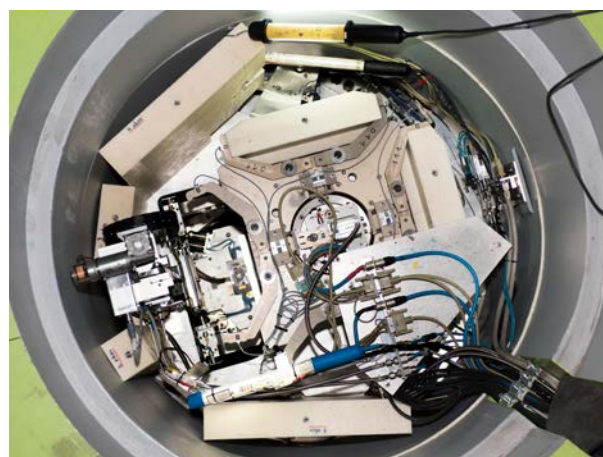
Where the neutrons come from: A look inside the beam guide of the Medical Application instrument MEDAPP and neutron tomography station NECTAR.



Scientific Highlights & Reports

Exploring the origin of high-temperature superconductivity

Since the discovery of high temperature superconductivity, researchers have tried to find out why these materials already become superconducting at comparatively high temperatures. They all show neutron spin resonance, which is a collective magnetic excitation that appears in the unconventional copper oxide, iron pnictide and heavy fermion superconductors below the critical temperature. But what is the reason for this behavior? Inelastic neutron scattering at PANDA turned out to be a convenient method for studying this resonance behavior, and showing how the magnetic resonance of the material develops and acts at the critical point where superconductivity occurs. In most common superconductors, magnetism suppresses superconductivity. An international team compared the neutron scattering data with a random phase approximation calculation of the electronic structure and the results from scanning tunneling microscopy and was able to show that, to the contrary, it seems that magnetic fluctuations resembling those in ordered magnets appear to be essential for superconductivity.

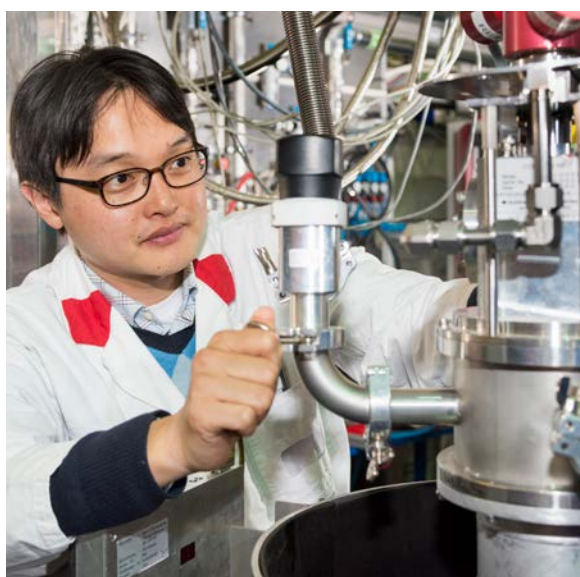


The three axes spectrometer PANDA showed, how the magnetic resonance of the material developed.

Y. Song, J. Van Dyke, I. K. Lum, B. D. White, S. Jang, D. Yazici, L. Shu, A. Schneidewind, P. Čermák, Y. Qiu, M. Brian Maple, Dirk K. Morr, and P. Dai; Robust upward dispersion of the neutron spin resonance in the heavy fermion superconductor $Ce_{1-x}Yb_xCoIn_5$, Nature Communications 7, 12774 (2016)

A complete survey of copper selenate

Chiral magnets are of huge interest not only for basic research, but also for future application in alternative magnetic data storage. A competition between multiple magnetic interactions typically governs the complex low-temperature ordered states in chiral magnets. The chiral-lattice multiferroic Cu_2OSeO_3 is recognized as the first insulating helimagnetic material in which a long-range order of topologically stable spin vortices, known as skyrmions, was established. For the first time, state-of-the-art inelastic neutron scattering (INS) at the instruments PUMA and PANDA has been employed to comprehend the full three-dimensional spin excitation spectrum of Cu_2OSeO_3 over a broad range of energies. Distinct types of high- and low-energy dispersive magnon modes separated by an extensive energy gap are observed, in excellent agreement with a previously suggested microscopic theory based on a model of entangled Cu_4 tetrahedra. A comparison of the INS data with model spin-dynamical calculations based on these theoretical proposals allows for an accurate quantitative verification of the fundamental magnetic interactions in copper selenate that are essential to an understanding of its abundant low-temperature magnetically ordered phases.



For the first time, Jitae Park and colleagues employed inelastic neutron scattering at PANDA and PUMA for the full three-dimensional spin excitation spectrum of copper selenate.

P. Y. Portnichenko, J. Romhányi, Y. A. Onyikienko, A. Henschel, M. Schmidt, A. S. Cameron, M. A. Surmach, J. A. Lim, J. T. Park, A. Schneidewind, D. L. Abernathy, H. Rosner, J. van den Brink, and D. S. Inosov; Magnon spectrum of the helimagnetic insulator Cu_2OSeO_3 , Nature Communications 7, 10725 (2016)



Pathways in 3D for future battery materials

The discovery of the lithium superionic conductor $\text{Li}_{10}\text{GeP}_2\text{S}_{12}$ triggered new groundbreaking research in the field of all solid-state batteries. Many reports have described the modification of the material in order to increase the ionic conductivity. However, despite the advances in controlling the ionic conductivity and even finding new compositions within this structure type, the underlying ion dynamics are still not clear. Neutron powder diffraction at SPODI, in combination with analyses of differential bond valence and nuclear density maps, elucidated the underlying diffusion pathways in $\text{Li}_{10}\text{GeP}_2\text{S}_{12}$. It shows quasi-isotropic three-dimensional pathways, which is a combination of one-dimensional diffusion channels crossing two diffusion planes. Furthermore, sound measurements at ultrasonic speeds are used to understand the lattice dynamics. Temperature dependent X-ray diffraction is performed in order to understand the temperature-dependent behavior of the prevalent structural backbone, as well as the thermal stability of the material. At elevated temperatures, the superionic conducting phase partially decomposes into $\text{Li}_4\text{P}_2\text{S}_6$, explaining the deterioration in the ionic conductivity upon heating.



Neutron powder diffraction elucidated the ion dynamics in a lithium superionic conductor suitable for batteries.

D. A. Weber, A. Senyshyn, K. S. Weldert, S. Wenzel, W. Zhang, R. Kaiser, S. Berendts, J. Janek, and W. G. Zeier; Structural Insights and 3D Diffusion Pathways within the Lithium Superionic Conductor $\text{Li}_{10}\text{GeP}_2\text{S}_{12}$; Chem. Mater. 28, 5905 (2016)

Inhomogeneities in lithium-ion batteries

Everyday, billions of lithium-ion batteries store electrical charge, relaying it back and forth. Despite the rather simple principle underlying this operation, some background processes affecting battery operation are not yet under complete control, e.g. loss of capacity upon extensive cycling, safety, temperature stability etc. Neutrons are an effective, non-destructive probe for in operando studies on standard size lithium-ion batteries under real operating conditions and beyond. Recent spatially-resolved neutron powder diffraction, electrochemical measurements and X-ray computed tomography unambiguously revealed variations of the lithium distribution in the graphite anode. Consequently, specific regions in the cells undergo more extensive ion-exchange than others, potentially leading to spatial differences in local fatigue. The spatial profile of Li concentration obtained points directly to the electrical current distribution as a key parameter defining cell performance. Improved use of the applied electrode materials can increase the effective cell capacity and, thus, result in more uniform fatigue and extended cycle life.

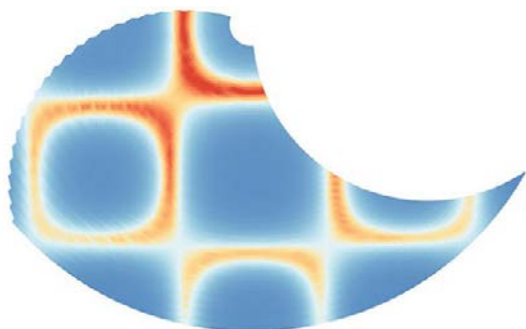
A. Senyshyn, M. J. Mühlbauer, O. Dolotko, M. Hofmann, and H. Ehrenberg, Homogeneity of lithium distribution in cylinder-type Li-ion batteries; Scientific Reports 5, 18380 (2015)



Martin Mühlbauer (left) and Anatoliy Senyshyn used spatially-resolved neutron powder diffraction at STRESS-SPEC in combination with electrochemical measurements and X-ray computed tomography to probe lithium distribution in lithium-ion batteries non-destructively.

Spin liquids show order in chaos

Correlated paramagnets follow a special pattern as far as their spin fluctuations are concerned. Usually, if they enter some long-range ordered state at low temperature, the ordered state can be extremely susceptible to external forces. A new type of correlated paramagnet state, the spiral spin-liquid, in which spins fluctuate collectively as spirals, has recently been theoretically predicted to exist.



This simulation of the scattering intensities illustrates impressively the spiral order in chaos of a spin liquid.

In the spiral spin-liquid, the ground states are a massively degenerated set of coplanar spin spirals. Using the diffuse scattering neutron time-of-flight spectrometer (DNS) at the MLZ, the spiral surface in MnSc_2S_4 was directly observed, which provides evidence for the existence of the spiral spin-liquid state. Moreover, neutron diffraction experiments illustrated the multi-step ordering behavior in MnSc_2S_4 and demonstrated a new way to realize a magnetic vortex lattice through frustrated interactions.

S. Gao, O. Zaharko, V. Tsurkan, Y. Su, J. S. White, G. S. Tucker, B. Roessli, F. Bourdarot, R. Sibille, D. Chernyshov, T. Fennell, A. Loidl, and C. Rüegg, Spiral spin-liquid and the emergence of a vortex-like state in MnSc_2S_4 , Nature Physics 13, 157 (2017)

Looking inside ice clouds

Ice clouds in the lower stratosphere (15-20 km altitude) play an important role in the radiation balance of our planet, exerting a strong influence on the climate, or on ozone depletion at the polar caps.

The particles inside these clouds consist primarily of water ice and nitric acid trihydrate (NAT): the latter can assume either an alpha- or beta-form. The research group focused on the alpha form of the hydrate, which is only temporarily stable. Using the powder diffractometer SPODI, they were the first to fully understand the structure of this alpha-NAT.

Since the beta-hydrate is present in the atmosphere at the end of the ice cloud formation, they also studied the phase transition and found the beta form with a similar volume, but a more symmetric structure than the alpha. This was the first proof of the independent existence of the alpha-NAT. As long as enough ice is available, the alpha is always produced first. This metastable form only exists between $-85\text{ }^\circ\text{C}$ and $-73\text{ }^\circ\text{C}$ if the alpha crystals are in contact with ice and slowly changes into the beta form. It has a high affinity to water ice, which plays a crucial role when it comes to the formation of ice clouds.



Cirri, the ice clouds in the upper troposphere (8-12 km high) look like teased cotton wool.

F. Weiss, F. Kubel, O. Gálvez, M. Hölzel, S. F. Parker, P. Baloh, R. Iannarelli, M. J. Rossi, and H. Grothe, Metastable Nitric Acid Trihydrate in Ice Clouds, Angewandte Chemie International Edition 55, 3276 (2016)

Safer underground storage of carbon dioxide

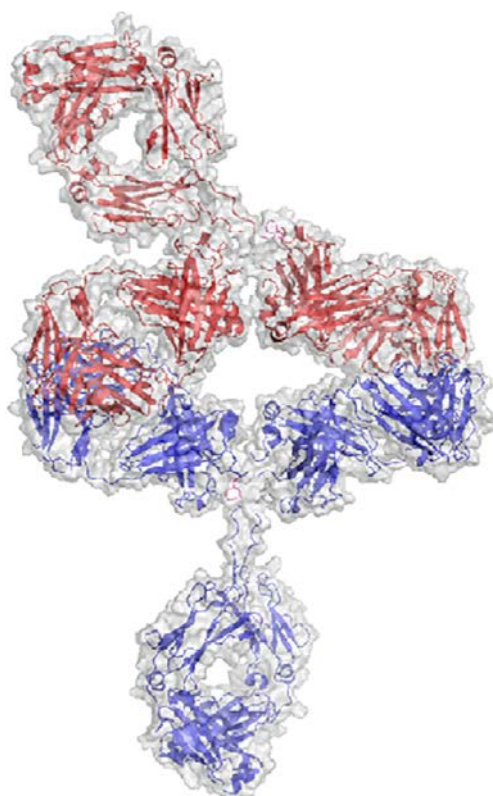
The long-term storage of carbon dioxide in porous layers of rock deep underground (carbon capturing and storage, CCS) could contribute to a reduction in the emission of climate-damaging gases in the atmosphere. Storage of CO₂ in porous rock layers deep underground is a favoured solution. However, before this can be achieved, there are many questions to be answered - above all, how long CO₂ can remain stored in the rock. Thick layers of non-porous stone should prevent leakage, but the question is, how long will they resist the acidic solutions of the liquefied gas? In the case of a natural reservoir in Utah, current experiments have found the top layer to be stable for at least 100,000 years, or ten times as long as once thought. An international research team investigating the pore network structure of a natural 100,000-year-old carbon dioxide (CO₂) reservoir in Utah, USA, has shown, with the help of small angle neutron scattering at the KWS-1 and KWS-3 instruments, that carbon dioxide dissolved in water remains stored in certain types of rock layers far longer than first envisaged.



The rocks in the Colorado Plateau, USA, are representative of reservoirs currently under consideration for CO₂ storage in Europe.

N. Kampman, A. Busch, P. Bertier, J. Snippe, S. Hangx, V. Pipich, Z. Di, G. Rother, J. F. Harrington, J. P. Evans, A. Maskell, H. J. Chapman, and M. J. Bickle; Observational evidence confirms modelling of the long-term integrity of CO₂-reservoir caprocks, Nature Communications 7, 12268 (2016)

Motion pattern of large molecules



Immunoglobulin G1 with Fc and Fab domains.

Antibodies are large Y-shaped glycoproteins consisting of three fragments of equal size (see Fig.) connected by a flexible linker region: two antigen-binding fragments (Fab) and one constant fragment (Fc). Variations in the Fc fragment distinguish the five major classes of immunoglobulins (Ig). It is very difficult to explore antibody activity in solution, since most investigative methods require a predefined fixed structure. The functions of biological active molecules rely on their ability to change the structure. They can only move in solution and these movements are tiny (small amplitude) and very fast. Neutron Spin Echo Spectroscopy at JNSE was able to follow the motion of the antibodies of different fragments on a timescale of 7 ns, with motional amplitudes of 1 nm relative to each other. It is a real challenge to determine what types of intramolecular motions are observed and to relate these motions to overall functionality. A detailed study of human IgG domain motions in a protein solution has now succeeded in resolving the motional pattern in space and time.

L. R. Stingaciu, O. Ivanova, M. Ohl, R. Biehl, and D. Richter, Fast antibody fragment motion: flexible linkers act as entropic spring; Scientific Reports 6, 22148 (2016)

Z. Fu¹, Y. Xiao², A. Feoktystov¹, V. Pipich¹, M.-S. Appavou¹, Y. Su¹, E. Feng¹, W. T. Jin¹, T. Brückel²¹Jülich Centre for Neutron Science (JCNS) at MLZ, Forschungszentrum Jülich GmbH, Garching, Germany; ²JCNS-2, PGI-4: Scattering Methods, Forschungszentrum Jülich GmbH, Jülich, Germany

The magnetic-field-driven self-assembly of magnetic nanoparticles (NPs) provides a fast, bottom-up strategy for the production of functional nanostructures and model systems. Iron oxide NPs are currently attracting wide interest due to their ease of preparation, low cost, high chemical stability, and tunable magnetic and surface properties. It is highly desirable to study the field-induced self-assembly of iron oxide NPs from both a fundamental and applicational point of view.

The magnetic NP sample used for the present work is a commercial iron oxide NP solution. Each magnetic NP consists of an iron oxide core and an oleic acid shell. As revealed by the TEM measurements, the NPs are spherical in shape and relatively uniform in size. The average core diameter is estimated to be around 17.1 nm. XRD and magnetization results suggest that the iron oxide core is composed mainly of maghemite.

Small-angle neutron scattering (SANS) investigations were carried out on KWS-1 at the MLZ. The radially averaged SANS intensity is fitted with the model for a core-shell spherical object. The radius of the core and the thickness of the shell are determined as 8.5 nm and 1.5 nm, respectively. The SANS patterns collected at various fields are shown in the figure. Upon applying a field of 0.1 T, distinct Bragg

peaks appear, demonstrating the formation of a single-crystalline-like superstructure. When the field is increased from 0.1 to 2.2 T, the crystallinity of the NPs self-assembly is improved, as indicated by the increased sharpness of the high-order diffraction spots, allowing a reliable inspection of the crystal structure. In Fig. 1f, the SANS pattern measured at 2.2 T agrees well with the theoretical diffraction pattern (white circles) calculated for face-centred cubic (FCC) supercrystals, clearly suggesting that the crystal structure of the field-induced self-assembly is FCC. By means of very-small-angle neutron scattering measurements using the KWS-3 at the MLZ, we have found that large-scale aggregates with radii of several hundreds of nanometers or more develop rapidly when the field increases from 0.005 to 0.2 T.

In conclusion, we have investigated the field-induced self-assembly of core-shell iron oxide NPs by means of SANS. The long-range well-ordered self-assembly of iron oxide NPs has been achieved when sufficient magnetic field is applied. The crystal structure of the NPs' self-assembly is FCC.

Z. Fu et al., Field-induced self-assembly of iron oxide nanoparticles investigated using small-angle neutron scattering; Nanoscale 8, 18541 (2016)

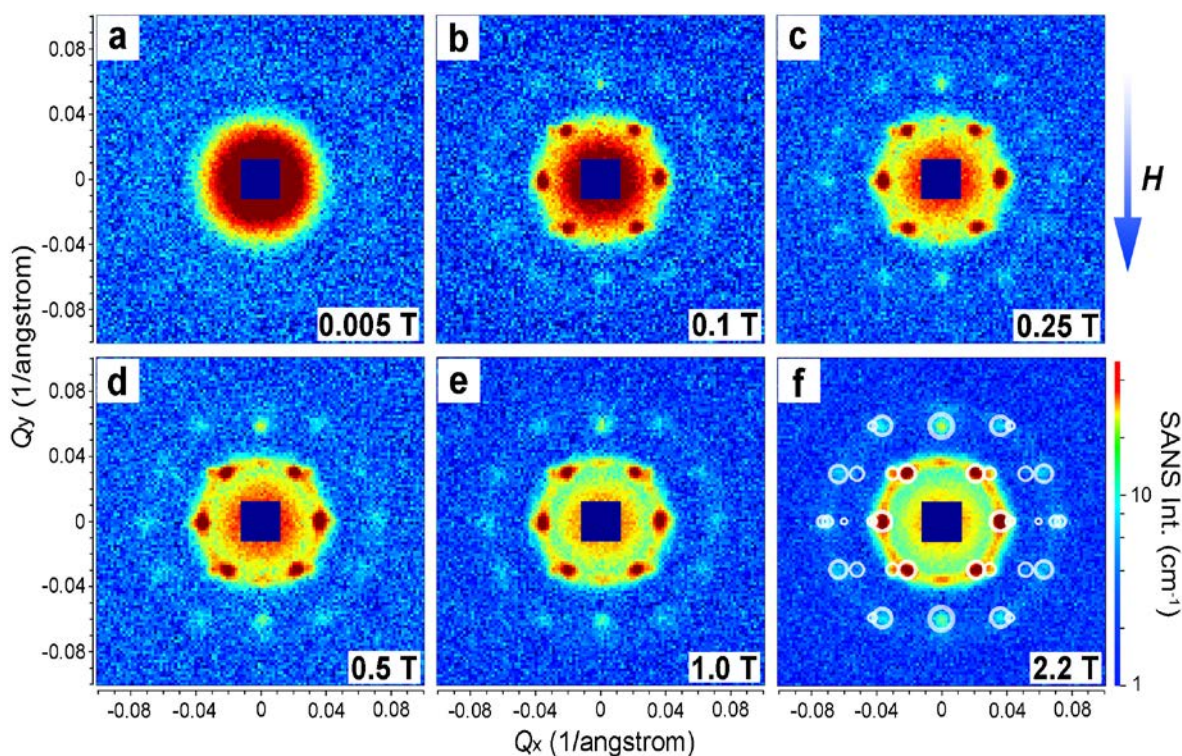


Figure 1: SANS patterns measured from iron oxide NPs solution exposed to external magnetic fields of 0.005 T (a), 0.1 T (b), 0.25 T (c), 0.5 T (d), 1 T (e), and 2.2 T (f). In (f), the calculated reflections for a face-centred cubic structure are shown as white circles and superimposed onto the experimental pattern for comparison.

S. Säubert^{1,2}, R. Jungwirth¹, T. Zweifel¹, M. Hofmann¹, M. Hoelzel¹, W. Petry¹
¹Heinz Maier-Leibnitz Zentrum (MLZ), Technische Universität München, Garching, Germany; ²Physik-Department, Technische Universität München, Garching, Germany

In order to reduce the amount of highly enriched uranium (HEU) in the civilian nuclear fuel cycle, efforts are being made to develop a fuel with a higher uranium density, which would allow the conversion of research and test reactors from HEU to lower enriched uranium (LEU) while maintaining an equivalent neutron flux and quality. Since the uranium compounds currently in use such as U_3Si_2 and UAl_x do not provide the uranium density required to convert high-performance research reactors, a new fuel must be developed. Pure metallic uranium, which would offer the highest uranium density possible, is known to show unfavourable behaviour during irradiation to high burn-up. Only the bcc γ -phase of uranium has properties adequate for use as a nuclear fuel. UMo alloys with 8-10wt % Mo content retain this phase in a metastable state at room temperature and have sufficient uranium density. These alloys are currently the subject of interest among the international research reactor fuel-developing community.

Nevertheless, the high temperatures to which the UMo alloy is exposed during the manufacturing process of the fuel element may lead to a decomposition of the γ -UMo phase into its thermal equilibrium microstructures, i.e. α -U and U_2Mo . Although it has been shown that the decomposition is reversed during in-pile irradiation, it is preferable to avoid it during fuel plate production. Therefore, the precise kinetics of the γ -UMo phase decomposition as a function of temperature and annealing time need to be understood.

Both neutron and X-ray diffraction studies at room temperature were performed on annealed UMo samples to obtain detailed crystallographic information on the state of decom-

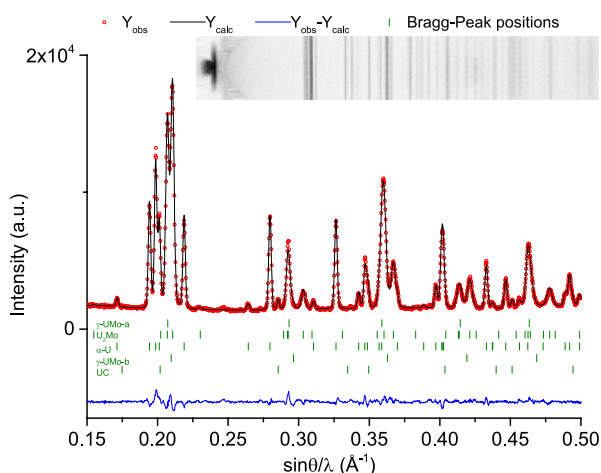


Figure 1: Neutron diffraction pattern for an U-8wt%Mo sample annealed at 748 K for 48 h with the diffraction image (inset). Red circles indicate the measured data, green dashes the Bragg peak positions, the black line the calculated pattern, and the blue line the difference between the calculated pattern and the measured data.

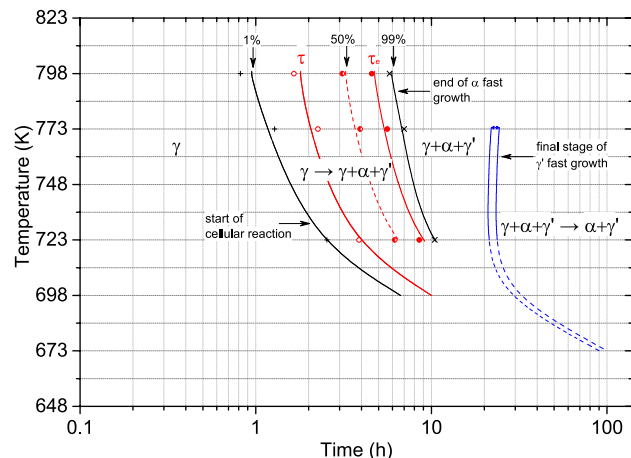


Figure 2: Isothermal transformation diagram of U-8wt%Mo: start of the cellular reaction where γ -UMo starts to transform into α -U and U_2Mo (γ'), the end of the α -U phase fast growth, the final stage of the U_2Mo fast growth (blue lines), and the region where the remaining γ -UMo slowly vanishes as the α -U and U_2Mo phases increase with a linear-like behaviour. The α -U phase growth can be described in more detail: 1 %, 50 %, 99 % of the fast growth; nucleation period τ (i.e. 10 %) and end of nucleation τ_e (i.e. 90 %).

position as a function of annealing time and temperature. A Rietveld refined diffraction pattern is shown in Fig. 1. The pattern was taken after annealing at 748 K for 48 h, where the decomposition is already at an advanced stage and most of the γ -UMo has decomposed. Additionally, *in situ* annealing studies using neutron diffraction were used for the investigation of the evolution of the Bragg peak intensity and, hence, the transformation kinetics of single phases.

The final isothermal transformation diagram is shown in Fig. 2. The data show the strong temperature dependence of the onset of phase decomposition (shown by the 1 % line) and the transformation itself. Depending on the reaction temperature, the beginning of the transformation, described by the α -U phase growth, is accompanied by the formation of U_2Mo (γ' -phase). However, at intermediate and low temperatures, below 750 K, the latter is delayed and the onset of the phase transformation is described solely by the α -U phase growth. The results of this work contain detailed information on the decomposition of the γ -UMo phase during temperature treatment and, hence, are vital for the manufacturing process of UMo fuel plates and the behaviour of the fuel during reactor operation. It has been shown which time-temperature regions must be avoided and where it is possible to manufacture the fuel element without risking immediate decomposition.

S. Säubert et al., Neutron and hard X-ray diffraction studies of the isothermal transformation kinetics in the research reactor fuel candidate U-8 wt%Mo; *J. Appl. Cryst.* 49, 923 (2016)

F. Strauß^{1,2}, S. Mattauch³, A. Koutsoubas³, J. Stahn⁴, T. Geue⁴, H. Schmidt^{1,2}

¹Mikrokinetics Group, Institute of Metallurgy, TU Clausthal, Clausthal-Zellerfeld, Germany; ²Clausthaler Zentrum für Materialtechnik, TU Clausthal, Clausthal-Zellerfeld, Germany; ³Jülich Centre for Neutron Science (JCNS) at MLZ, Forschungszentrum Jülich GmbH, Garching, Germany; ⁴Laboratory for Neutron Scattering and Imaging, Paul Scherrer Institute, Villigen, Switzerland

Self-diffusion in metastable solids, such as amorphous or nano-crystalline materials, is a fundamental matter transport process which is important for material stability and structure-property relationships. Due to the metastability, the measurement of diffusion processes is made more easily accessible by methods that can detect diffusive motion on a length scale of some nanometers. Neutron reflectometry (NR) is ideally suited to this task. NR experiments were carried out, making it possible to determine self-diffusivities in amorphous silicon (a-Si) for the first time. a-Si is a model system for a covalently bound amorphous semiconductor with technological importance, e.g. in thin film transistors, solar cells and Li-ion batteries. For the experiments, isotopically modulated (^{nat}Si/²⁹Si) amorphous silicon multilayer samples with a total thickness of 300 nm were deposited by ion-beam sputtering. The samples were then measured using NR after various stages of annealing at temperatures between 550 and 700 °C at the θ-2θ-reflectometer MARIA at the MLZ and at the time of flight reflectometer AMOR at PSI, Villigen, Switzerland. NR patterns of this kind of sample yield Bragg peaks due to the different coherent scattering lengths of the two isotopes. The decrease in the peaks with increasing annealing time and temperature due to isotope interdiffusion is then evaluated and used to calculate self-diffusivities. The calculation hinges upon the description of the peak area after a time *t*, *I*(*t*), as

$$I(t) = I(0) \cdot \exp\left(\frac{8\pi^2 n^2 D}{l^2} \cdot t\right), \quad (1.1)$$

where *n* is the order of the evaluated peak, *l* the thickness of a double layer, *D* the diffusivity and *I*(0) the peak area in

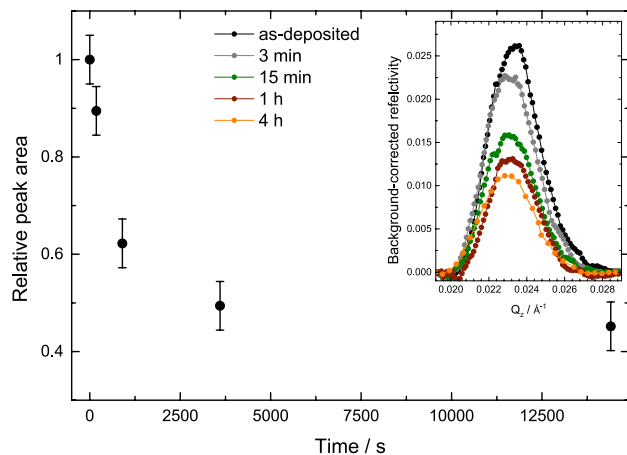


Figure 1: Decrease of the first order Bragg peak of a [²⁹Si_{6nm} | ^{nat}Si_{24nm}]₁₀ multilayer sample after annealing at 650 °C for up to 4 h. The integrated peak area relative to the as deposited sample is plotted versus the annealing time. The background-corrected reflectometry patterns can be seen in the inset.

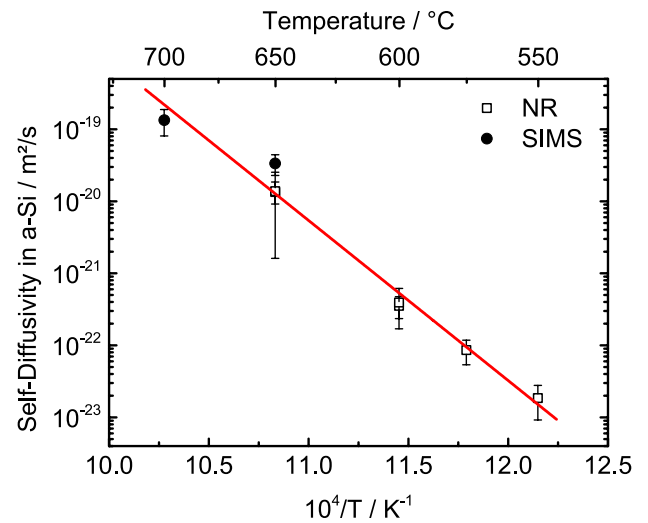


Figure 2: Arrhenius plot of a-Si self-diffusivities versus the inverse temperature. NR data are shown by open squares, the additional SIMS data at high temperatures by black dots. The depicted linear fit gives an activation energy of $E_a = (4.4 \pm 0.3)$ eV and a pre-exponential factor of $D_0 = 1.5 \times 10^4$ m²/s (error: $\log_{10}D_0 = 1.5$).

the as-deposited state. Furthermore, $d = \sqrt{2Dt}$ is the diffusion length. Fig. 1 shows the decrease of the artificial Bragg peak after annealing at 650 °C and the evaluated peak area plotted versus the annealing time. The apparent diffusion lengths in those experiments of 5 nm and above point towards a long range diffusion process that can be well separated from short range structural relaxation processes in the amorphous matrix. By comparing the peak areas after the annealing steps to the as-deposited state, diffusivities are calculated and plotted in an Arrhenius-diagram which is shown in Fig. 2.

Diffusivities range from around 2×10^{-23} m²/s at 550 °C to 1×10^{-20} m²/s at 650 °C and show no time dependence. Additional Secondary Ion Mass Spectrometry measurements at high temperatures confirm the NR results. The diffusivities in Fig. 2 yield an activation energy of self-diffusion of 4.4 eV and a pre-exponential factor of $D_0 = 1.5 \times 10^4$ m²/s. The high activation energy points to a combination of defect formation and migration energies governing the diffusive process. As compared to self-diffusivities in crystalline silicon (c-Si), the diffusivities found in this study surpass those in c-Si by five orders of magnitude at 700 °C. This can be interpreted as the consequence of a high diffusion entropy (high pre-exponential factor). The presence of extended point defects consisting of several atoms has been suggested as a possible explanation for the high diffusion entropy.

F. Strauß et al., Self-Diffusion in Amorphous Silicon, Phys. Rev. Lett. 116, 25901 (2016)

C. Stieghorst^{1,3}, B. Karches³, K. Welter³, H. Gerstenberg², G. Hampel³, P. Krenckel³, P. Kudějová¹, J. Lichtinger¹, C. Plonka³, B. Ponsard⁵, S. Riepe⁴, T. Reich³, Z. Révay¹, J. Schön⁴, N. Wieh³

¹Heinz Maier-Leibnitz Zentrum (MLZ), Technische Universität München, Garching, Germany; ²Forschungs-Neutronenquelle Heinz Maier-Leibnitz (FRM II), Technische Universität München, Garching, Germany; ³Johannes Gutenberg-Universität Mainz, Institut für Kernchemie, Mainz, Germany; ⁴Fraunhofer-Institut für Solare Energiesysteme ISE, Freiburg, Germany; ⁵Belgian Nuclear Research Centre (SCK-CEN), Mol, Belgium

Directional solidification is an important step in the production of solar cells based on multi-crystalline silicon (mc-Si). To lower the cost and energy consumption involved in their manufacture, it is necessary to know the extent and the distribution of the impurities in the raw material, crucibles and silicon blocks (ingots). Dopants control the conductivity of the solar cell, while 3d transition metals act as recombination centers and reduce the cell efficiency. We analyzed all these impurities using neutron activation techniques.

The Fraunhofer Institute for Solar Energy Systems ISE produced the test ingots, which were sampled by sawing and etching (pieces ~1.5g). The irradiations were performed at the FRM II, the BR2 and the TRIGA Mainz. The joint project of the JGU Mainz and the ISE was supported by the DFG (No. HA 5571/4-1, BO 3498/1).

3d transition metals

The 3d metals accumulate in the liquid phase during the crystallization from the bottom to the top of the ingot, depending on an element specific segregation coefficient k . The profile of the element concentration c_s can roughly be described by the Scheil equation $c_s = k \cdot c_0 \cdot (1 - f_s)^{k-1}$, where c_0 is the initial concentration and f_s the already solidified fraction. We analyzed the ingots using neutron activation analysis (INAA) and found a deviating U-shaped distribution along the height of the ingot, caused primarily by diffusion processes from the crucible and coatings as well as back diffusion from the top of the ingot during crystallization and cooling.

Boron analysis

Boron is the dopant which is commonly used for solar cells based on p-doped silicon. Prompt gamma activation analysis (PGAA) is very sensitive in the case of boron. Five different test ingots were analyzed. The results fit very well with expectation, based on the conditions of the crystallization (e.g. see Fig. 1). Additionally, a sensitive method based on neutron-induced charged-particle coincidence measurements (originally developed for Li determination by Lichtinger et al.) was tested for low B concentrations in Si (<10ppb_w). In a 1µm thick sample, which was dissected from a silicon wafer through etching at the ISE, a qualitative B determination was possible.

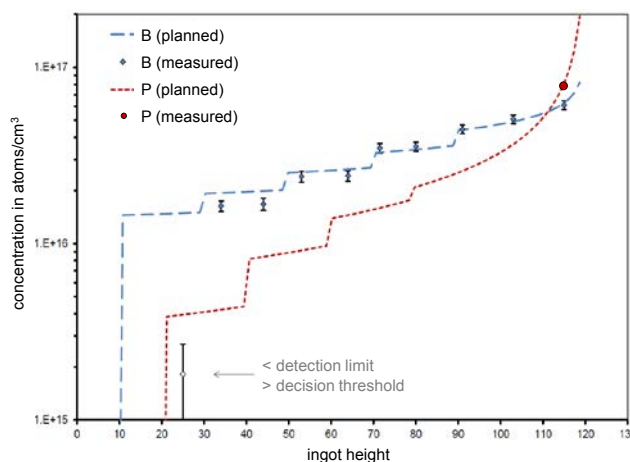


Figure 1: Planned and measured B and P concentrations.

Phosphorus analysis

Phosphorus is the most important dopant in n-type solar cells. The analysis of low P concentrations in silicon is generally challenging, and this is also true for conventional neutron activation techniques. We used the β radiation of P-32 for the analysis. Disturbances of radiation emitted by other activated impurities were suppressed with a β - γ anticoincidence setup - a combination of a plastic scintillator for β detection and a surrounding NaI(Tl) γ -ray detector. Geant4 simulations were performed to correct for the β absorption. The result of an ingot sample is in good agreement with the expected values based on the doping plan at the ISE (Fig. 1), thus confirming the suitability of the proposed method.

A complete panoramic analysis of the dopants and the 3d metal was performed using neutron activation methods, as a better understanding of the behavior of impurities in mc-Si is essential for the development of more cost effective solar cell production. Finally, doping plans of test ingots and simulations performed at the ISE show good agreement with our results.

B. Karches et al., Instrumental determination of phosphorus in silicon for photovoltaics by β spectroscopy: a new approach, J. Radioanal. Nucl. Chem. 311, 541 (2016)

S. Seidlmayer¹, I. Buchberger², M. Reiner³, T. Gigl³, R. Gilles¹, H. A. Gasteiger², C. Hugenschmidt^{1,3}¹Heinz Maier-Leibnitz Zentrum (MLZ), Technische Universität München, Garching, Germany; ²Chair of Technical Electrochemistry, Department of Chemistry and Catalysis Research Center, Technische Universität München, Garching, Germany; ³Physik Department E21, Technische Universität München, Garching, Germany

In lithium ion batteries, the widely used NMC-111 ($\text{Li}_{1-x}\text{Ni}_{1/3}\text{Mn}_{1/3}\text{Co}_{1/3}\text{O}_2$) cathode electrodes suffer a capacity loss during the first charge-discharge cycle. Recovering full lithiation during the cell discharge of the cathode material (e. g. back to $x = 0$) is not possible under normal conditions. This irreversible capacity loss (ICL) typically reaches values up to $x = 0.08$. However, if the underlying reasons for this effect were better understood, it is possible that the total cell capacity or cycling and aging behavior could be improved.

For the first time, we applied defect sensitive positron annihilation spectroscopy (PAS) to charged and discharged NMC-111 electrodes of this type of battery material in order to investigate the structure and evolution of vacancy type defects in the electrodes in correlation with their structural and crystallographic properties. Our results support the idea that the ICL is caused by a kinetic barrier, as we discuss the relation between positron annihilation and electronic structure in terms of structural dynamics during the lithiation process.

Samples of NMC-111 electrodes with decreasing lithium content ($x = 0 - 0.7$) covering the whole range of state of charge were electrochemically prepared in Swagelok T-cells and then dismantled for non-destructive analysis using positron coincidence Doppler broadening spectroscopy (CDBS). Additionally, after the first discharge, various samples were prepared using 12 h voltage hold steps (at 2.0 V/25 °C, at 3.0 V/25 °C, and at 3.0 V/55 °C), following galvanostatic discharge, to examine the evolution of lattice defects and lithium vacancies. The combination of CDBS with X-ray diffraction made it possible to discuss the ICL in the first charge-discharge cycle with respect to possible implications due to vacancy ordering. In particular, CDBS revealed that the highest degree of relithiation was obtained after discharge to 3.0 V at 55 °C.

In our study, a clear correlation between positron annihilation and the degree of delithiation x was found, showing the microscopic behavior of the positrons to predominantly annihilate in lithium vacancies and the sensitivity of the annihilation process on the changing lattice constants. In Fig. 1, the annihilation S parameter is plotted versus delithiation degree x and four different sections are marked. In section (i), at very low x annihilation from competing states such as lithium vacancies or transition metal vacancies becomes relevant and needs to be taken into account in detail in future studies by employing *ab initio* modelling of the electronic structure. Using a combination of CDBS, XRD, and electrochemistry, we also revealed that kinetic effects cause

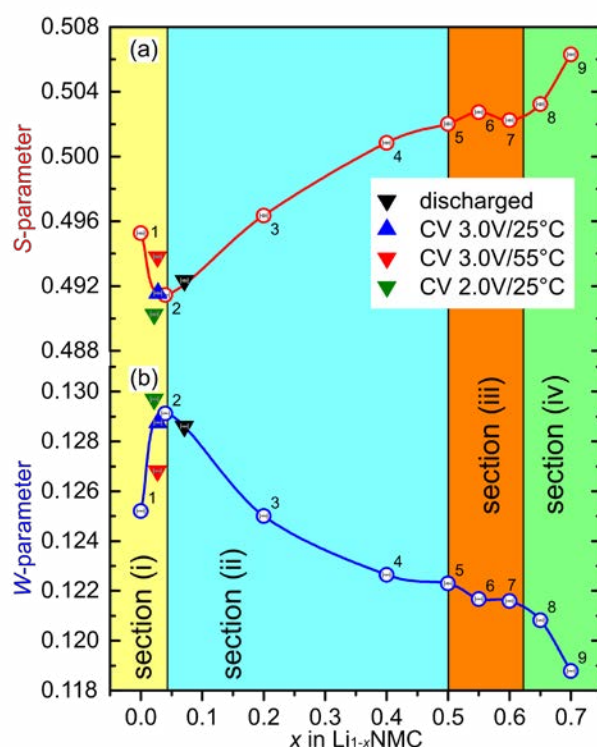


Figure 1: Doppler broadening line-shape (S) and wing (W) parameters measured on NMC-111 electrode samples in dependence of removed lithium amount x . Solid lines are guides for the eyes only. Instrumental error of the CDBS-parameters is shown as tiny circles, and the standard deviation in x as a small bar inside the data symbols. The experimental error in S and W is <0.001 and therefore not visible in the figure. Samples are numerated according to reference. Sections (i) – (iv) are marked in color.

the first cycle capacity loss of the cathode material due to the dependence of vacancy evolution on temperature rather than on the discharge voltage (see reference for further details, also sections (ii) and (iii)). In section (iv) at high delithiation ($x > 0.5$), changes in the electronic structure affect both the S -parameter measured by PAS and, simultaneously, the lattice parameter changes in the XRD show a strong deviation from linearity. It is envisaged that, in the future, this study will be extended by complementary positron annihilation lifetime spectroscopy (PALS) to differentiate between various types of vacancies.

S. Seidlmayer et al, First-cycle defect evolution of $\text{Li}_{1-x}\text{Ni}_{1/3}\text{Mn}_{1/3}\text{Co}_{1/3}\text{O}_2$ lithium ion battery electrodes investigated by positron annihilation spectroscopy, J. Power Sources 336, 224 (2016)

S. Zimnik, C. Piochacz, S. Vohburger, C. Hugenschmidt

Heinz Maier-Leibnitz Zentrum (MLZ) and Physik Department, Technische Universität München, Garching, Germany

The investigation of the elemental composition of surfaces is of great importance for the understanding of various surface-related processes such as catalysis, phase transitions or surface segregation. Functional materials and surfaces based on Pd are employed for e.g. heterogeneous catalysis or hydrogen purification. For industrial applications, several factors, such as the chemical composition of the Pd surface, which significantly influences its catalytic effectiveness, and the mechanical stability e.g. of thin membranes, which is affected by foreign atoms or segregation processes, play an important role.

Nowadays, the design of catalysts is focused on reducing cost and increasing efficiency, leading to more complex combinations of different catalytically active materials. To give an example, it was recently shown that the efficiency of direct-ethanol fuel cells can be increased by using a catalyst with a Ni/Pd bilayer structure instead of a pure Pd surface. To achieve long-term stability of the functional surfaces of such compound systems, the surface mechanisms leading to a degradation of the catalytic activity need to be understood.

In our study, we focused on the Pd surface covered with a varying amount of Ni in order to investigate the time-dependent evolution of the chemical composition of the Ni/Pd surface. In order to characterize the behavior of very low Ni coverages, i.e. nominal thickness below one monolayer (ML) of Ni on a Pd surface, or even to observe surface segregation, a method of highest surface sensitivity is required.

We experimentally demonstrated the outstanding surface sensitivity of Positron-annihilation induced Auger Electron Spectroscopy (PAES) by comparing the results with those of conventional AES induced by electrons and X-rays. In particular, time-dependent PAES was performed on a 0.5 ML Ni cover layer on Pd and compared with conventional X-ray induced Photoelectron Spectroscopy (XPS) in order to observe changes in the elemental composition of the surface. The PAES results appear to show a migration of Ni atoms into the Pd substrate, whereas the Ni signal shows a decrease of 12 % within 13 h with respect to the initial value (see Fig. 1).

Influences on the detected amount of Ni and Pd due to possible surface contamination with molecules of the residual gas were analyzed by a complementary time-dependent XPS analysis on pure Ni and Pd accompanying the PAES study. Consequently, it was concluded that the PAES data show a superposition of carbon contamination and structural changes at the surface of Ni/Pd.

Financial support by the German Federal Ministry of Education and Research within the project no BMBF-05K13WO1 is gratefully acknowledged.

S. Zimnik et al., Time-dependent investigation of sub-monolayers of Ni on Pd using Positron-annihilation induced Auger Electron Spectroscopy and XPS, Surf. Sci. 643, 178 (2016)

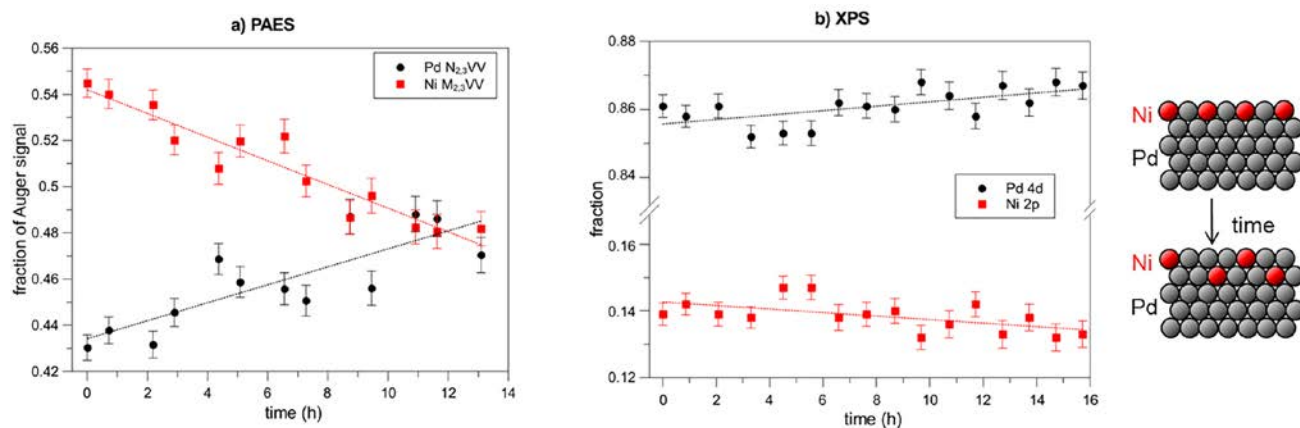


Figure 1: Comparison of the time-dependent fraction of Ni and Pd in (a) PAES and (b) XPS on 0.5ML Ni on Pd. Both methods show the same trend, but the higher surface sensitivity of PAES leads to a more significant result, indicating the migration of Pd atoms to the sub-surface as sketched in the illustration.

F. Ziegler¹, H. Gibhardt¹, O. Sobolev¹, M. M. Murshed², T. M. Gesing², G. Eckold¹

¹Institute of Physical Chemistry, Georg-August-Universität Göttingen, Göttingen, Germany; ²Solid State Chemical Crystallography, Institute of Inorganic Chemistry and Crystallography and MAPEX Center for Materials and Processes, University of Bremen, Bremen, Germany

Mullite-type $\text{Bi}_2\text{Mn}_4\text{O}_{10}$ has attracted scientific attention in recent years due to its multiferroic nature below $T_N = 40$ K. Most investigations so far have focused on the magnetic and electric behavior, while the mechanical properties have been somewhat neglected. However, the origin of multiferroicity in $\text{Bi}_2\text{Mn}_4\text{O}_{10}$ has still not been definitively established, but elastic interactions and local distortions seem to play an important role. For a better understanding of multiferroic coupling, we therefore determined the full set of nine elastic constants using inelastic neutron scattering.

All experiments were performed on a single crystal at the thermal three-axes spectrometer PUMA@FRM II under ambient conditions. Taking into careful consideration the resolution of the instrument, we measured the dispersion curves of selected acoustic phonons close to the Γ point, which makes it possible to calculate the corresponding sound velocities. These are a function of a certain combination of elastic constants dependent on the wave propagation direction. For example, it is possible to obtain six constants alone from phonons which propagate along the principal axes of the crystal, as shown in Fig. 1. The remaining three constants can be derived from the propagation directions $(\xi, \xi, 0)$, $(\xi, 0, \xi)$ and $(0, \xi, \xi)$.

Having determined the nine elastic constants, it is possible to calculate the sound velocity of all three acoustic phonons for any propagation direction (see Fig. 2). Here, a clear mechanical anisotropy can be observed. All phonons which involve a displacement of atoms along the **a**-direction propagate with lower velocity. This indicates that the material is considerably harder in the **b**- and **c**-directions than along the **a**-axis, which is a direct result of the coordination geometry of the metal ions. Furthermore, this is also the direction of the spin orientation in the multiferroic phase. We therefore plan temperature-dependent measurements at low temperatures for the future to further investigate the connection between multiferroic coupling and mechanical behavior.

F. Ziegler et al., Mechanical properties of multiferroic $\text{Bi}_2\text{Mn}_4\text{O}_{10}$: Full set of elastic constants determined by inelastic neutron scattering; Phys. Status Solidi B 253, 976 (2016)

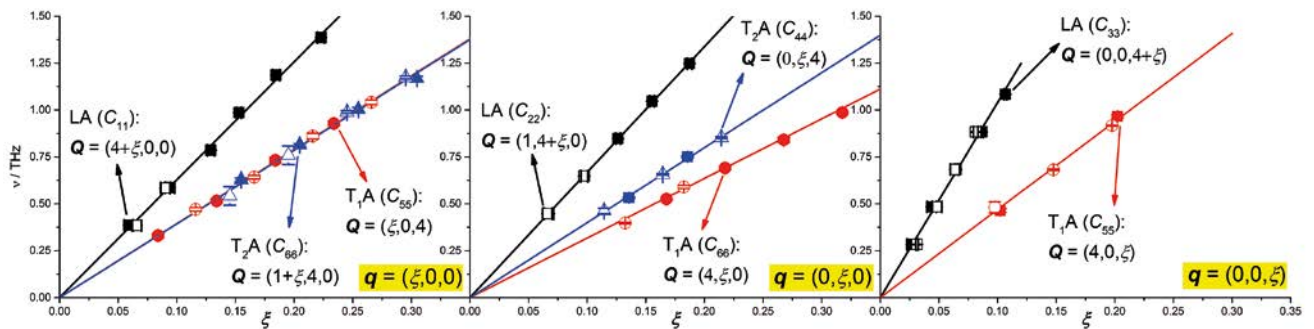


Figure 1: Dispersion curves for all measured acoustic phonons propagating along the principal directions as indicated by the propagation vector \mathbf{q} . The sound velocity of each longitudinal (LA) and transverse phonon (TA) corresponds to one elastic constant (C_i) in this setup. \mathbf{Q} denotes the scattering vector of the respective phonon.

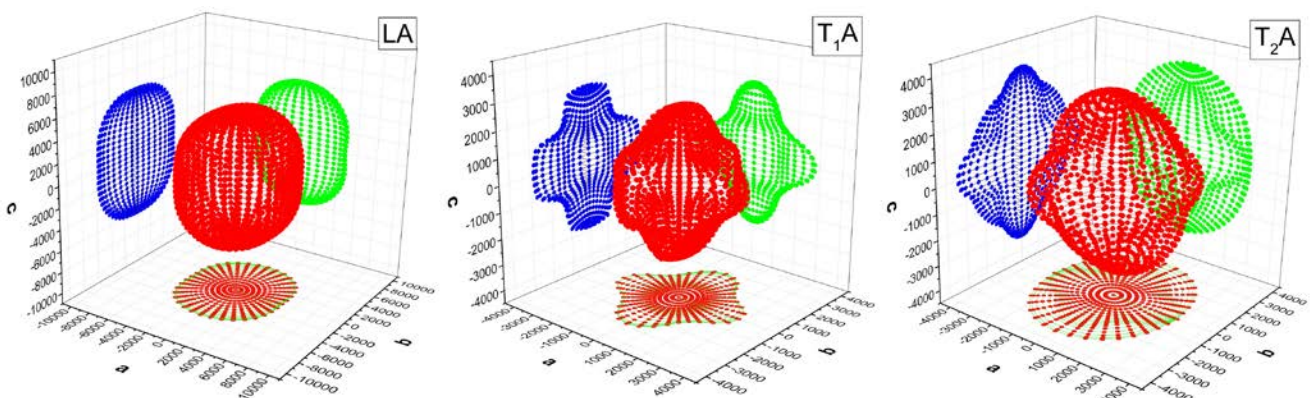


Figure 2: Calculated sound velocities (in m s^{-1}) of the longitudinal (LA) and transverse phonons (TA) for arbitrary propagation directions.

C. Stock¹, Y. Su², S.-W. Cheong³

¹Institute for Condensed Matter and Complex Systems, University of Edinburgh, Edinburgh, UK; ²Jülich Centre for Neutron Science (JCNS) at MLZ, Forschungszentrum Jülich GmbH, Garching, Germany; ³Department of Physics & Astronomy, Rutgers Center for Emergent Materials, Rutgers University, Piscataway, USA

Materials that display localized behavior have been studied extensively in the search for new properties, including localized electronic and electromagnetic states. In the context of magnetism, single molecular magnets have been investigated owing to their ability to tune quantum properties, as well as possible device applications, and the mesoscopic magnetic structures that have been created to confine magnetic excitations. While localization in many of these systems is introduced through breaking up regular structures, the spatial localization of energy has been known to exist in periodic structures that also contain strong nonlinear interactions.

In this work, we demonstrate the presence of localized antiphase boundaries in the classical magnet CaFe_2O_4 using the DNS polarized diffractometer. CaFe_2O_4 is unusual

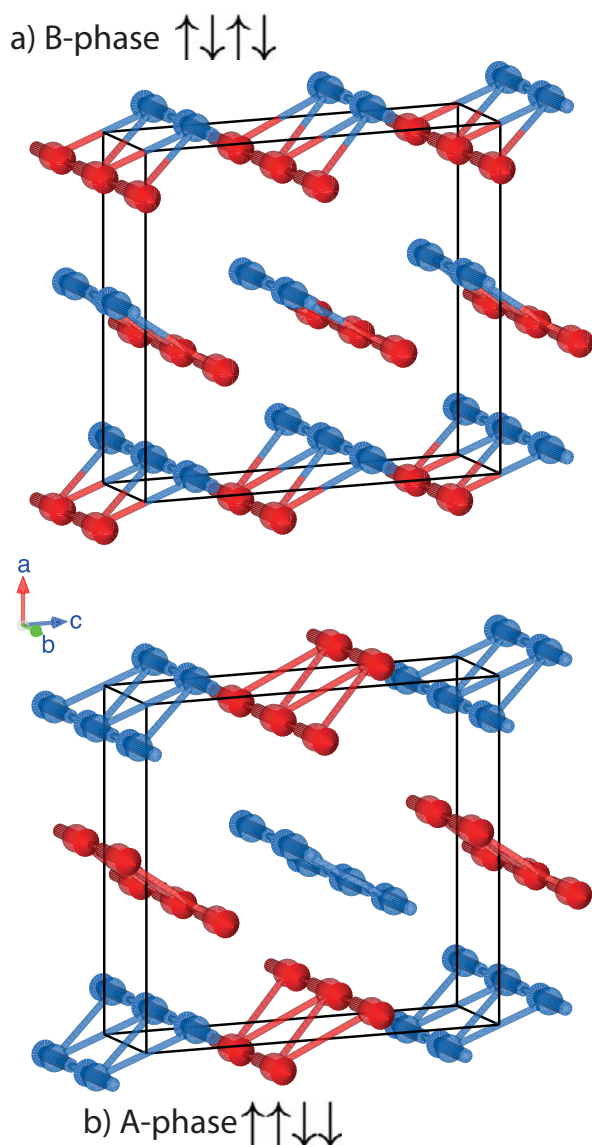


Figure 1: The two magnetic structures of CaFe_2O_4 solved through neutron powder diffraction and polarized neutrons on DNS.

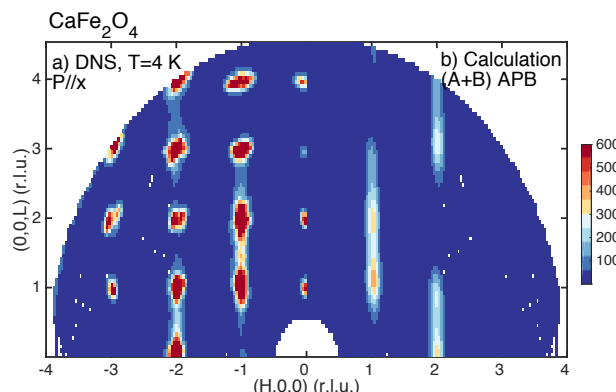


Figure 2: The measured (a) and calculated (b) diffuse scattering patterns measured on DNS. The calculation is based on antiphase boundaries along the c axis.

in that it displays two magnetic transitions with magnetic structures differing by c-axis stacking of antiferromagnetic stripes (Fig. 1). At high temperatures of 200 K, the B phase is present, being replaced by the A phase at lower temperatures. The two phases can be thought of as differing by an antiphase boundary along the c-axis resulting from an exchange coupling which is on the verge of being either anti or ferromagnetic. Given the presence of a large anisotropy gap in the excitations, the magnetic moments in both phases are constrained to be aligned along the b axis of an orthorhombic cell. Work on DNS has shown that the transition from B phase to A phase ordering is incomplete, as evidenced by a significant amount of diffuse scattering.

The results are summarized in Fig. 1 (a) which plots the magnetic scattering probed through aligning the incident beam neutron polarization parallel to the momentum transfer. Fig. 1 (b) illustrates a calculation considering only antiphase boundaries along the c axis with resolution limited peaks in the a and b directions. Further polarization analysis, based on the xyz setup on DNS, revealed that the moment orientation of the diffuse scattering is uniaxial, with the moments being aligned along the b-axis. These boundaries are dynamic with relaxational timescales, studied with spin-echo, of the order of GHz. Further work on this compound has revealed that these antiphase boundaries are confining, resulting in a discrete series of countable excitations. CaFe_2O_4 therefore represents a unique case of confinement in a classical magnet where nonlinear terms are introduced from a large anisotropy.

C. Stock et al., *Solitary Magnons in the S=5/2 Antiferromagnet CaFe_2O_4* , *Phys. Rev. Lett.* **117**, 017201 (2016)

Q. Wang¹, J. T. Park², Y. Feng¹, Y. Shen¹, Y. Hao¹, B. Pan¹, J. W. Lynn³, A. Ivanov⁴, S. Chi⁵, M. Matsuda⁵, H. Cao⁵, R. J. Birgeneau^{6,7}, D. V. Efremov⁸, J. Zhao^{1,9}

¹State Key Laboratory of Surface Physics and Department of Physics, Fudan University, Shanghai, China; ²Heinz Maier-Leibnitz Zentrum (MLZ), Technische Universität München, Garching, Germany; ³Center for Neutron Research, National Institute of Standards and Technology (NIST), Gaithersburg, Maryland, USA; ⁴Institut Laue-Langevin, Grenoble, France; ⁵Quantum Condensed Matter Division, Oak Ridge National Laboratory, Oak Ridge, USA; ⁶Department of Physics, University of California, Berkeley, USA; ⁷Department of Materials Science and Engineering, University of California, Berkeley, USA; ⁸IFW Dresden, Dresden, Germany; ⁹Collaborative Innovation Center of Advanced Microstructures, Fudan University, Shanghai, China

In iron based superconductors, weak coupling theories suggest that superconductivity is mediated by spin fluctuations due to a sign reversal between the superconducting order parameters on different parts of the Fermi surfaces. In this scenario, a sharp resonant mode is expected to emerge below 2Δ in the spin excitation spectrum below T_c (2Δ is the superconducting gap). On the other hand, it has been pointed out that, in the case of the sign preserved order parameter, there is a redistribution of the magnetic spectral weight below T_c , which leads to a broad peak above 2Δ . Therefore, the observation of the peak either below or above 2Δ allows the relative sign of the order parameter to be identified.

We performed inelastic neutron scattering experiments on PUMA at the MLZ to explore the effect of isovalent S doping on the spin dynamics and its relationship with superconductivity in $K_xFe_{2-y}(Se_{1-z}S_z)_2$. Fig. 1 shows the Q-scans for $K_xFe_{2-y}(Se_{1-z}S_z)_2$ of four S concentrations ($z = 0, 0.25, 0.4, 0.5$; $T_c = 31.2, 32.0, 28.4, 25.4$ K). In all the samples measured, the momentum-space structure of the magnetic excitations barely changes.

Fig. 2 (a-d) show the evolution of the resonant mode as a function of S concentration. A sharp spin resonant mode is observed in the spectra of the undoped sample in the superconducting state (Fig. 2a). To our surprise, in the $z = 0.4$ sample, an additional shoulder emerges above 2Δ in the spectra (Fig. 2b). With increasing S concentration to $z = 0.5$, the resonant mode is completely replaced by a broad hump structure above 2Δ (Fig. 2c), suggesting that the superconducting order parameter no longer has a sign reversal at this doping level. The detailed temperature dependence of the resonant mode and the hump above 2Δ confirm that the redistribution of the spectra is intimately associated with superconductivity (Fig. 2(d-g)).

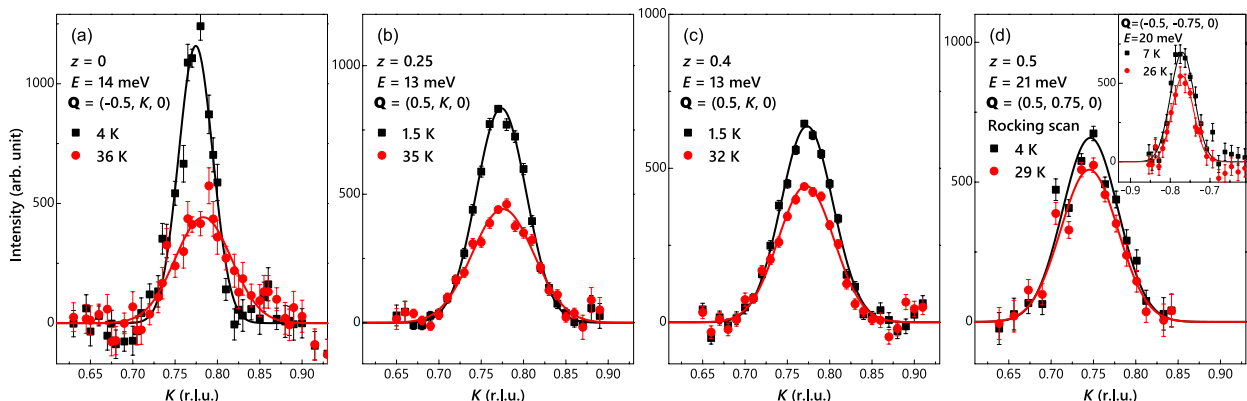


Figure 1: (a)-(d) Constant energy scans in the superconducting and the normal state for the $z = 0, 0.25, 0.4,$ and 0.5 samples, respectively.

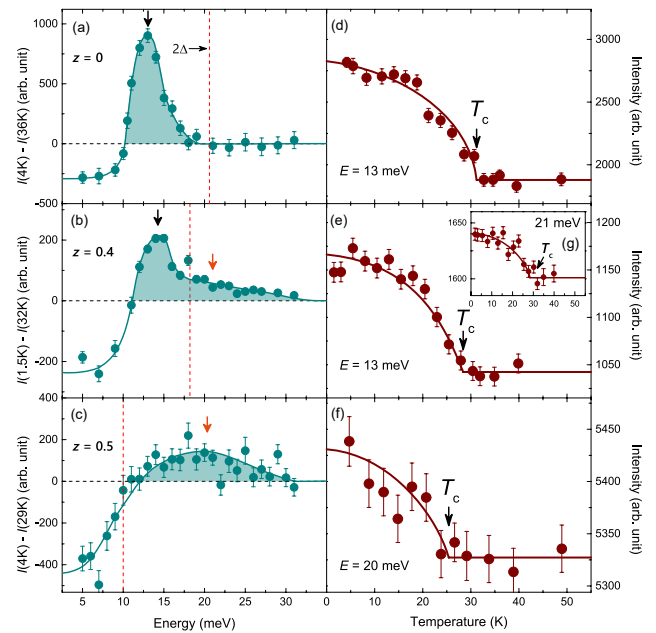


Figure 2: (a)-(d) Energy dependence of the intensity difference between the superconducting and the normal state in the vicinity of $Q = (0.5, 0.75, 0)$ in $K_xFe_{2-y}(Se_{1-z}S_z)_2$ ($z = 0, 0.4, 0.5$). (d)-(g) Temperature dependence of the spin excitations.

Our results suggest that multiple pairing channels are required in order to describe superconductivity in this system. It is possible that $K_xFe_{2-y}(Se_{1-z}S_z)_2$ is close to an intermediate pairing state.

Q. Wang et al., *Transition from Sign-Reversed to Sign-Preserved Cooper-Pairing Symmetry in Sulfur-Doped Iron Selenide Superconductors*, *Phys. Rev. Lett.* **116**, 197004 (2016)

The term ‘nematic’ is conventionally used to describe a state in liquid crystals where the rod-like molecules tend to align themselves in the same direction, but in disordered positions. This nematic state breaks the rotational symmetry of the liquid, but preserves the translational symmetry which is usually broken in crystals. Thus, it can be viewed as an intermediate state between liquid and crystal. Similarly, correlated electrons can also form such a ‘nematic’ state, but this time, rather than breaking the symmetry of the free space, the rotational symmetry of the host crystal is spontaneously broken. Although electrons have no structure, they can behave in different ways in two equivalent directions in lattice perspective, such as showing unequal mobility in two orthogonal directions, as observed in iron-based superconductors.

The origin of nematic order remains one of the major questions in iron-based superconductors. In theories based on spin nematicity, the spins begin to fluctuate in different dynamic correlations along two orthogonal nearest neighbor directions with one direction more antiparallel correlated than the other, before they are condensed into a collinear AFM state. As a result, the spin-spin correlations show anisotropy between $(\pi, 0)$ and $(0, \pi)$. Although the intensity anisotropy of the low-energy spin excitations and the enhancement of the correlation length at $(\pi, 0)$ below T_s are observed in experiments, the decrease of the correlation length at $(0, \pi)$ had never been measured. Using inelastic neutron scattering, we carried out such a measurement in detwinned $\text{BaFe}_{1.935}\text{Ni}_{0.065}\text{As}_2$ at PUMA triple-axis spectrometer and obtained good results consistent with the spin nematic theory.

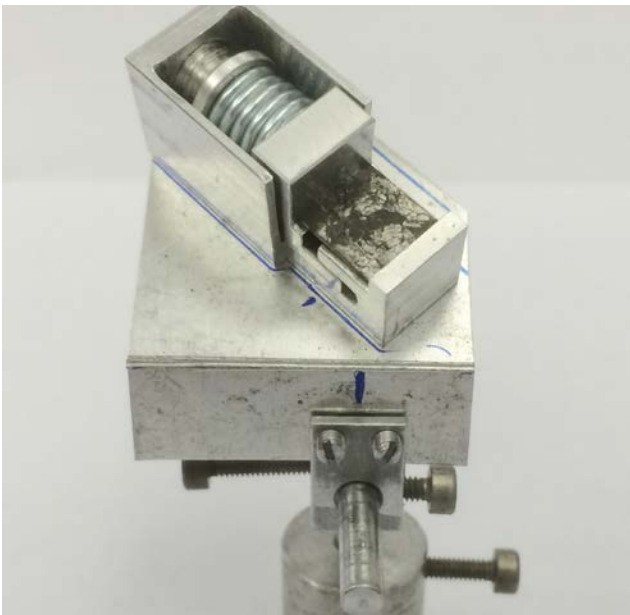


Figure 1: The sample set-up shows the square sample under uniaxial stress applied through the action of a spring.

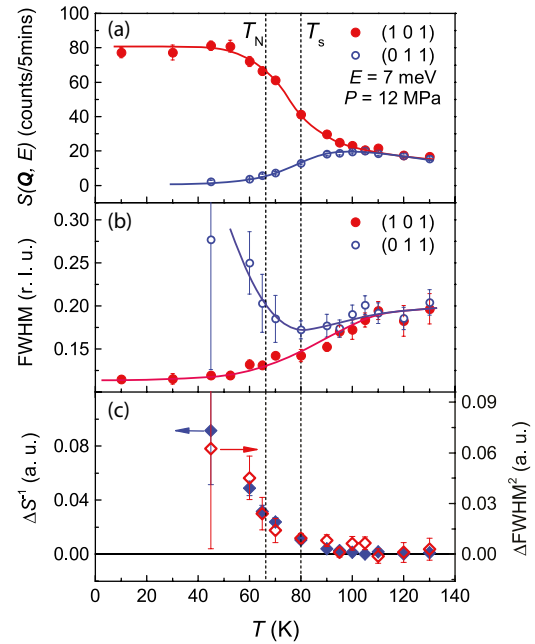


Figure 2: Temperature dependence of (a) $S(Q, E)$ and (b) FWHM at $(1\ 0\ 1)$ and $(0\ 1\ 1)$ at 7 meV and 12 MPa. (c) Temperature dependence of ΔS^{-1} (blue solid diamonds) and ΔFWHM^2 (red open diamonds) as defined in the main text. The solid lines are a guide for the eye. The error bars are given by the Gaussian fits.

Since the twinning effect naturally mixes the information of $(\pi, 0)$ and $(0, \pi)$, the sample needs to be detwinned. Usually, a uniaxial stress is applied to detwin the sample, Fig. 1 shows our device used to apply uniaxial stress. Fig. 2 summarises our results on the temperature dependence of the low energy spin-spin correlations in $\text{BaFe}_{1.935}\text{Ni}_{0.065}\text{As}_2$. The difference between $(\pi, 0)$ and $(0, \pi)$ both in the intensity and the correlation length starts well above T_s , possibly due to the stabilization of nematic spin fluctuations by the uniaxial pressure due to spin-lattice coupling. The spin-spin correlation at $(0, \pi)$ starts to decrease just below T_s suggesting, that the nematic order transition seems still well defined at T_s even under large uniaxial pressure. We also plot the temperature dependence of $\Delta S(Q, E)^{-1}$ and ΔFWHM^2 in Fig. 2(c), where $\Delta S(Q, E)^{-1} = S(Q, E)^{-1}_{(011)} - S(Q, E)^{-1}_{(101)}$ and $\Delta \text{FWHM}^2 = \text{FWHM}^2_{(011)} - \text{FWHM}^2_{(101)}$. The two quantities are well scaled, which accords with the spin nematic theory. Our results provide a good description of the effect of nematic order on the low-energy spin fluctuations in iron based superconductor $\text{BaFe}_{1.935}\text{Ni}_{0.065}\text{As}_2$ and are well consistent with the spin nematic theory.

W. Zhang et al., Effect of Nematic Order on the Low-Energy Spin Fluctuations in Detwinned $\text{BaFe}_{1.935}\text{Ni}_{0.065}\text{As}_2$; *Phys. Rev. Lett.* 117, 227003 (2016)

S. Demirdiř¹, C. J. van der Beek², S. Mühlbauer³, Y. Su¹, T. Wolf⁴

¹Jülich Center for Neutron Science (JCNS) at MLZ, Forschungszentrum Jülich GmbH, Garching, Germany; ²Laboratoire des Solides Irradiés, CNRS UMR 7642 & CEA-DSM-IRAMIS, Ecole Polytechnique, Palaiseau cedex, France; ³Heinz Maier-Leibnitz Zentrum (MLZ), Technische Universität München, Garching, Germany; ⁴Institut für Festkörperphysik, Karlsruher Institut für Technologie, Karlsruhe, Germany

Vortex lattice (VL) studies performed so far on Fe-based superconductors have revealed strong pinning properties and the associated highly disordered vortex ensembles, the only exception being the work on the single crystalline KFe_2As_2 . Our recent results, obtained using the SANS-1 instrument at the MLZ on a high quality $\text{Ba}_{0.64}\text{K}_{0.36}\text{Fe}_2\text{As}_2$ single crystal, show that vortex lattice disorder can be sufficiently weak in this system to permit the observation of well-defined Bragg peaks corresponding to a long-range orientationally ordered triangular lattice.

Fig. 1(a) - (d) show clear diffraction peaks observed up to $B_a = 0.75$ T. Above this field, the diffraction spots start to broaden, and their intensity diminishes. A near-circular (polycrystalline) diffraction pattern is observed at $B_a = 1$ T, whence the scattered intensity has vanished for $B_a = 2$ T. The radial scans of the scattered intensity presented in Fig. 1(e) quantify this decrease. Furthermore, the rocking curves in Fig.1(f) confirm the decrease as well as a broadening of the FWHM with increasing B_a . The average vortex lattice structure factor S and the form factor $F^2(q, T)$ presented in Fig. 2 show the maximum measured intensity value at low fields, which drops abruptly above 0.5 T, an indication for a structural disordering transition of the VL.

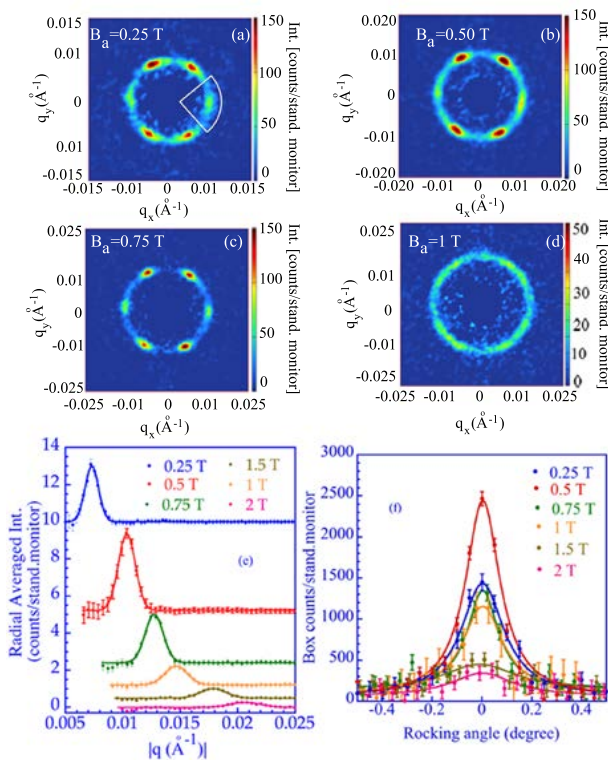


Figure 1: (a)–(d) Small-angle neutron scattering pattern of the vortex solid in $\text{Ba}_{0.64}\text{K}_{0.36}\text{Fe}_2\text{As}_2$, for magnetic fields ranging from 0.25 T to 1 T. (e) Radial intensity distribution versus $|q|$, for different applied magnetic fields. (f) Angular dependence of the diffracted intensity (rocking curves) at different applied magnetic fields. The solid lines are fits to the data with a Lorentzian function.

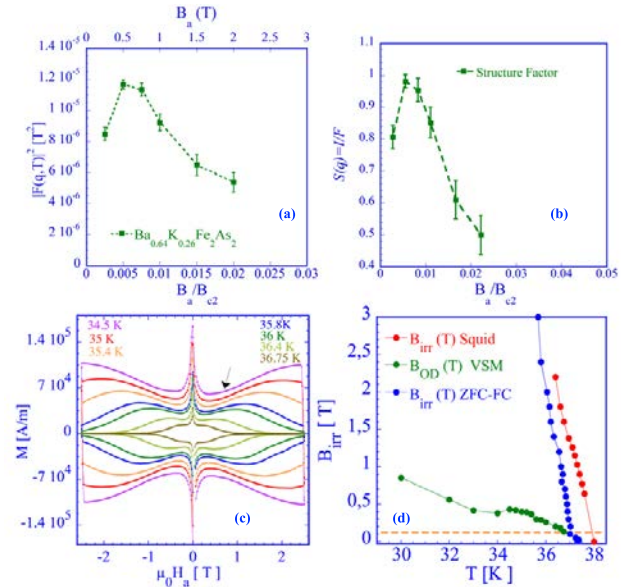


Figure 2: (a) Field dependence of $|F(q, T)|^2$ extracted from the integrated intensity obtained by integration over an arc of 60° spanning the vortex Bragg peak as indicated in Fig. 1(a). (b) Field dependence of the vortex structure factor, extracted from the data. (c) Loops of the hysteric magnetization $M(B_a)$ for selected different temperatures. (d) Magnetic phase diagram of the vortex ensemble. The vertical orange line corresponds to the boundary between the irreversibility line $B_{irr}(T)$ and the order-disorder line $B_{OD}(T)$.

In order to correlate the transition with the VL phase diagram, we resort to the magnetization measurements. The magnetic hysteresis loops in Fig. 2(c) show, at larger fields, an increase in the magnetization (second peak) at the onset of the so-called order- disorder field B_{OD} . At the same time, the VL phase diagram reveals a boundary between the irreversibility line $B_{irr}(T)$ and the order-disorder line $B_{OD}(T)$ (Fig. 2(d)).

To interpret the SANS data, we recall that it is obtained under field-cooling protocol and, therefore, reflects the VL as quenched at $T_f(B)$, which plays the role of a “freezing temperature” T_f . Thus, in all experiments performed at fields below the boundary, the VL is frozen in the ordered state and gives a clear diffraction pattern with $S = 1$, while above the boundary line the strong pinning starts to affect the VL, and results in a progressive disordering, and a decrease in S . Finally, for larger fields the VL is quenched as a disordered polycrystal since the applied field exceeds $B_{OD}(T)$ for all T. Thus, the VL in the $\text{Ba}_{0.64}\text{K}_{0.36}\text{Fe}_2\text{As}_2$ single crystal undergoes a transition from a long-range orientationally ordered VL to a disordered vortex solid.

S. Demirdiř et al., SANS study of vortex lattice structural transition in optimally doped $(\text{Ba}_{1-x}\text{K}_x)\text{Fe}_2\text{As}_2$; *J. Phys.-Condens. Mat.* 28, 425701 (2016)

E. S. Klyushina^{1,2}, A. C. Tiegel³, B. Fauseweh⁴, A. T. M. N. Islam¹, J. T. Park⁵, B. Klemke¹, A. Honecker⁶, G. S. Uhrig⁴, S. R. Manmana³, B. Lake^{1,2}

¹Helmholtz-Zentrum Berlin für Materialien und Energie, Berlin, Germany; ²Institut für Festkörperphysik, Technische Universität Berlin, Berlin, Germany; ³Institut für Theoretische Physik, Georg-August-Universität Göttingen, Göttingen, Germany; ⁴Lehrstuhl für Theoretische Physik I, Technische Universität Dortmund, Dortmund, Germany; ⁵Heinz Maier-Leibnitz Zentrum (MLZ), Technische Universität München, Garching, Germany; ⁶Laboratoire de Physique Théorique et Modélisation, Université de Cergy-Pontoise, Cergy-Pontoise, France

Strongly correlated phenomena (SCP) in quantum magnets have potential applications in devices based on quantum coherence. Since realistic devices must be able to operate *at room temperature*, it is important to identify and quantitatively describe systems which retain coherence at finite temperatures (FT). Here, we report on the investigation of the magnetic properties of the strongly dimerized quantum magnet $\text{BaCu}_2\text{V}_2\text{O}_8$ from base temperature (BT) to moderately high temperatures by performing inelastic neutron scattering (INS) measurements at PUMA. The INS data were analyzed and compared successfully with numerical and analytical calculations. The results (see reference) reveal that $\text{BaCu}_2\text{V}_2\text{O}_8$ remains coherent up to finite temperatures.

Hamiltonian of $\text{BaCu}_2\text{V}_2\text{O}_8$

$\text{BaCu}_2\text{V}_2\text{O}_8$ has a tetragonal crystal structure consisting of double copper-oxygen plaquettes which form screw chains of spin-1/2 Cu^{2+} ions along the c-axis. Single crystal INS measurements at BT revealed that the magnetic excitation spectrum of $\text{BaCu}_2\text{V}_2\text{O}_8$ is gapped and disperses along the c-axis, but is completely dispersionless within the tetragonal plane. This implies that $\text{BaCu}_2\text{V}_2\text{O}_8$ is a highly dimerized system where the dimers (i.e. pairs of spins coupled by a strong antiferromagnetic (AFM) interaction) are coupled into chains along the c-axis. To solve the Hamiltonian, the magnetic excitation spectrum was analyzed using the one-magnon dispersion relation proposed for the dimerized chain. The extracted solutions were used for numerical computations based on the density-matrix renormalization group (DMRG) approach. A comparison of the computed and the experimentally observed excitation spectra reveals that the AFM dimers are coupled into chains by a weak ferromagnetic (FM) interaction. Thus, $\text{BaCu}_2\text{V}_2\text{O}_8$ is a rare example of a highly dimerized AFM–FM chain, providing a unique opportunity to explore SCP at FT in this new class of systems.

SCP at FT in $\text{BaCu}_2\text{V}_2\text{O}_8$

Conventionally, magnetic excitations lose their coherence as temperature increases, resulting in a symmetric Lorentzian energy broadening of their lineshapes. However, in strongly dimerized magnetic systems, where the available phase space is restricted and the magnons interact via the hard-core constraint, the lineshapes were found to broaden asymmetrically as temperature increases. This was attributed to SCP at FT, although a quantitative description has not yet been achieved.

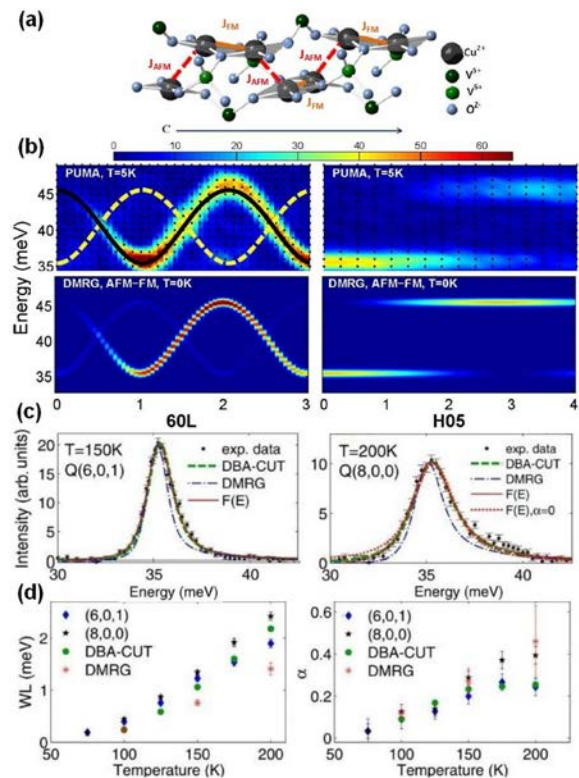


Figure 1: (a) Crystal structure of $\text{BaCu}_2\text{V}_2\text{O}_8$ (the Ba^{2+} are omitted). (b) Magnetic excitation spectra of $\text{BaCu}_2\text{V}_2\text{O}_8$ at BT measured on PUMA, FRMII and computed using the DMRG approach. (c) Lineshapes at FT simulated using DMRG and DBA-CUT approaches plotted over the INS data which are analyzed by a fitting function. (d) Temperature dependence of the asymmetry parameters and Lorentzian width extracted by fitting the experimental and computed lineshapes.

To explore SCP at FT in $\text{BaCu}_2\text{V}_2\text{O}_8$, high resolution constant wave-vector scans were performed for several temperatures up to 200 K. For comparison, the lineshapes of $\text{BaCu}_2\text{V}_2\text{O}_8$ were simulated at the same temperatures using analytical and numerical approaches based on the diagrammatic Brückner approach combined with continuous unitary transformations (DBA-CUT) and the DMRG technique, respectively. The experimental and computed data were then analyzed using a customized fitting function, so that the asymmetry parameter (α) and Lorentzian width (WL) were extracted and plotted as a function of temperature. A comparison of the α and WL extracted from the experimental data at FT with both theoretical approaches reveals an accurate quantitative agreement, confirming the presence of SCP at FT in $\text{BaCu}_2\text{V}_2\text{O}_8$, and shows that coherent behaviour can now be accurately predicted for a given Hamiltonian.

E. S. Klyushina et al., Magnetic excitations in the $S = 1/2$ antiferromagnetic-ferromagnetic chain compound $\text{BaCu}_2\text{V}_2\text{O}_8$ at zero and finite temperature, Phys. Rev. B 93, 241109(R) (2016)

S. V. Grigoriev^{1,2}, A. S. Sukhanov^{1,2}, E. V. Altyntbaev^{1,2}, S.-A. Siegfried³, A. Heinemann³, P. Kizhe^{1,4}, S. V. Maleyev¹
¹Condensed Matter Department, Petersburg Nuclear Physics Institute, NRC "Kurchatov Institute", Gatchina, St. Petersburg, Russia; ²Faculty of Physics, St. Petersburg State University, St. Petersburg, Russia; ³German Engineering Materials Science Centre (GEMS) at MLZ, Helmholtz-Zentrum Geesthacht GmbH, Garching, Germany; ⁴Faculty of Physics, Grad-Kitezh University, Grad-Kitezh, Russia

The competition between the ferromagnetic exchange interaction and the antisymmetric Dzyaloshinskii-Moriya (DM) interaction leads to the appearance of the helical magnetic structure in cubic B20-type compounds. The external magnetic field H_{C2} is necessary to transform the helix with wave vector $|\mathbf{k}_s| = D/J$ into the ferromagnetic collinear full-polarized (FP) state. Despite parallel ordering of the spins in the FP state, the presence of the DM interaction leads to the chirality of the dispersion relation of the spin waves. The dispersion relation in this case has been given by Kataoka as the following: $\varepsilon_q = A(\mathbf{q} - \mathbf{k}_s)^2 + H - H_{C2}$ (1), where A is the spin-wave stiffness. The dispersion curve resembles the ferromagnetic one, but displays three important features: First, the only minimum in the curve is shifted from the position $q = 0$. Second, the sign of the DM constant determines the preferred direction of the propagation of the spin waves. Third, the spin-wave gap related to the magnetic field is shifted by the value $g\mu_B H_{C2}$. The FP state of the DM helimagnets is predicted to be the only known system exhibiting the excitations described by the asymmetrical dispersion relation. To verify the main features of the dispersion relation Eq. (1), one can extend the neutron scattering method that was used to measure the spin-wave stiffness in ferromagnets. The small-angle scattering is limited within the cut-off angle $\theta_c^2(H) = \theta_0^2 - \theta_0/E_i \cdot H + \theta_B^2$ (2). Due to the anisotropy of the dispersion relation, the magnetic field must be set perpendicular to the incident beam to extract the maximal scattering contribution. In this work, we have studied the spin wave dynamic in MnSi by way of an example. The small-an-

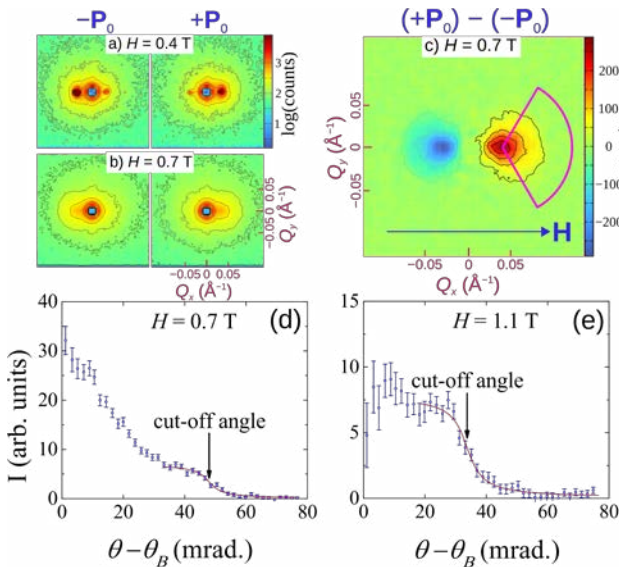


Figure 1: Maps of the SANS intensities for the chiral single crystal MnSi at $T = 15$ K at the field below H_{C2} (0.4 T) (a) and above H_{C2} (0.7 T) (b) for the polarization P_0 opposite the guide field (left) and along it (right). (c) The result of the subtraction of the left and right SANS patterns at $H = 0.7$ T. The averaged scattering intensity I vs scattered angle $\theta - \theta_B$ at $H = 0.7$ T (d), $H = 1.1$ T (e).

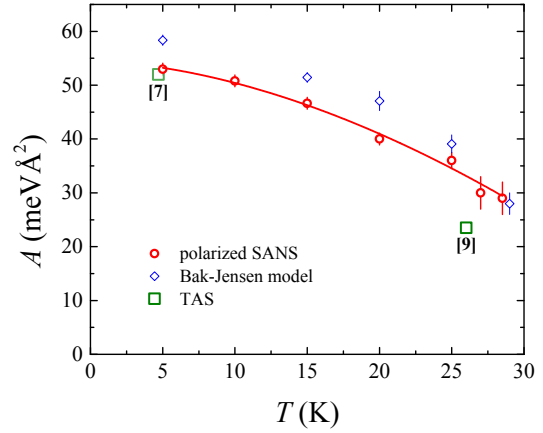


Figure 2: Temperature dependence of the spin-wave stiffness $A(T)$: circles—polarized SANS; squares—TAS [7,9], diamonds estimation from the Bak-Jensen model [3,4]. The solid line is the fit by the power law (see text).

gle neutron scattering makes it possible to, firstly, detect the position of the elastic peak at $\mathbf{Q} = \mathbf{k}_s$ [Fig. 1(a)]. When the magnetic field exceeds the value of H_{C2} , the elastic peak vanishes and we detect a circle of neutron scattering within the centre at $\mathbf{Q} = \mathbf{k}_s$ and a radius equal to θ_c [Fig. 1(b)], which depends only on the spin wave stiffness. To extract the polarization-dependent scattering, the patterns with the polarizations along and opposite to the magnetic field were subtracted one from another [Fig. 1(c)]. The intensity is plotted as a function of the angle $\theta - \theta_B$ in Fig. 1 (d–e) at different values of the field and $T = 15$ K. The cut-off angle $\theta_c(H)$ can easily be obtained from the analysis of the I versus $\theta - \theta_B$ plot. Using Eq. (2), one can determine the value of the parameter θ_0 (and the spin-wave stiffness) with high accuracy. The spin-wave stiffness, obtained from the detection of the cut-off angles at different temperatures, is presented together with the calculated values from the Bak-Jensen model in Fig. 2. The measured temperature dependence was fitted by the power law as follows: $A(T) = A_0[1 - c(T/T_C)^z]$, where z is equal to 1.8 ± 0.3 with $A_0 = 0.054$ meV \AA^2 and $c = 0.47$. The temperature dependence of the stiffness calculated in this model is shown in Fig. 2. Both the magnitudes of the stiffness and a tendency for a small decrease with temperature are the same for the calculated and measured values.

In conclusion, we have experimentally proven: (i) the validity of the spin-wave dispersion relation for helimagnets with the DM interaction in the full-polarized state [Eq. (1)] and (ii) the ability to study the sw dynamics of helimagnets with DM interaction using polarized SANS.

S. V. Grigoriev et al., Spin waves in full-polarized state of Dzyaloshinskii-Moriya helimagnets: Small-angle neutron scattering study; Phys. Rev. B 92, 220415(R) (2015)

C. H. Lee¹, K. Kihou¹, J. T. Park², K. Horigane³, K. Fujita³, F. Waßer⁴, N. Qureshi⁴, Y. Sidis⁵, J. Akimitsu³, M. Braden⁴

¹National Institute of Advanced Industrial Science and Technology (AIST), Tsukuba, Ibaraki, Japan; ²Heinz Maier-Leibnitz Zentrum (MLZ), Technische Universität München, Garching, Germany; ³Aoyama Gakuin University, Sagami-hara, Japan; ⁴Il. Physikalisches Institut, Universität zu Köln, Cologne, Germany; ⁵Laboratoire Léon Brillouin (LLB), C.E.A./C.N.R.S., Gif-sur-Yvette, France

The mechanism of Cooper pair formation in iron-based superconductors remains a controversial topic. The resonance mode is interpreted as a bound spin-exciton state (particle-hole excitation) in the spin fluctuation model, where the energy (E_{res}) must remain below $2\Delta_s$. In contrast, there is an enhancement of magnetic scattering at energies exceeding $2\Delta_s$ in the orbital fluctuation model. Therefore, we have studied the spin fluctuation of hole doped $\text{Ba}_{1-x}\text{K}_x\text{Fe}_2\text{As}_2$ using the triple-axis spectrometer PUMA.

Incommensurate peaks

Low-energy spin fluctuations in $\text{Ba}_{1-x}\text{K}_x\text{Fe}_2\text{As}_2$ vary from commensurate to incommensurate peaks located at $Q = (0.5 \pm \delta, 0.5 \pm \delta, L)$ for $x > 0.5$ (Fig. 1). The incommensurability δ increases with increasing doping level associated with the suppression of T_c , forming a parabolic relationship up to $x = 0.66$. This indicates that the periodicity of the spin fluctuations has a considerable impact on superconductivity and that a commensurate structure is advantageous for achieving high T_c . The parabolic correlation, however, ends near $x = 0.66$, where T_c drops dramatically. This suggests that the interplay between magnetism and superconductivity changes around $x = 0.66$.

Spin resonance peaks

A well-defined spin resonance peak is observed at $E_{\text{res}} = 5$ meV for $x = 0.5$ (Fig. 2). The resonance intensity decreases drastically with hole doping, while E_{res} remains almost constant. The dramatic suppression of the resonance intensities can itself be explained by the spin exciton model,

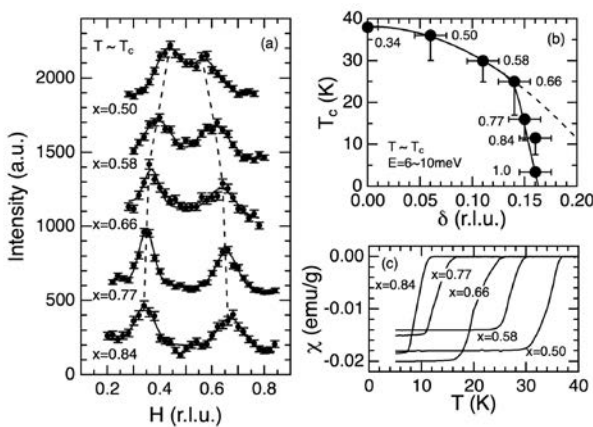


Figure 1: (a) Q-spectra of $\text{Ba}_{1-x}\text{K}_x\text{Fe}_2\text{As}_2$ along $(H, H, 1)$ in the normal state. Energies and temperatures are $E = 8$ meV, $T = 42$ K for $x = 0.50$; $E = 8$ meV, $T = 36$ K for $x = 0.58$; $E = 8$ meV, $T = 36$ K for $x = 0.66$; $E = 8$ meV, $T = 22$ K for $x = 0.77$ and $E = 6$ meV, $T = 15$ K for $x = 0.84$. (b) T_c vs. incommensurability δ in the normal state close to T_c . Vertical error bars depict a superconducting transition width. Data for $x = 0.34$ and 1.0 are extracted from [Sci. Rep. 1, 115 (2011)] and [Phys. Rev. Lett. 106, 067003 (2011)], respectively. (c) Shielding signals measured under a magnetic field of $H = 10$ Oe.

where the resonance intensity is proportional to $2\Delta_s - E_{\text{res}}$, given the restriction that E_{res} be smaller than $2\Delta_s$. In fact, E_{res} is smaller than $2\Delta_s = 7.5k_B T_c$ and approaches $2\Delta_s$ with increasing doping, keeping $E_{\text{res}}/k_B T_c$ at an almost constant value of 5 below $x = 0.66$. On the other hand, $E_{\text{res}}/k_B T_c$ increases drastically above $x = 0.66$ and reaches values of 10.5 at $x = .84$. Such a high value can no longer be explained by the spin exciton model, which cannot yield a resonance feature above $2\Delta_s$ within the continuum of particle-hole excitations. It seems that the effect of magnetism on superconductivity is reduced and other mechanisms, such as the orbital fluctuation model, arise in the overdoped region.

C. H. Lee et al., *Suppression of spin-exciton state in hole overdoped iron-based superconductors*, *Sci. Rep. 6, 23424 (2016)*

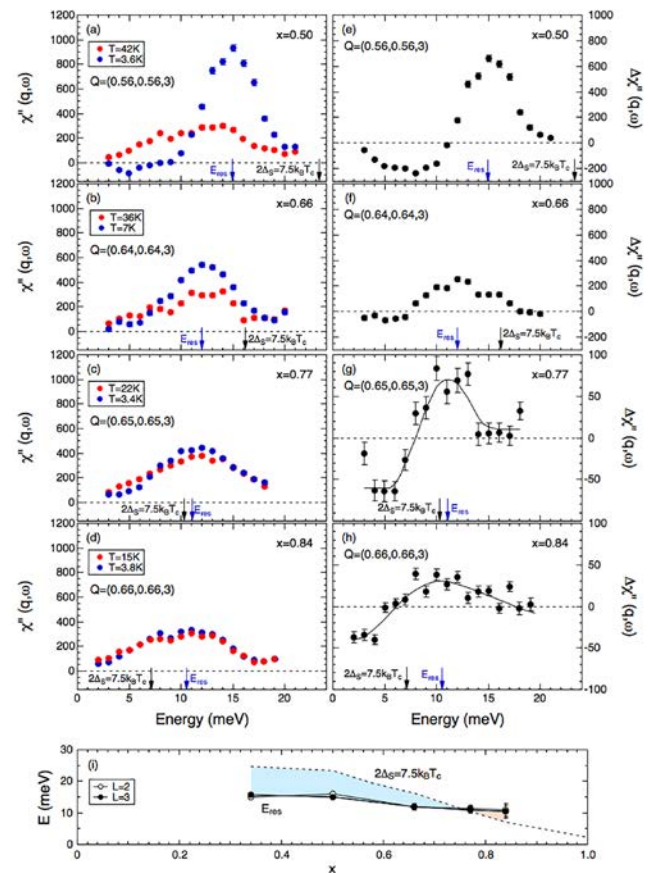


Figure 2: (a-d) Energy dependences of $\chi''(q, \omega)$ at peak positions in Q-scans at $T \sim T_c$ and $T < T_c$ for (a) $x = 0.50$, (b) $x = 0.66$, (c) $x = 0.77$ and (d) $x = 0.84$. Amplitudes were normalized by phonon scattering intensities. (e-h) Difference of $\chi''(q, \omega)$ between $T \sim T_c$ and $T < T_c$. (i) Doping dependences of E_{res} at $L = 2$ and 3 with data of $x = 0.34$ extracted from [Sci. Rep. 1, 115 (2011)]. E_{res} is almost independent of L . The dashed line depicts the superconducting gap value of $2\Delta_s = 7.5k_B T_c$.

X. Lu¹, K.-F. Tseng^{2,3}, J. T. Park³, T. Keller^{2,3}, P. Dai¹

¹Department of Physics and Astronomy & Rice Center for Quantum Materials, Rice University, Houston, Texas, USA; ²Max-Planck-Institute for Solid State Research, Stuttgart, Germany; ³Heinz Maier-Leibnitz Zentrum (MLZ), Technische Universität München, Garching, Germany

The newly discovered electronic nematic in iron-pnictide high- T_c superconductors has attracted much attention due to its significance in revealing the driving force of the structural and antiferromagnetic transitions. The origin of the nematicity is believed to be crucial for an understanding of the microscopic mechanism of the high- T_c superconductivity in iron pnictides.

In electron doped $\text{BaFe}_{2-x}\text{T}_x\text{As}_2$ ($T = \text{Co, Ni}$), resistivity measurements in detwinned samples revealed an in-plane electronic anisotropy emerging from a temperature (T^*) well above the tetragonal-to-orthorhombic structural transition temperature (T_s). It has been suggested that the surprising electronic nematicity in the tetragonal state $T^* > T_s$ arises from the fluctuations associated with the structural transitions. However, since most experiments to investigate the electronic nematicity were performed on uniaxial-strained samples, it is possible that the uniaxial stress breaks the C_4 rotational symmetry and induces the nematicity above T_s .

To understand the microscopic origin of the electronic anisotropy in the paramagnetic state, it is important to establish the effect of a uniaxial pressure on the structural transitions of iron pnictides.

The spectrometer TRISP at the MLZ is an ideal choice to settle this issue. Its Larmor diffraction mode is capable of measuring lattice distortions and thermal expansions of single crystals with $\Delta d/d \sim 10^{-6}$, which is better than high resolution x-ray diffraction and can probe the whole sample.

Combining TRISP with our detwinning device, we have unambiguously determined the effect of uniaxial stress on the structural transitions and lattice distortions in electron-doped iron pnictides $\text{BaFe}_{2-x}\text{Ni}_x\text{As}_2$ with $x = 0, 0.03, 0.12$ and $\text{SrFe}_{1.97}\text{Ni}_{0.03}\text{As}_2$. We find the pressure-induced lattice distortions for $T > T_s$ to be comparable for all the materials and show a strong coupling between the uniaxial pressure induced lattice distortion and the electronic nematic. However, we have to be cautious in directly relating resistivity anisotropy to the nematic order parameter in the iron pnictides. Details of the experimental setup and results can be found in the reference.

X. Lu et al., Impact of uniaxial pressure on structural and magnetic phase transitions in electron-doped iron pnictides; Phys. Rev. B 93, 134519 (2016)

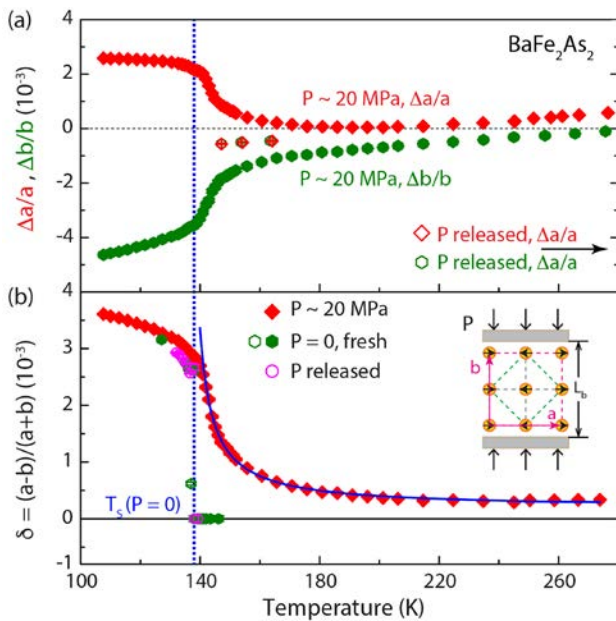


Figure 1: Temperature dependence of the a and b lattice parameters and orthorhombicity δ under different uniaxial pressure conditions for BaFe_2As_2 . The data were measured by Larmor diffraction on TRISP. The pressure is applied along the orthorhombic b axis [inset of Fig. 1(b)].

M. Katava¹, M. Maccarini², G. Villain¹, A. Paciaroni³, M. Sztucki⁴, O. Ivanova⁵, D. Madern⁶, F. Sterpone¹

¹Laboratoire de Biochimie Théorique, IBPC, CNRS UPR9080, Univ. Paris Diderot, Sorbonne Paris, France; ²Univ. Grenoble Alpes - Laboratoire TIMC/IMAG UMR CNRS 5525, La Tronche, France; ³Dipartimento di Fisica e Geologia, Università di Perugia, Perugia, Italy; ⁴European Synchrotron Radiation Facility, Grenoble, France; ⁵Jülich Centre for Neutron Science (JCNS) at MLZ, Forschungszentrum Jülich GmbH, Garching, Germany; ⁶Institut de Biologie Structurale (IBS), Univ. Grenoble Alpes, CEA, CNRS, Grenoble, France.

Conformational changes that occur during enzymatic turnover are essential for the regulation of protein functionality. Establishing the protein regions involved in these changes and the dynamical processes associated with the protein functions are still demanding tasks, both theoretically and experimentally.

We performed a combined Neutron Spin Echo (NSE) spectroscopy and Molecular Dynamic (MD) simulations study to uncover the characteristic length- and time-scales associated with the thermal activation of the functional modes and conformational changes in a eukaryotic Lactate Dehydrogenase (LDH) enzyme.

We observed that the modes involving the catalytic loop and the mobile region around the binding site become activated at room temperature. These modes match the allosteric reorganisation of bacterial LDHs. Our study shows that, in a temperature window of about 15 degrees, these modes make the protein sufficiently flexible and capable of reorganising the active site toward a functional configuration. By raising the temperature further, an excess of thermal excitation leads to the distortion of the protein matrix with a possible anti-catalytic effect.

The NSE experiments were performed on a LDH protein dispersed in a buffer solution at 90 mg/ml at the J-NSE in-

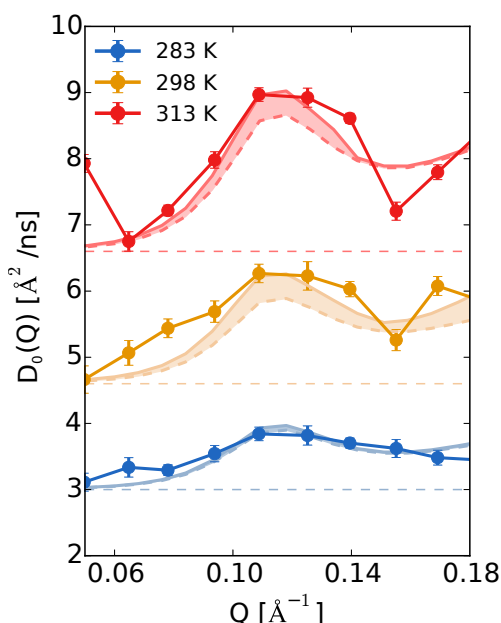


Figure 1: Experimental diffusion spectra at different temperatures compared to the theoretically reconstructed spectrum (solid curve) obtained by adding the rigid-body contribution (dashed curve) to the internal-dynamics contribution derived from long MD simulations (shown in the shaded area).

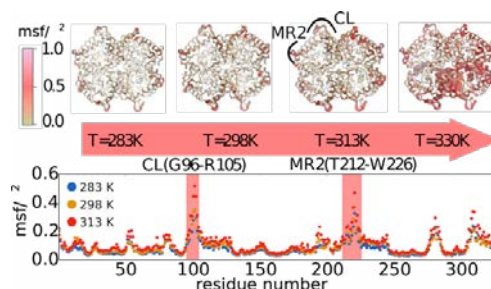


Figure 2: The flexible regions of the protein individuated by the local atomistic fluctuations are highlighted in the protein structure and along the subunit sequence. We have specifically indicated the loop of the catalytic site (CL) and the adjacent helical region (MR2).

strument and probed dynamical modes in a length-scale between 170 and 30 Å, and at the nanosecond timescale. At these characteristic length and time-scales, the signal comes from the correlated motion of separated atoms (coherent contribution) belonging to different protein domains. The dynamical processes expressed in terms of diffusion, D_0 , as a function of temperature are shown in Fig. 1. The D_0 includes the rigid-body translational and rotational contribution plus the contribution due to the internal protein dynamics. NSE cannot distinguish between these three components, and MD simulations were used to separate the internal dynamics (shadowed contribution in Fig. 1) from the rigid-body contribution.

The thermally activated motions that make the greatest contribution to the NSE spectra involve the long-range displacement of the four domains forming the protein, and span the characteristic lengths 40-70 Å. In particular, the most flexible regions are localized around the binding site and control its structural reorganization (Fig. 2). These regions had already been found to be those most affected in the allosteric activation of the homolog bacterial LDH. Hence, for our non-allosteric protein too, the catalytic site samples active configurations at the working temperature that are either inaccessible at lower temperature, or corrupted by extreme excitation at higher temperatures.

In conclusion, our study has shown that temperature regulates the functionality of the rabbit LDH as does the allosteric mechanism for the homologues bacterial variants of the protein, and long-range inter-domain motions are key factors for this regulation.

M. Katava et al., Thermal activation of 'allosteric-like' large-scale motions in a eukaryotic Lactate Dehydrogenase; Sci. Rep. 7, 41092 (2017)

F. Foglia^{1,9}, R. Hazael¹, G. G. Simeoni², M.-S. Appavou³, M. Moulin⁴, M. Haertlein⁴, V. T. Forsyth^{4,5}, T. Seydel⁶, I. Daniel⁷, F. Meersman^{1,8}, P. F. McMillan¹

¹Chemistry Department, Christopher Ingold Laboratories, University College London, London, UK; ²Heinz Maier-Leibnitz Zentrum (MLZ), Technische Universität München, Garching, Germany; ³Jülich Centre for Neutron Science (JCNS) at MLZ, Forschungszentrum Jülich GmbH, Garching, Germany; ⁴Life Science Group, Institut Laue-Langevin, Grenoble, France; ⁵Faculty of Natural Sciences/ISTM, Keele University, Staffordshire, UK; ⁶Science Division, Institut Laue-Langevin, Grenoble, France; ⁷Laboratoire de Géologie de Lyon, Université Lyon, Villeurbanne, France; ⁸Biomolecular & Analytical Mass Spectrometry, Department of Chemistry, University of Antwerp, Antwerp, Belgium; ⁹Department of Chemical Engineering, Imperial College London, London, UK

Understanding the functioning of extremophile bacteria under high pressure conditions is essential when seeking to answer critical questions concerning Earth's deep biosphere. It is also necessary to optimize food preservation via "Pascalization" processes, as well as by applying emerging biotechnology. A core mechanism of cellular activity involves both the mobility of water inside the cell and its transport across the cell envelope. Quasi-elastic neutron scattering (QENS) is a powerful technique for studying correlated proton dynamics and relaxation processes over a wide range of momentum and energy transfers at timescales relevant to cellular biology. Due to the large differences in H/D neutron incoherent cross sections, isotopic contrast experiments can be designed to focus on dynamics that occur within specific regions of the cell. Specifically, we have investigated water dynamics in live *Shewanella oneidensis* bacteria at ambient pressure and 2 kbar. Deuterated bacteria were produced using the Deuteration Laboratory of the Life Sciences Group at the Institut Laue-Langevin. Scattering experiments were carried out at the instrument TOFTOF using an AI-body cell with an internal gauge to continuously monitor the pressure. Our pioneering experiments indicate that, although the intracellular mobility is indistinguishable from bulk dy-

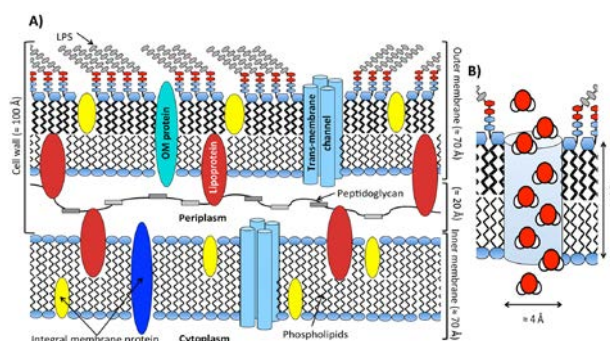


Figure 2: Sketch of the cell membrane and trans-membrane diffusion pathways for Gram negative bacteria. (A) schematic drawing showing the inner and outer membrane as well as periplasmic space. (B) Cartoon drawing depicting H₂O transport through an Aquaporin channel such as AqZ in *E. coli* or *Shewanella*.

namics at ambient pressure, a clear slowdown is observed as the pressure is increased to 2 kbar, which is substantially (-25 %) greater than that observed for the surrounding aqueous medium (-18 %). This is undoubtedly related to the effects on water diffusion of interactions with macromolecules within the nanoconfined cellular environment. The analysis of our contrast measurements for the transport across the cell wall showed an unexpected narrowing of the QENS line shapes for $Q = 0.7\text{--}1.1 \text{ \AA}^{-1}$ which corresponds to an enhanced relaxation time for correlated water dynamics over a real space distance of about 6-9 Å (see Fig. 1). This length scale corresponds to that for H₂O molecules passing through the "neck" region of Aquaporin channels embedded within the membrane structures (see Fig. 2), providing the first direct observation of this process *in vivo*. Our experiments demonstrate that high pressure QENS can be applied to the study of live biological systems, including the use of isotopic contrast protocols to spatially highlight different relaxation regimes of biochemical action, while leading to new insights into the nature and relaxation dynamics of water both inside the cell and across the cell membrane, under ambient and extreme high pressure conditions.

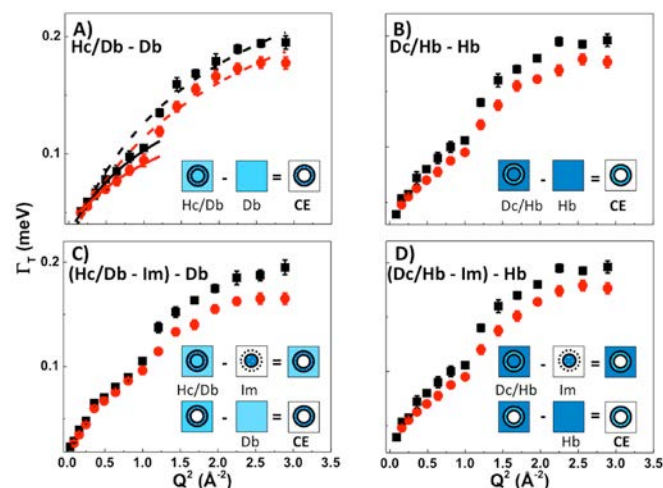


Figure 1: Water dynamics across the cell envelope (CE) at ambient pressure (black) and 2 kbar (red), visualised using different isotopic contrast subtractions. (A): Hc/Db - Db: (hydrogenated cells/in deuterated buffer) - deuterated buffer, with Singwi-Sjölander jump model fits to the overall cell envelope (0.2-1.8 Å⁻¹) shown as dashed lines and restricted to the 0.2-1.0 Å⁻¹ range (solid lines). (B): Data points for the corresponding isotopic contrast Dc/Hb - Hb: (deuterated cells/in hydrogenated buffer) - hydrogenated buffer. Panels (C) and (D): Data taking into account differential effects of pressure on intracellular medium (Im) compared with the bulk media (Hb, Db): (Hc/Db - Im) - Db and (Dc/Hb - Im) - Hb.

F. Foglia et al., Water Dynamics in Shewanella oneidensis at Ambient and High Pressure using Quasi-Elastic Neutron Scattering; Sci. Rep. 6, 18862 (2016)

D. Schwahn¹, V. Pipich²

¹Heinz Maier-Leibnitz Zentrum (MLZ), Technische Universität München, Garching, Germany; ²Jülich Centre for Neutron Science (JCNS) at MLZ, Forschungszentrum Jülich GmbH, Garching, Germany

It is stated in the literature that “the behavior of poly (ethylene oxide) (PEO) in aqueous environment is the key to its importance in biomedical and biotechnical applications”. A relevant example is the role PEO plays in protecting against organic fouling in membrane-based wastewater treatment technologies. PEO has been successfully incorporated into the design of water treatment membranes, thanks to graft polymerization. It was found that the chemical nature of PEO resists the non-specific binding of proteins. Our research in this area allows us to explore the properties of aqueous PEO in more detail, using the technique of small-angle neutron scattering (SANS).

PEO in water represents a so-called associating aqueous solution, as hydrogen bonding between PEO and water plays an essential role, determining the solubility at ambient temperature. Phase separation is observed above 90 °C. We studied the PEO of molar mass between 0.45 and 280 kDa close to its critical concentration in a temperature interval between 11.8 and 95.7 °C. We measured the thermal fluctuations of the PEO concentration determined by the susceptibility $S(Q=0)$ (i.e. scattering function at scattering vector $Q=0$), as depicted in Fig. 1. The inverse susceptibility versus inverse temperature ($1/T$) follows a scaling law

according to $S^{-1}(0) = (1/C_+) \tau^\gamma$ with respect to the reduced temperature $\tau = [1/T - 1/T_C]/(1/T_C)$, the critical exponent γ , and the critical temperature T_C . In the case of 3D-Ising critical behavior and mean field approximation lead one to expect numerical values of $\gamma = 1.239 \pm 0.003$ and $\gamma = 1$, respectively. The 0.5 kDa PEO shows mean field behavior as the critical point is far from the accessible temperatures. The next two PEO solutions of 5 and 10 kDa exhibit the expected 3D-Ising behavior, whereas the three largest PEOs of 70, 90, and 280 kDa show near mean field exponents. This change in γ indicates a transition to tricritical point behavior which belongs to the universality class of $d = 3$ and $n = 0$ dimensions of space and order parameter, respectively, which is different from the 3D-Ising case showing $n = 1$ as suggested by deGennes in the late 1970s. Another scaling behavior is shown in Fig. 2 for the amplitudes of susceptibility (C_+) and correlation length (ξ_0), confirming the proposed critical exponents for semi-dilute polymer solutions shown to be valid for an associating polymer solution following critical 3D-Ising and tricritical Θ -point behavior.

D. Schwahn and V. Pipich, Crossover from ordinary critical to tricritical behavior in the poly(ethylene glycol) aqueous solution, Macromolecules 49, 8228 (2016)

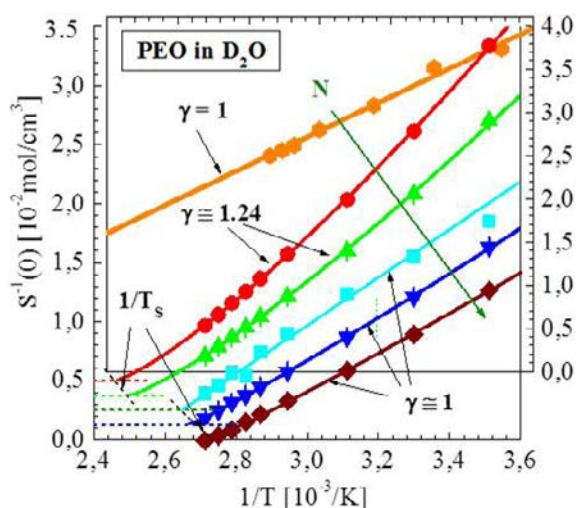


Figure 1: Inverse susceptibility of PEO in D₂O of near critical composition. For better transparency the 0.5k-90 k data were shifted to larger $S^{-1}(0)$ (dashed line indicates zero $S^{-1}(0)$). Meaning of symbols: ● (PEO-0.5k); ● (PEO-5k); ▲ (PEO-10k); ■ (PEO-70k); ▼ (PEO-90k); ◆ (PEO-280k).

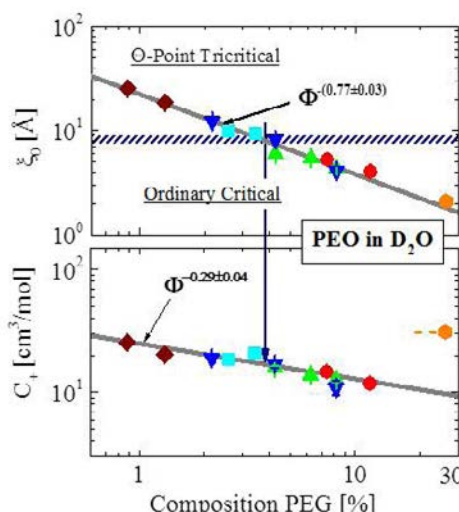


Figure 2: Amplitudes of correlation length and susceptibility of thermal fluctuations versus PEO composition. Colored symbols used as in Figure 1.

H. Frielinghaus¹, J. Viell², N. K. Szekely¹

¹Jülich Centre for Neutron Science at MLZ, Forschungszentrum Jülich GmbH, Garching, Germany; ²Aachener Verfahrenstechnik-Process Systems Engineering, RWTH Aachen University, Aachen, Germany

Wood, and biomass in general, provide valuable resources for chemicals and/or fuels. The valorization of wood, however, requires efficient pretreatment that prepares the cellulose for enzymatic saccharification. Mild conditions at high selectivity are preferable for high yields. Ionic liquids, which are still rather expensive, have been identified as suitable for such pretreatment. However, water contamination appears naturally and reduces the efficiency of this poorly understood process.

The pretreatment of beech wood in 1-ethyl-3-methylimidazolium acetate (EMIMAc) and small amounts of water was studied using spectroscopy, x-ray and neutron scattering. The wood was treated at 115 °C for 1.5 h, and then analyzed further. At lower water content ($\leq 8.6\%$), the processed wood is a rather fluffy material (Fig. 1), while at higher water content the morphology resembles the original wood, and only the color becomes considerably darker. Using x-ray diffraction, the crystallinity of the cellulose was observed: At lower water content ($\leq 8.6\%$), the cellulose turned quite amorphous, while at higher water content the crystallinity even increased slightly. At lower water content, the enzymatic digestion is quite complete. Interestingly, even higher water content ($\geq 10.7\%$) allowed for enhanced digestion by the enzymes. This accessibility of the enzymes to the cellulose is a key parameter in pretreatment and needs to be understood microscopically.

In the small angle neutron scattering experiment, the wood samples were swelled in heavy water to achieve enhanced contrast. The natural wood displayed two distinct correlation peaks (at $Q \approx 1.6 \text{ nm}^{-1}$) in the meridional plane, which accounts for the packing distance of 3.9 nm of cellulose microfibrils within the fibres. The anisotropy is maintained, but less pronounced, for higher water content (12.6 and 8.6 %), while at lower water content the scattering was isotropic.

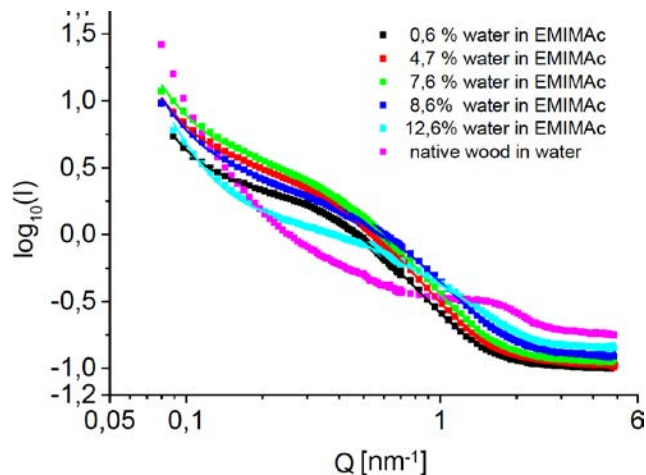


Figure 2: Radially averaged SANS profiles of native and pretreated wood samples swelled in D_2O .

The radially averaged scattering (Fig. 2) displays a shoulder at $Q \approx 0.6 \text{ nm}^{-1}$ that is connected to the fibril diameter (7.6 to 9.0 nm for water content below 8.6 %, and 5.6 nm for 12.6 %). The larger diameters coincide with the amorphous state of the cellulose after concentrated EMIMAc pretreatment that enhances the accessibility for the enzymes, while dilute EMIMAc pretreatment only leads to the coalescence of microfibrils. This coalescence obviously increases the enzymatic accessibility. This new understanding of ionic liquid pretreatment paves the way for a formulation of the mechanistic requirements of pretreatment using simpler pretreatment liquors.

J. Viell et al., Multi-scale processes of beech wood disintegration and pretreatment with 1-ethyl-3-methylimidazolium acetate/water mixtures; Biotechnol. Biofuels 9:7 (2016)

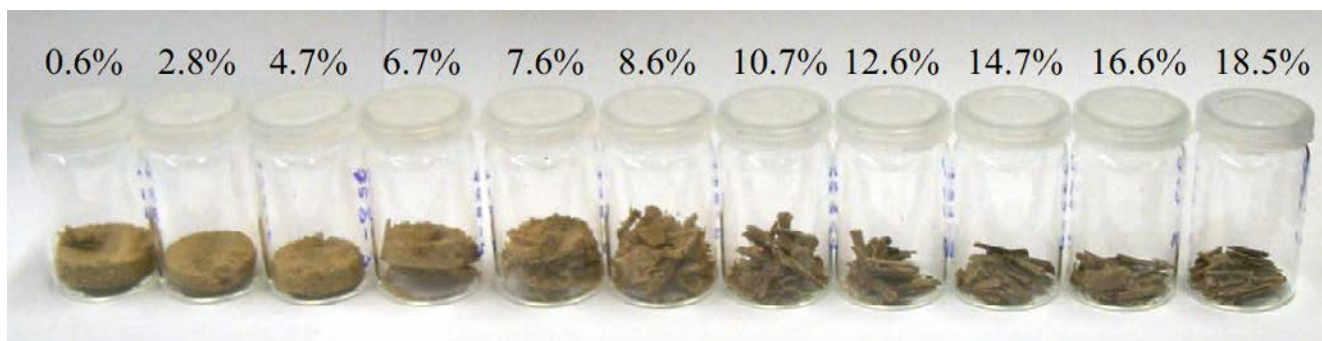


Figure 1: Morphology of beech chips pretreated in EMIMAc/water mixtures. The water content is given in wt%.

S. Jaksch¹, A. Schulz², Z. Di³, R. Luxenhofer⁴, R. Jordan², C. M. Papadakis¹¹Physik-Department, Technische Universität München, Garching, Germany; ²School of Science, Technische Universität Dresden, Dresden, Germany; ³Jülich Centre for Neutron Science (JCNS) at MLZ, Forschungszentrum Jülich GmbH, Garching, Germany; ⁴Functional Polymer Materials, Julius-Maximilians-Universität Würzburg, Würzburg, Germany

Self-assembled polymeric nanoparticles serve as pharmaceutical formulations to overcome the low water solubility of many commonly used drugs and to increase their residence time in the body. For this, a high loading capacity for the drug is desirable, and the carrier should not lead to side effects. Self-assembled micelles from amphiphilic block copolymers such as poly(2-oxazoline)s (POx) feature these advantageous properties: They exhibit very limited toxicity and complement activation, and show rapid renal clearance. Moreover, an exceptionally high loading capacity for hydrophobic drugs has been achieved for the cancer drug Paclitaxel (PTX) which is used to treat, among others, breast and ovarian cancer. Notably, the water solubility of PTX is very low, namely ~ 1 mg/L. This is particularly important as patients routinely receive approx. 400 mg during one chemotherapy session.

The POx system, among others, facilitates fine-tuning of the water solubility of the blocks. We have investigated triblock copolymers that have a weakly hydrophobic poly(*n*-butyl-2-oxazoline) (BuOx) middle block and hydrophilic poly(methyl-2-oxazoline) (MeOx) end blocks (Fig. 1a). $\text{PMeOx}_{33}\text{-}b\text{-PBuOx}_{26}\text{-}b\text{-PMeOx}_{45}$ (subscripts denote the degrees of polymerization). For comparison, similar triblock copolymers, but with strongly hydrophobic middle blocks, were also studied. Surprisingly, the loading capacity for drugs is maximal (more than 10,000 times higher than in pure water) for the system containing PBuOx, e.g. for a middle core-forming block that is only weakly (and not strongly) hydrophobic.

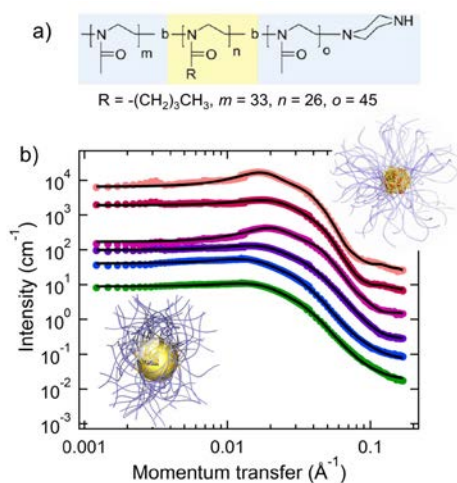


Figure 1: (a) Chemical structure of $\text{PMeOx}_{33}\text{-}b\text{-PBuOx}_{26}\text{-}b\text{-PMeOx}_{45}$. From ACS Nano 8, 2686 (2014), available at <http://pubs.acs.org/doi/abs/10.1021%2Fnn406388t>. Copyright 2014. Reproduced with the permission of the American Chemical Society. (b) Small-angle neutron scattering data from solutions of $\text{PMeOx}_{33}\text{-}b\text{-PBuOx}_{26}\text{-}b\text{-PMeOx}_{45}$ in D_2O (10 g L^{-1}) loaded with (from below) 0, 0.2, 0.9, 1.9, 4.2 and 4.8 g L^{-1} PTX. Insets: Structures of unloaded and PTX-loaded micelles. The PBuOx core is depicted in yellow, the PMeOx blocks in blue and PTX in red.

In order to explain the origin of this intriguing finding, we used small-angle neutron scattering (SANS) to analyse both the inner structure of the micelles themselves and the distribution of the drug in the micelle. Solutions of micelles from $\text{PMeOx}_{33}\text{-}b\text{-PBuOx}_{26}\text{-}b\text{-PMeOx}_{45}$ (subscripts denote degrees of polymerization) were prepared in D_2O to maximize the scattering contrast. The polymer concentration was kept at 10 g L^{-1} , while the concentration of PTX was varied in fine steps up to 4.8 g L^{-1} . SANS experiments were carried out on the KWS-1 instrument at sample-detector distances between 1.7 m and 19.7 m and a neutron wavelength of 6.9 \AA . Measuring times were between 15 min and 30 min.

The SANS data are shown in Fig. 1b. For PTX loadings up to 0.2 g L^{-1} , they were able to be fitted by a model for homogeneous spherical particles having a radius of $46\text{-}50\text{ \AA}$, which corresponds to the radius of the micellar core (lower inset of Fig. 1b). For PTX loadings of 0.9 g L^{-1} and above, this model did not describe the data adequately. Instead, it proved possible to use a model describing raspberry-like spherical particles. The radius of the micellar core was $53\text{-}61\text{ \AA}$ in the entire concentration range studied, and it is surrounded by small spheres (radius $12\text{-}17\text{ \AA}$).

Thus, the PTX molecules form small aggregates which are located near the interface between the PBuOx core and the PMeOx shell of the micelles (upper inset of Fig. 1). This peculiar distribution of the drug within the micelle (which was not observed in the system with strongly hydrophobic cores) may explain the exceptionally high PTX loading capacity of this type of micelles. Compared to other methods, such as transmission electron microscopy, SANS allows drug delivery systems to be studied in solution, and no preparatory steps, which may alter the structure of these delicate systems, are required. Thus, SANS is of great value in designing drug delivery systems with high therapeutic effect and minimum side effects.

The authors gratefully acknowledge financial support from the DFG (Pa771/6-2, Jo287/4-3) and the National Cancer Institute Alliance for Nanotechnology in Cancer (U01 CA116591).

S. Jaksch et al., *Amphiphilic Triblock Copolymers from Poly(2-oxazoline) with Different Hydrophobic Blocks: Changes of the Micellar Structures upon Addition of a Strongly Hydrophobic Cancer Drug*; *Macromol. Chem. Phys.* 217, 1448 (2016)

A. Koutsioumpas

Jülich Centre for Neutron Science (JCNS) at Heinz Maier-Leibnitz Zentrum (MLZ), Forschungszentrum Jülich GmbH, Garching, Germany

Biological lipid membranes represent an important self-assembly system in living organisms. In their most abundant form as the primary constituent of the cell membrane, they provide a bilayer fluid matrix for embedded membrane proteins that, in turn, regulate the cell's communication and its transport of chemical species. Biomembranes are immensely complex, containing mixtures of many different types of lipids, cholesterol and proteins. In biophysical studies, simpler counterparts consisting of a single or a few different lipid types are usually used.

The existence of methods that permit the reconstitution of model biomembranes on flat surfaces facilitates the use of a multitude of surface analytical experimental techniques for the study of their structure and dynamics. Among these techniques, neutron reflectometry is probably the most powerful probe of their structure. The special nature of neutrons enables them to penetrate deeply into materials, making them ideal probes for buried interfaces, such as membranes at the solid/liquid interface. Furthermore, the ability to manipulate contrast through the use of a deuterated solvent or lipids offers many possibilities for the extraction of structural information at the sub-nanometer level.

Traditionally, reflectivity data are compared to theoretical curves of simplified models consisting of stratified layers representing the hydrophilic parts, that is the lipid heads, and the hydrophobic parts – the lipid tails – of the membrane. The end result is a lateral averaged scattering length density (sld) profile that gives hints about the molecular dis-

tribution across the membrane. In our recent work, we have attempted to improve the interpretation of reflectivity data by the combined use of Molecular Dynamics (MD) and neutron reflectivity, so that the sld profiles correspond not to a mechanistic layer model, but to an objective representation of the system under study.

A set of neutron reflectivity measurements was obtained at the MARIA reflectometer, using DPPC supported membranes on Si substrates. This exact system was simulated using a coarse-grained (CG) MD approach based on the MARTINI force field. Then, the system parameters leading to an agreement between simulation and experiment were identified. Results indicate (Fig. 1) that, by carefully tuning CG simulations, we are able to reproduce the experimental behavior of the system both in the fluid and gel lipid phase. An analysis of the MD trajectories offers hints on the structural and dynamical details of the lipid systems. Finally, the successful application of this method paves the way for the investigation of more elaborate systems.

A large part of the “Soft Matter/Biology” experiments taking place at MARIA exploit the resolving power of neutrons for the study of model biomembranes. In the near future, we envisage the use of this approach for the elucidation of subtle structural features in experiments where membranes interact with proteins, small peptides, and nanoparticles that are candidates for drug delivery applications.

A. Koutsioubas, Combined Coarse-Grained Molecular Dynamics and Neutron Reflectivity Characterization of Supported Lipid Membranes; J. Phys. Chem. B 120, 11474 (2016)

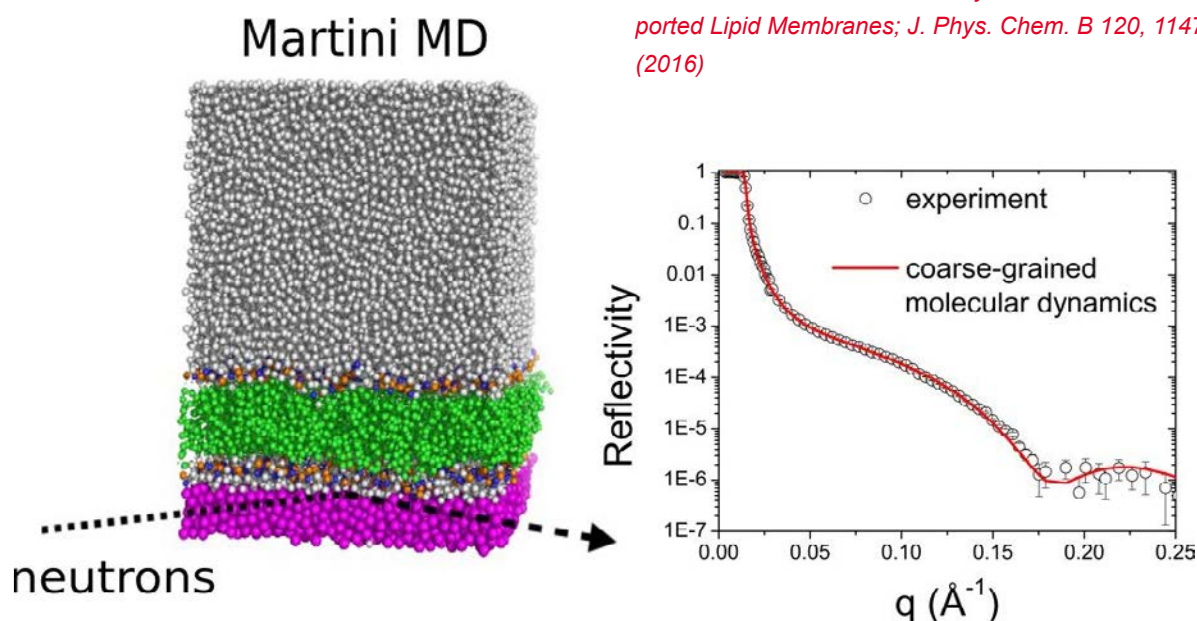


Figure 1: A typical molecular dynamics snapshot and comparison with the neutron reflectivity curves obtained (at a temperature above the liquid/gel lipid phase transition), where the agreement between simulation and experiment is showcased.

E. Metwalli¹, Y. Yao¹, J.-F. Moulin², M. Opel³, P. Müller-Buschbaum¹
¹Physik-Department, Lehrstuhl Funktionelle Materialien, Technische Universität München, Garching, Germany; ²German Engineering Materials Science Centre (GEMS) at MLZ, Helmholtz-Zentrum Geesthacht GmbH, Garching, Germany; ³Walther-Meißner-Institut, Bayerische Akademie der Wissenschaften, Garching, Germany

Block copolymers (BCs) are a special type of polymer that consists of two or more chemically different polymer blocks. They are able to self-assemble into various ordered nanostructures, such as spheres, cylinders, gyroids and lamellae, due to the chemical incompatibility of the polymer blocks. In thin films, BCs have the ability to create nano-scale templates that can be further employed to create nano-patterns of inorganic materials. For example, nanostructured BC films guide magnetic metal oxide nanoparticles (NPs) to create long-range ordered metal oxide nanopatterns, which are involved in the manufacture of nano-devices such as magnetic storage media, biosensor and solar cells. In this report, hybrid films composed of maghemite NPs and deuterated polystyrene-*block*-polybutylmethacrylate (PSd-*b*-PBMA) diblock copolymer were prepared via a simple coating step, followed by thermal annealing, to facilitate micro-phase separation and self-assembly processes.

One challenge is to determine the structure of such metal oxide/BC hybrid films along the film depth from the poly-

mer-substrate interface to the free air interface. The time-of-flight grazing incidence small angle neutron scattering (TOF-GISANS) technique is used to probe thin films at different film depths. TOF-GISANS has the advantage that it is capable of measuring simultaneously over a wide range of momentum transfer in a single experiment, without the need to alter the incident angle, the collimation or the sample-to-detector distance. In other words, TOF-GISANS permits several simultaneous GISANS measurements with different wavelengths (i.e. scattering vectors) in a single measurement. In TOF-mode, the neutron pulse with wavelengths of 0.2-2 nm can result in a dynamic range of the scattering vector which is 10 times larger than that of the monochromatic neutron beam. Thus, TOF-GISANS measurements were performed at the REFSANS instrument at the MLZ to investigate the lamella morphologies of different hybrid thin films. Two different film thicknesses of the hybrid films were used to achieve two different lamella orientations of the BC, parallel and perpendicular to the solid support (see Fig. 1).

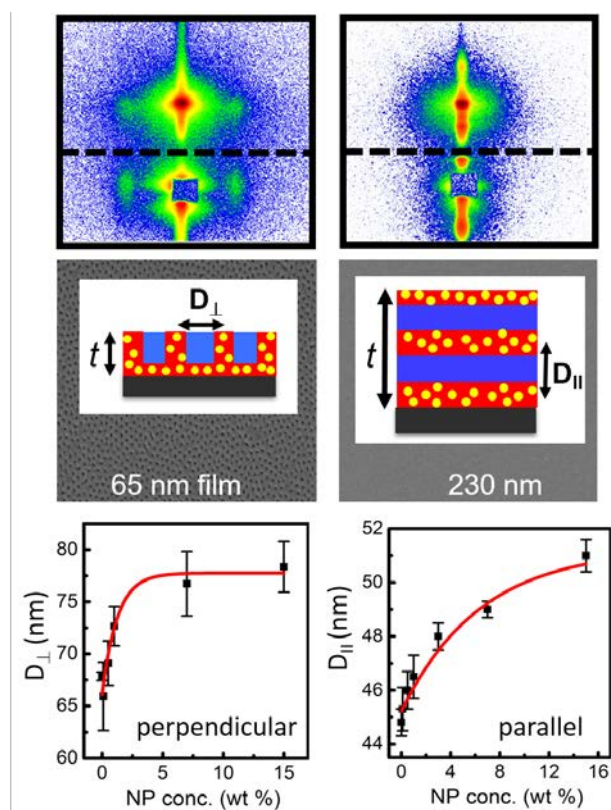


Figure 1: top row) 2D TOF-GISANS scattering patterns for both parallel and perpendicular lamella orientations, measured at a neutron wavelength of 0.47 nm. Middle row) Schematic representation of the nanostructured hybrid films overlaid with their respective SEM images showing the top surface structure. Bottom row) Inter-domain spacing D_{\perp} and D_{\parallel} as a function of the maghemite NP upload.

The TOF-GISANS results indicate an enrichment of NPs at the buried solid interface for both lamella orientations. Additionally, the dispersion stability of the PS-coated maghemite NPs in the nanostructured BC films is found to depend not only on the size of the NP employed, but also on the orientation of the PS nanodomains. For the perpendicular lamella in particular, a non-controlled aggregation of NPs compared with parallel lamella morphology is observed at low NP concentrations due to confinement effects. Such structural information gained with the help of TOF-GISANS measurements enabled us to better design and produce maghemite/BC hybrid films with optimized magnetically functional morphologies, proven using a superconducting quantum interference device magnetometer. The complementary results of real-space characterizations, including atomic force microscopy and scanning electron microscopy, are consistent with the observation obtained from the TOF-GISANS measurements. The perpendicular morphology is essential for devices such as magnetic storage systems in order to make simple storage and read-out possible. The parallel lamella morphology is better suited to magnetic sensor applications as it allows for higher magnetic saturation and remanence.

Y. Yao et al., *Hybrid Films: Lamellar Diblock Copolymer Films with Embedded Maghemite Nanoparticles*; *Adv Mater Interfaces* 3, (8), 1500712 (2016)

A. Tao¹, M. Meven²
¹Nanyang Technological University, School of Materials Science and Engineering, Singapore; ²Institute of Crystallography, RWTH Aachen University at MLZ and Jülich Centre for Neutron Science (JCNS) at MLZ, Garching, Germany

Rare earth silicates with apatite structure have been identified as promising materials as a solid electrolyte for solid oxide fuel cell (SOFC) applications, due to their superior ionic conductivity at intermediate temperatures (500 – 700 °C). Compared to conventional ionic conductors (such as yttria-stabilized zirconia) in which O²⁻ migrates via vacancies, they have a distinctive O²⁻ conduction mechanism via interstitial transport. While previous studies on these oxide interstitials have been limited to computational simulations, in the present work we have determined their location experimentally via neutron diffraction of Nd_{(28+x)/3}Al_xSi_{6-x}O₂₆ (0 ≤ x ≤ 1.5) single crystals. From these results, a dual-path conduction mechanism was deduced which provides the most thorough understanding of the O²⁻ transport mechanism to date, resulting in a systematic understanding of oxide ion migration in oxyapatites, insights which will be able to guide future performance optimization.

Looking into the crystal

Single crystal neutron diffraction was carried out on as-grown Nd_{9.33}Si₆O₂₆ crystals at 2 K and room temperature,

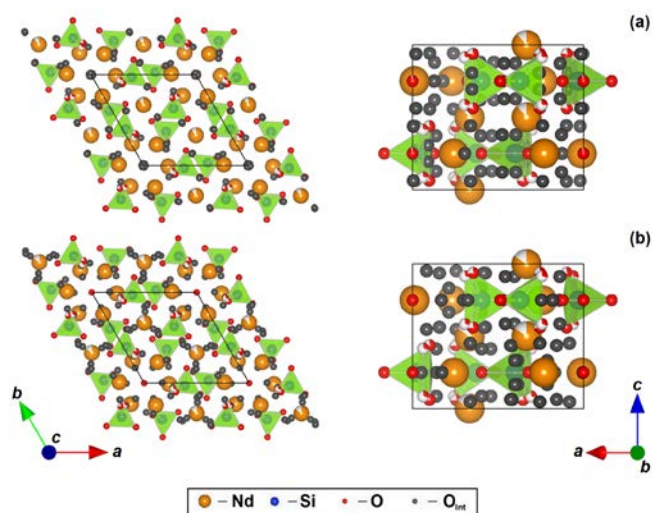


Figure 1: The concentration and distribution of oxygen interstitials in (a) as-grown Nd_{9.33}Si₆O₂₆ and (b) annealed Nd_{9.33}Si₆O₂₆ at room temperature viewed along [001] (left) and [010] (right).

and for an annealed Nd_{9.33}Si₆O₂₆ crystal (950 °C/3 months) at room temperature on the HEiDi hot single crystal diffractometer at the MLZ. A wavelength of 1.17Å combined with a high flux density of 1.2×10⁷ neutrons per second per cm² was obtained using an Er filter and a Ge (311) monochromator. Low temperatures were realised by a He closed-cycle cryostat mounted in the Eulerian cradle of the diffractometer. The crystal was wrapped in Al foil to minimize thermal losses and the temperature measured and controlled by a diode sensor near the heater to a stability of ± 0.1 K. The absolute temperatures were measured by an additional temperature sensor at the sample. The corrected integrated intensities of the reflections were calculated using PRON2K, and numerical absorption correction was performed with TBAR. The data collected have (sinθ/λ)_{max} > 0.72 and a total number of reflections > 3000. Corrections for the extinction effect were made in the refinements with Jana 2006.

From data to understanding mechanisms

The O²⁻ interstitial positions and concentrations at Fourier peaks of Nd_{9.33}Si₆O₂₆ (prior to and after annealing) are illustrated in Fig. 1. Tunnel interstitials in Nd_{9.33}Si₆O₂₆ migrate towards the framework after annealing, but the overall concentration of interstitials is significantly lower. This may be due to the presence of Si₂O₇ dimers in the framework, and the subsequent elimination of interstitials (O_i²⁻ + Si₂O₇⁶⁻ → 2SiO₄⁴⁻) after heat treatment. With this interstitial shift towards the framework and reduction in concentration due to long-term annealing, the dual-conduction path is disabled and O²⁻ migration along [001] is attenuated, which leads to the reduction in ionic conductivity as well as the removal of the inflection in the conductivity plot.

A. Tao et al., *Interstitial Oxide Ion Distribution and Transport Mechanism in Aluminum-Doped Neodymium Silicate Apatite Electrolytes*, *J. Am. Chem. Soc.* 138, 4468 (2016)

Phase diagram of Eu magnetic ordering in Sn-flux-grown $\text{Eu}(\text{Fe}_{1-x}\text{Co}_x)_2\text{As}_2$ single crystals

W. T. Jin^{1,2}, Y. Xiao¹, Z. Bukowski³, Y. Su², S. Nandi⁴, A. P. Sazonov^{2,5}, M. Meven^{2,5}, O. Zaharko⁶, S. Demirdis², K. Nemkovski², K. Schmalzl⁷, L. M. Tran⁸, Z. Guguchia⁸, E. Feng², Z. Fu², T. Brückel^{1,2}

¹Jülich Centre for Neutron Science (JCNS) and Peter Grünberg Institut, Forschungszentrum Jülich GmbH, Jülich, Germany; ²Jülich Centre for Neutron Science (JCNS) at MLZ, Forschungszentrum Jülich GmbH, Garching, Germany; ³Institute of Low Temperature and Structure Research, Polish Academy of Sciences, Wrocław, Poland; ⁴Department of Physics, Indian Institute of Technology, Kanpur, India; ⁵Institut für Kristallographie, RWTH Aachen, Aachen, Germany; ⁶Laboratory for Neutron Scattering and Imaging, Paul Scherrer Institut, Villigen, Switzerland; ⁷Jülich Centre for Neutron Science (JCNS) at Institut Laue-Langevin (ILL), Forschungszentrum Jülich GmbH, Grenoble, France; ⁸Laboratory for Muon Spin Spectroscopy, Paul Scherrer Institut, Villigen, Switzerland

The discovery of superconductivity in iron pnictides in 2008 has provided new opportunities to study the interplay between superconductivity and magnetism. EuFe_2As_2 is a unique family among the iron pnictides as it contains two magnetic sublattices. Superconductivity can be achieved in this system by suppressing the spin-density-wave (SDW) ordering of Fe by chemical substitution. Nevertheless, for an electron-doped $\text{Eu}(\text{Fe}_{1-x}\text{Co}_x)_2\text{As}_2$ system, reports about its physical properties remain quite controversial.

In order to establish a specific phase diagram of $\text{Eu}(\text{Fe}_{1-x}\text{Co}_x)_2\text{As}_2$ that describes its physical properties, we performed complementary macroscopic and neutron diffraction measurements on a series of Sn-flux grown single crystals with different Co-doping levels. The neutron diffraction measurements were performed on HEiDi and DNS at the MLZ, TriCS at PSI, and D23 at ILL.

Fig. 1 illustrates how the ground-state magnetic structure of $\text{Eu}(\text{Fe}_{1-x}\text{Co}_x)_2\text{As}_2$ evolves with the Co concentration. For $x \leq 0.053$, the Eu^{2+} moments maintain the alignment within

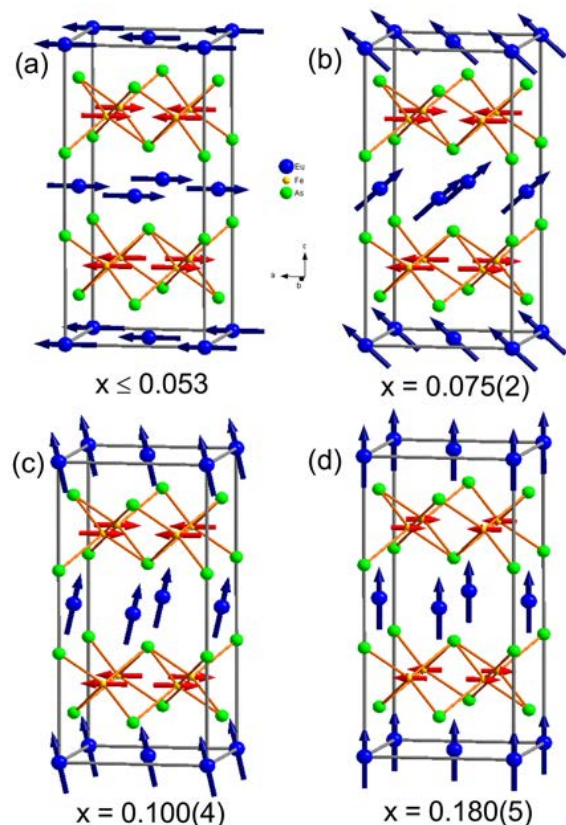


Figure 1: The ground-state magnetic structure of $\text{Eu}(\text{Fe}_{1-x}\text{Co}_x)_2\text{As}_2$ with $x \leq 0.053$ (a), $x = 0.075(2)$ (b), $x = 0.100(4)$ (c), and $x = 0.180(5)$ (d), as determined by single-crystal neutron diffraction.

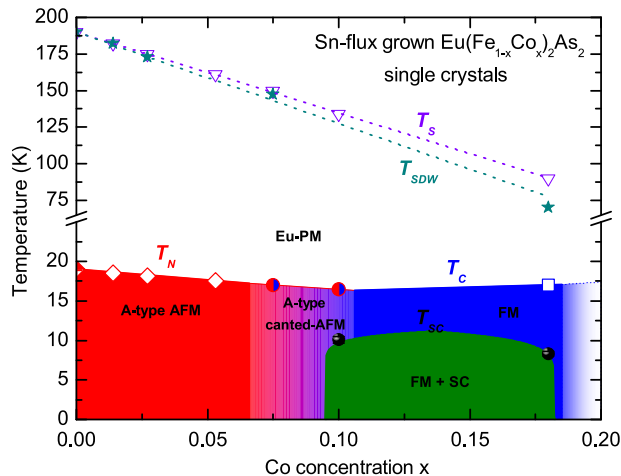


Figure 2: The phase diagram of Sn-flux-grown $\text{Eu}(\text{Fe}_{1-x}\text{Co}_x)_2\text{As}_2$ single crystals.

the ab plane in the A-type AFM order. When the Co-doping level is further increased, the Eu^{2+} spins start to rotate toward the c axis within the ac plane, exhibiting the A-type canted AFM structure with a net FM moment component along the c direction. At base temperature, the canting angle of the Eu^{2+} spins out of the ab plane increases with Co-doping, from $23.8(6)^\circ$ for $x = 0.075(2)$, to $\sim 65^\circ$ for $x = 0.100(4)$ and finally to 90° for $x = 0.180(5)$, showing a pure FM order of Eu.

The phase diagram of $\text{Eu}(\text{Fe}_{1-x}\text{Co}_x)_2\text{As}_2$ has been constructed and shown in Fig. 2. Both the structural phase transition (T_S) and the SDW transition of Fe (T_{SDW}) are continuously suppressed by Co-doping. The magnetic ground state of the Eu^{2+} moments depends strongly on the Co-doping level. The doping-induced modification of the indirect Rutherford-Kittel-Kasuya-Yosida (RKKY) interaction between the Eu^{2+} moments, which is mediated by the conduction d electrons on the $(\text{Fe},\text{Co})\text{As}$ layers, as well as the change in the strength of the direct interaction between the Eu^{2+} and Fe^{2+} moments, is believed to be responsible for the change in the magnetic ground state and the ordering temperature of Eu. In addition, for $\text{Eu}(\text{Fe}_{1-x}\text{Co}_x)_2\text{As}_2$ with $0.10 \leq x \leq 0.18$, strong ferromagnetism from the Eu sublattice is well developed in the superconducting state, where a spontaneous vortex state is expected to account for the compromise between the two competing phenomena.

W. T. Jin et al., Phase diagram of Eu magnetic ordering in Sn-flux-grown $\text{Eu}(\text{Fe}_{1-x}\text{Co}_x)_2\text{As}_2$ single crystals; *Phys. Rev. B* **94**, 184513 (2016)

A. Sazonov^{1,2}, V. Hutanu^{1,2}, M. Meven^{1,2}, G. Roth¹, I. Kézsmárki³, H. Murakawa⁴, Y. Tokura^{4,5}, B. Náfrádi⁶

¹Institute of Crystallography, RWTH Aachen University, Aachen, Germany; ²Jülich Centre for Neutron Science at MLZ, Forschungszentrum Jülich GmbH, Garching, Germany; ³Department of Physics and Magneto-Optical Spectroscopy Research Group, Budapest University of Technology, Budapest, Hungary; ⁴Multiferroics Project, ERATO, Japan Science and Technology Agency, University of Tokyo, Tokyo, Japan; ⁵Department of Applied Physics and Quantum Phase Electronics Center, University of Tokyo, Tokyo, Japan; ⁶École Polytechnique Fédérale de Lausanne, Laboratory of Nanostructures and Novel Electronic Materials, Lausanne, Switzerland

Recently, $\text{Ca}_2\text{CoSi}_2\text{O}_7$ melilite has been found to be multiferroic, exhibiting static as well as dynamic magnetoelectric effects. It has also been shown that the main features of the magnetoelectric behaviour of melilites can be predicted by symmetry considerations, without appealing to any specific atomic mechanism. Thus, for a symmetry-consistent theoretical description of the multiferroic phase, precise knowledge of the crystal structure is a prerequisite. However, for many melilite systems, there is still a lack of low-temperature structural details.

In order to remedy the deficiency in low-temperature structural information on $\text{Ca}_2\text{CoSi}_2\text{O}_7$ and provide reliable data for further experimental and theoretical research, we performed single-crystal neutron diffraction measurements at temperatures between 10 K and 250 K. The studies were carried out on the four-circle diffractometer HEiDi at the hot-neutron source of the FRM II reactor, using a wavelength $\lambda = 1.169 \text{ \AA}$.

Group-theoretical calculations show that only two subgroups of the high-temperature tetragonal space group (SG) $P\bar{4}2_1m$ (No. 113 according to Int. Tables Cryst.) can describe observed low-temperature modulation of the melilite structure. These are the tetragonal SG $P\bar{4}$ (No. 81) and the orthorhombic SG $P2_12_12$ (No. 18). Based on X-ray diffraction experiments, arguments for both SG have been put forward. The choice of SG $P\bar{4}$ was based on the observation of the (h00) and (0k0) type reflections with h and $k = 2n + 1$, which are forbidden in $P2_12_12$. A few extremely weak reflections of the same type were also present in our neutron data. A detailed analysis of both the measured peak profiles and integrated intensities reveals the multiple diffraction origin of those reflections. We have selected SG $P2_12_12$ as the most appropriate model to describe the neutron diffraction data of $\text{Ca}_2\text{CoSi}_2\text{O}_7$ at 10 K. Our choice is based on the:

- greater reliability factors in $P\bar{4}$ (Fig. 1),

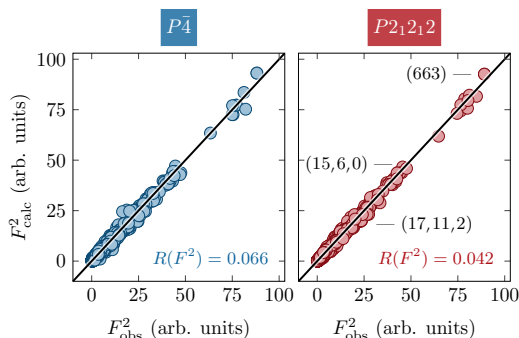


Figure 1: The quality of the crystal structure refinement in SG $P\bar{4}$ (left panel) and SG $P2_12_12$ (right panel). The experimentally measured structure factors (F^2_{obs}) are plotted against the calculated ones (F^2_{calc}).

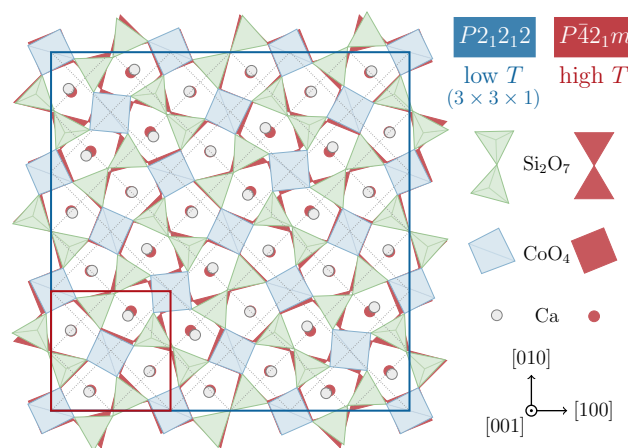


Figure 2: Comparison of the low-temperature commensurately modulated lock-in state ($3 \times 3 \times 1$ supercell, SG $P2_12_12$) with the high-temperature unmodulated phase (SG $P\bar{4}2_1m$), according to our neutron diffraction data at 10 K and X ray diffraction at 500 K quoted in the literature, respectively.

- non-physical values of atomic displacement parameters in $P\bar{4}$,
- multiple diffraction origin of the observed reflections forbidden in $P2_12_12$.

Fig. 2 shows a comparison of the low-temperature commensurately modulated lock-in state ($3 \times 3 \times 1$ supercell, SG $P2_12_12$) with the high-temperature unmodulated phase (SG $P\bar{4}2_1m$), according to our neutron diffraction data at 10 K and literature X-ray diffraction at 500 K, respectively. Clear shifts of the atoms are visible, especially for Ca and O. A comparison of the structure at 10 K with that derived within the same model (SG $P2_12_12$ from X-ray diffraction at 170 K) shows a much smaller difference in the positional parameters, with an average value of $\sim 1\sigma$; The average shift is less than 0.014 \AA . Thus, we can conclude that the crystal symmetry is preserved from 170 K down to at least 10 K.

In conclusion, the crystal structure of multiferroic melilite $\text{Ca}_2\text{CoSi}_2\text{O}_7$ has been accurately determined by single-crystal neutron diffraction at 10 K, just above the antiferromagnetic phase transition temperature $T_N \approx 5.7 \text{ K}$. The structural parameters reported can serve as a solid experimental and theoretical basis from which to develop microscopic models describing the multiferroic nature and the peculiar magnetoelectric phenomena in melilites.

A. Sazonov et al., *The low-temperature crystal structure of the multiferroic melilite $\text{Ca}_2\text{CoSi}_2\text{O}_7$* , *Acta. Crystallogr. B* **72**, 126 (2016)

D. Wiedemann¹, S. Indris², M. Meven³, B. Pedersen⁴, H. Boysen⁵, R. Uecker⁶, P. Heitjans⁷, M. Lerch¹

¹Institut für Chemie, Technische Universität Berlin, Berlin, Germany; ²Institut für Angewandte Materialien (IAM-ESS), Karlsruher Institut für Technologie, Eggenstein-Leopoldshafen, Germany; ³Institut für Kristallographie, RWTH Aachen and Jülich Centre for Neutron Scattering (JCNS) at Heinz Maier-Leibnitz Zentrum (MLZ), Garching, Germany; ⁴Heinz Maier-Leibnitz Zentrum (MLZ), Garching, Germany; ⁵Sektion Kristallographie, Ludwig-Maximilians-Universität München, München, Germany; ⁶Leibniz-Institut für Kristallzüchtung, Berlin, Germany; ⁷Institut für Physikalische Chemie und Elektrochemie and ZFM – Zentrum für Festkörperchemie und Neue Materialien, Leibniz Universität Hannover, Hannover, Germany

Despite many actual and proposed uses for solid lithium-ion conductors (foremost in energy storage), transport phenomena within them are still poorly understood at a fundamental level. The crucial role of the latter in applications is the reason for our interest in γ -LiAlO₂, as it is a so-called “ultraslow” three-dimensional conductor. Neutron diffraction is an ideal method for spatially mapping diffusion pathways (and evaluating associated energy barriers), because it (a) is sensitive to the notoriously elusive lithium ions and (b) can be carried out at the high temperatures that are necessary to activate migration.

Our research on γ -LiAlO₂ (tetragonal, space group: $P4_32_1/P4_32_1$) began with the evaluation of two datasets, which had been acquired using the single-crystal diffractometers RESI at 25(2) °C and HEiDi at 770(5) °C in their earlier days. The room-temperature data provided us with a crystal-structure model that included anisotropic displacement parameters for all ion positions (see Fig. 1). In this way, we not only added precision to a previous determination dating from 1965, but also excluded any significant disorder at 25 °C. The high-temperature data, on the other hand, were considerably more troublesome: during the measurement, the crystal had slipped—probably due to teething troubles with the instrumental setup. Nevertheless, we overcame the resulting mismeasurements using rigorous data exclusion and subsequently applying maximum-entropy methods (MEM) for the evaluation.

In this case, MEM yield the maximum variance in the calculated structure factors within standard deviations of the observed structure factors. This means that we extract *minimal information* within the limits of observational uncertainty to minimize artifacts and avoid misinterpretation. The result

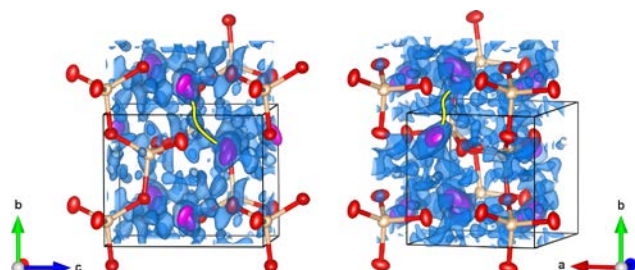


Figure 2: MEM-reconstructed negative scattering-length density (SLD) at 770 °C in two orientations. Pink: lithium, other: aluminium, red: oxide ions (ellipsoids of 75 % probability), blue: isosurface for $-0.0375 \cdot 10^{-6} \text{ fm pm}^{-3}$, yellow: proposed lithium diffusion pathway, black: unit cell.

is a map of the scattering-length density (SLD; the neutron equivalent of the electron density known from X-ray diffraction), in which lithium-ion migration manifests as a smearing of the time-averaged negative SLD. From such a map (see Fig. 2), we identified a strongly curved pathway between adjacent lithium positions as the most probable one. This finding was of high heuristic value for further studies on powders at even higher temperatures, which ultimately led to corroboration of the initial allusion premise.

This work was supported by the Deutsche Forschungsgemeinschaft (research unit FOR 1277: “Mobility of Lithium Ions in Solids”).

D. Wiedemann et al., Single-crystal neutron diffraction on γ -LiAlO₂: structure determination and estimation of lithium diffusion pathway; Z. Kristallogr. – Cryst. Mater. 231, 189 (2016)

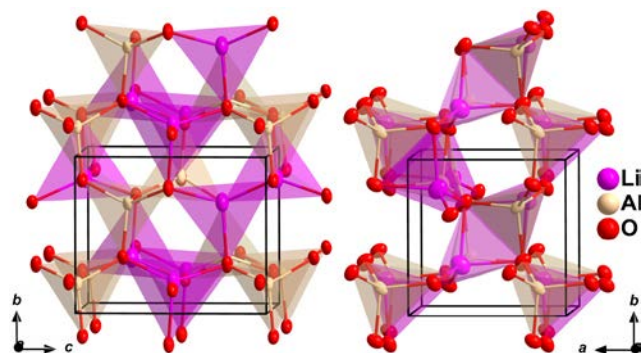


Figure 1: Crystal structure of γ -LiAlO₂ at 25(2) °C. Ellipsoids of 90 % probability, unit cell in black.

G. D. Gatta¹, M. Meven²

¹Dipartimento di Scienze della Terra, Università degli Studi di Milano, Milan, Italy; ²Institute of Crystallography, RWTH Aachen University, and Jülich Centre for Neutron Science (JCNS) at MLZ, Garching, Germany

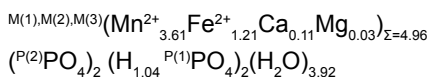
Understanding rock formation

Phosphate minerals represent the major host for transition metals and H₂O in pegmatitic rocks. (Fe,Mn)-phosphates play an essential geochemical role in the evolution processes affecting pegmatites. Hureaulite is a late-stage secondary phosphate mineral. Its formation occurs mainly in Ta- and Li-enriched pegmatites, which are highly interesting as they are a natural source of the strategic elements Ta and Nb. So far, knowledge of the crystal chemistry of hureaulite has been restricted to a few studies based on X-ray data that agree in the monoclinic space group (C2/c) and metrics, but show different possible crystal-chemical formulae, with the presence of the H₃O⁺ ion but no clear evidence for the presence of the HOPO₃²⁻ groups.

To resolve these open questions, we have reinvestigated the crystal structure of hureaulite using single-crystal neutron diffraction.

Looking into the matter

Pale pink crystals of natural hureaulite from Minas Gerais, Brazil, were used for this study. The chemical composition was determined by EPMA-WDS analysis:



A single crystal neutron diffraction experiment was carried out on the diffractometer HEiDi at the MLZ at 2.3 K, $\lambda=1.1680(2)$ Å. A total number of 2078 reflections was collected with $R_{\text{int}} = 0.0591$, refined unit-cell parameters $a = 17.466(6)$ Å, $b = 9.104(5)$ Å, $c = 9.457(4)$ Å, $\beta = 96.33(6)^\circ$. The anisotropic structure refinement took as its starting point the atomic coordinates of previous studies without H sites, with the scattering length $b(\text{P})$ for the two

independent tetrahedral sites $P(1)$, $P(2)$, and with mixed $b(\text{Fe}+\text{Mn})$ lengths corresponding to the fractions of Fe and Mn for each of the three independent octahedral sites $M(1)$, $M(2)$ and $M(3)$. Five negative residual peaks were found in the difference-Fourier map of nuclear density and assigned to H. The final refinement cycle had no peaks larger than ± 1.0 fm/Å³ in the difference-Fourier map and an agreement index of $R_1(F_{\text{obs}} > 4\sigma(F_{\text{obs}})) = 0.0747$ (167 free parameters, 707 unique reflections).

Locating the protons in hureaulite

The results of this first study on hureaulite using neutron diffraction data confirm the previous structure model from X-ray data, with $\text{P}^{(2)}\text{PO}_4$ and $(\text{HO}^{\text{P}^{(1)}}\text{PO}_3)$ units and groups of edge-sharing $M^{(1)}\text{MO}_6$, $M^{(3)}\text{MO}_5(\text{H}_2\text{O})$ and $M^{(2)}\text{MO}_4(\text{H}_2\text{O})_2$ units. No “zeolitic” H₂O molecules occur. In addition, our data reveal five independent H sites in hureaulite with full site occupancy, one of them as a member of the unique hydroxyl group of the structure (O(1)-H(1)), the other four belonging to H₂O molecules (H(2)-O(9)-H(3) and H(4)-O(10)-H(5)) (Fig. 1) with fairly anisotropic displacement parameters. The complex H bonding scheme contains five energetically favorable hydrogen bonds; the strongest one involves the hydroxyl group, i.e., O(1)-H(1)⋯O(8); the other four bonds the H₂O molecules; O(3)⋯H(2)-O(9)-H(3)⋯O(3) and O(1)⋯H(4)-O(10)-H(5)⋯O(8). In contrast to earlier studies, we have clearly shown that hureaulite contains the HOPO₃²⁻ anion but no H₃O⁺.

G. Diego Gatta et al., Single-crystal neutron diffraction and Mössbauer spectroscopic study of hureaulite, $(\text{Mn,Fe})_5(\text{PO}_4)_2(\text{HPO}_4)_2(\text{H}_2\text{O})_4$; *Eur. J. Mineral.* 28, 93 (2016)

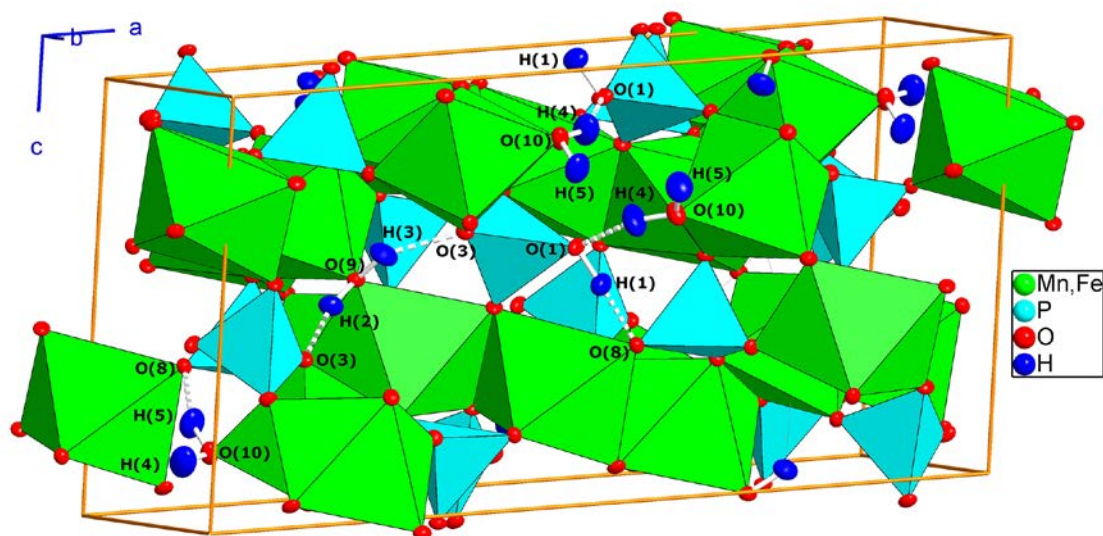


Figure 1: Clinographic view of the crystal structure of hureaulite, based on neutron structure refinement.

T. Reimann^{1,2}, S. Mühlbauer¹, B. Betz³, P. Böni², M. Schulz^{1,2}

¹Heinz Maier-Leibnitz Zentrum (MLZ), Technische Universität München, Garching, Germany, ²Physik-Department, Technische Universität München, Garching, Germany; ³Neutron Imaging and Activation Group, Paul Scherrer Institut, Villigen, Switzerland

Neutron Grating Interferometry (nGI) is an advanced method in neutron imaging that is based on two neutron absorption gratings and one phase grating implemented in an existing neutron imaging beamline. The nGI-technique permits the simultaneous recording of the transmission, the differential phase and the dark-field image. Hence, by means of nGI, neutron phase shift and neutron scattering provide additional contrast modalities in order to both distinguish materials of similar transmission and to image pure magnetic structures such as e.g. ferromagnetic domains.

The dark-field image (DFI), in particular, has recently been the subject of much interest, since it has been realized that its contrast not only marks scattering within the sample but that, furthermore, its value is directly linked to the differential scattering cross-section of the underlying microstructure. By performing nGI investigations for different neutron energies (denoted as quantitative dark-field imaging) or sample-to-grating rotation angles (known as directional dark-field imaging), information on the microstructure such as local structure sizes or textures can consequently be obtained, while the spatial resolution is insufficient to map the microstructure directly.

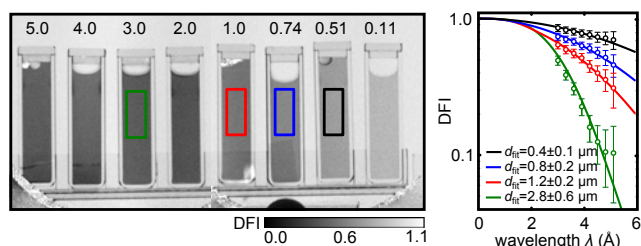


Figure 1: Quantitative dark-field imaging. Left: Dark-field image of eight cuvettes filled with 10 % polystyrene particles of different diameter solved in H₂O/D₂O. The diameters (μm) are given in the picture. Although the chemical composition is equal for each sample, their dark-field contrast differs strongly. Right: Contrast for the positions marked in the dark-field image as a function of the neutron wavelength. The particle diameters d_{fit} are recovered by fitting the data to theory.

The capabilities of these new approaches in neutron imaging have been demonstrated at the ANTARES beamline. In particular, the theoretical description of the dark-field contrast has been verified for a simple model system of diluted polystyrene particles (see Fig. 1) and later extended in order to study the complex domain structure arising in superconducting niobium. A further evaluation of the sample's microstructure can be provided by directional dark-field imaging (Fig. 2). For this purpose, the setup at ANTARES is unique, since it allows the simultaneous rotation of all gratings which, in turn, allows for the combination of this new experimental approach with heavy and bulky sample environments.

In conclusion, the nGI approaches introduced provide a means of obtaining quantitative information on the local microstructure of a sample and are thus highly complementary to well-established methods such as small and ultra-small-angle scattering. The methods are of especially high impact for local investigations of modulated phases arising in e.g. ferromagnetic, multiferroic or superconducting domain systems.

T. Reimann et al., The new neutron grating interferometer at the ANTARES beamline: design, principles and applications; J. Appl. Cryst. 49, 1488 (2016)

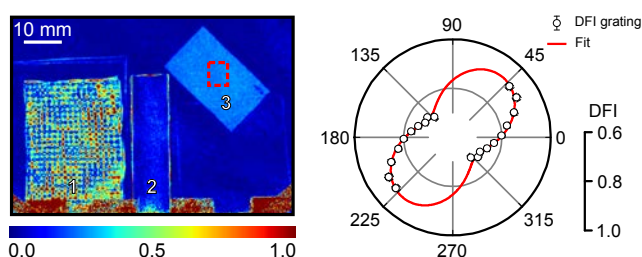


Figure 2: Left: Dark-field anisotropy map of a glass fiber mat (1), a copper rod (2) and a 4 μm Gd grating (3). Image quantifying the local anisotropy of the microstructure. While Cu is isotropic, the grating is anisotropic and the woven structure consists of a regular pattern of anisotropic and isotropic regions. Right: The contrast variation (in the red marked region) for different sample-to-grating rotations reveals minimal scattering along 55°.

S. Mühlbauer¹, A. Heinemann², S. Busch², A. Wilhelm¹, A Backs¹, H. Weiss³

¹Heinz Maier-Leibnitz Zentrum (MLZ), Technische Universität München, Garching, Germany; ²German Engineering Materials Science Center (GEMS) at MLZ, Helmholtz-Zentrum Geesthacht GmbH, Garching, Germany; ³Lehrstuhl für Umformtechnik und Gießereiwesen (UTG), Technische Universität München, Garching, Germany

Time resolved stroboscopic neutron scattering and TISANE (Time Involved Small Angle Neutron Experiments) are based on the cyclic perturbation of the sample with an external control parameter, i.e. the measurements are repeated for many cycles of the control parameter, where the data obtained for the individual cycles is summed. The time resolved response of the sample to the external control parameter is measured in such experiments. While the time frame of stroboscopic neutron scattering typically ranges from minutes to ms, TISANE benefits hugely from a neutron chopper system and makes it possible to access μs time scales. However, a crucial point for the successful use of both stroboscopic neutron scattering and TISANE is the careful choice of the external control parameter.

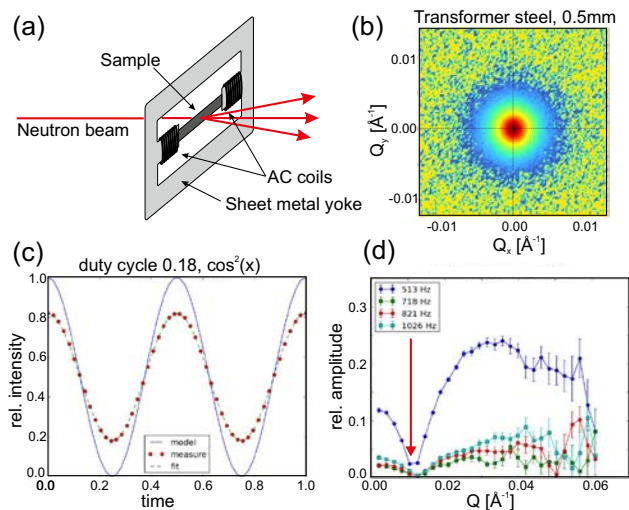


Figure 1: (a) Schematic setup of the TISANE experiment at transformer steels. An oscillating AC field between 50Hz and 1000Hz is applied to the sample. The scattering intensity is recorded with μs time resolution. (b) Typical scattering pattern at a wavelength of 12 \AA and SD of 20m. For each pixel, the oscillation of the signal is fitted, yielding offset and relative amplitude of the intensity. (c) Folding of the expected \cos^2 signal with a duty cycle of 0.18. (d) Relative amplitude of the oscillation for different frequencies from 500Hz to 1000Hz AC-field as function of Q . It should be noted that the red marker indicates a phase shift of 180°.

Following a first set of successful experiments in autumn 2016, a dedicated TISANE setup has finally been commissioned at the small angle neutron scattering instrument SANS-1 at the MLZ. The TISANE project was jointly realized by the TUM and HZG. It consists of a cutting edge double disk neutron chopper (AIRBUS) with magnetic bearings and a maximal speed of 20.000 rpm. The chopper is located in front of the collimator section of SANS-1 in a newly built common shielding with the velocity selectors. The chopper discs can be co- or counter-rotated. 14 equal cutouts, in combination with an adjustable aperture, allow for a broad range of pulse shapes to tune both the resolution and intensity to the needs of the experiment. For a Q -range of 0.07 \AA^{-1} - 0.4 \AA^{-1} , maximal sample frequencies in the order of 20 kHz can be achieved. Moreover, a successful TISANE setup imposes tight restrictions on the synchronization of the chopper, sample oscillation and neutron data acquisition in the event mode.

In a first experiment, the frequency dependence of sheet metal steel (transformer alloy) with a thickness of 0.5 mm was examined in a frequency range of up to 1000 Hz. The experimental setup and typical data are shown in Fig. 1. The TISANE setup is now ready for user experiments over a broad range of applications ranging from driven vortex and skyrmion motion in magnetic systems, ferrofluids and magnetic domain dynamics to shear induced ordering phenomena in polymers.

The realization of the TISANE setup @ SANS-1 would not have been possible without the technical support of the HZG and TUM: In particular, we would like to thank A. Beldowski, G. Musilak, J. Borchers, O. Listing and D. Heims from the HZG Technikum and U. Reineke and S. Semecky from the TUM.

S. Mühlbauer et al., Kinetic small angle neutron scattering of the skyrmion lattice in MnSi; New J. Phys. 18(7), 075017 (2016)

R. B. Firestone¹, Z. Révay²

¹University of California, Department of Nuclear Engineering, Berkeley, California, USA; ²Heinz Maier-Leibnitz Zentrum (MLZ), Technische Universität München, Garching, Germany

Precisely known radiative thermal neutron cross sections are important for elemental analysis by Prompt Gamma-ray Activation Analysis (PGAA). The cross sections of the light elements are especially important due to the high abundance of these elements in nature. In this work, we have completed the precise determination of γ -ray and total radiative cross sections for ^2H , $^6,^7\text{Li}$, ^9Be , $^{10,11}\text{B}$, $^{12,13}\text{C}$, $^{14,15}\text{N}$, and $^{16,17,18}\text{O}$. We have also measured new, precise neutron separation energies for these neutron capture isotopes. This work provides the first complete cross section analysis of the light elements with $Z = 1,3-8$, including all of their stable isotopes.

Prompt γ -rays from enriched isotopic targets were measured using the PGAA experimental facilities at the FRM II and Budapest Reactors. The γ -rays were detected with n-type high-purity, 60 % efficient germanium detectors surrounded by a bismuth germanate scintillator Compton suppression system. A lead collimator was placed in front of the detector to collimate the γ -rays, generated by the neutron beam, onto the detector. Counting efficiency was calibrated from 50 keV to 10 MeV with radioactive sources and (n, γ) reaction γ -rays to a precision of better than 1 % from 0.5-6 MeV and better than 3 % at all other energies. The γ -ray spectra were analyzed with the Hypermet PC peak analysis code. Cross section standardization of the γ -ray spectra was performed with respect to the $^1\text{H}(n,\gamma)$ 2223-keV γ -ray cross section, $\sigma_\gamma = 0.3325(7)$ b, using either stoichiometric compound targets containing ^1H or other elements previously calibrated using ^1H .

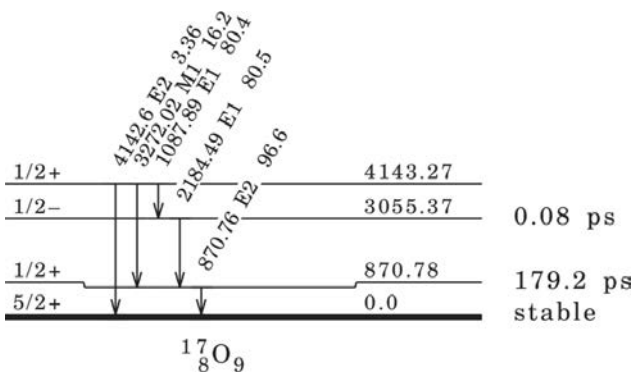


Figure 1. Level scheme showing level and γ -ray energies and transition probabilities for the $^{16}\text{O}(n,\gamma)^{17}\text{O}$ measurement.



Figure 2: The new PGAA instrument at the MLZ is typically used for the determination of the elemental composition of solid samples, liquids and even gaseous samples.

Reaction	σ_0 (mb) (this work)	σ_0 (mb) (Mughab- ghab)	S_n (this work)	S_n (Wang et al)
$^1\text{H}(n,\gamma)^2\text{H}$	$\approx 332.6(7)$	332.6(7)	-	2224.5660(4)
$^2\text{H}(n,\gamma)^3\text{H}$	489(6)	508(15)	-	6257.2328(23)
$^6\text{Li}(n,\gamma)^7\text{Li}$	39.3(7)	38.5(30)	7250.67(21)	7251.09(1)
$^7\text{Li}(n,\gamma)^8\text{Li}$	44.3(5)	45.4(27)	2032.564(19)	2032.52(5)
$^9\text{Be}(n,\gamma)^{10}\text{Be}$	8.27(13)	8.49(34)	6812.13(4)	6812.28(5)
$^{10}\text{B}(n,\gamma)^{11}\text{B}$	394(15)	305(16)	11454.02(10)	11454.12(16)
$^{11}\text{B}(n,\gamma)^{12}\text{B}$	9.09(10)	5.5(33)	3368.87(16)	3368.87(14)
$^{12}\text{C}(n,\gamma)^{13}\text{C}$	3.87(3)	3.53(7)	3368.87(6)	4946.3084(5)
$^{13}\text{C}(n,\gamma)^{14}\text{C}$	1.496(18)	1.37(4)	8176.61(8)	8176.43
$^{14}\text{N}(n,\gamma)^{15}\text{N}$	80.0(4)	80.1(6)	10833.22(5)	10833.2951(8)
$^{15}\text{N}(n,\gamma)^{16}\text{N}$	0.0396(14)	0.024(8)	-	2488.8(23)
$^{16}\text{O}(n,\gamma)^{17}\text{O}$	0.170(3)	0.190(19)	4143.27(13)	4143.079(1)
$^{17}\text{O}(n,\gamma)^{18}\text{O}$	0.67(7)	0.538(65)	8046.06(10)	8045.369(1)
$^{18}\text{O}(n,\gamma)^{19}\text{O}$	0.141(6)	0.16(1)	3963.12(19)	3955.6(26)

Table 1: Total radiative thermal neutron cross sections and neutron separation energies measured in this work.

Complete neutron capture decay schemes, as shown in Fig. 1, were determined for all of the isotopes measured in these experiments. The adopted γ -ray energies were determined by a least-squared fit of the measured transition energies to the decay scheme level energies. This fit also gave a precise determination of the neutron separation energy. Transition cross sections were also a least-squared fit to the level scheme assuming that the total cross section deexciting the capture state equals that feeding the ground state, and that cross sections feeding and deexciting of intermediate states are equal. Our final results are summarized in Tab. 1 and have been published in Physical Review C.

R. B. Firestone and Zs. Révay, *Phys. Rev. C* 93, 044311, 054306 (2016)

M. Dickmann¹, J. Mitteneder², G. Kögel², G. Dollinger², W. Egger², C. Piochacz¹, P. Sperr², S. Vohburger¹, C. Hugenschmidt¹

¹Heinz Maier-Leibnitz Zentrum (MLZ) and Physik-Department, Technische Universität München, Garching, Germany; ²Institut für Angewandte Physik und Messtechnik, Universität der Bundeswehr München, Neubiberg, Germany

The scanning positron microscope (SPM) at the Universität der Bundeswehr München caters for spatially-resolved positron annihilation lifetime spectroscopy (PALS). In order to overcome the long measurement times of several days per sample involved when using a conventional ²²Na positron source, the SPM has currently been transferred to the intense positron source NEPOMUC. As a prerequisite, a special SPM-interface has been built and installed to adapt the NEPOMUC beam to the stringent requirements of position resolved PALS. This interface includes several bunching components to pulse the beam for lifetime measurements. An additional re-moderation stage is used to convert the 2 mm (FWHM) diameter NEPOMUC beam into a high brightness positron micro-beam of about 200 μm diameter.

A newly built sample chamber has been attached to the exit of the SPM interface. Deflecting coils make it possible to scan the beam over a sample area of about $2 \times 2 \text{ mm}^2$. With this setup, we have been able to characterize the positron micro-beam and finally perform the first spatially-resolved PALS measurements at the FRM II.

To determine the beam size, a sample consisting of two materials with considerably different average positron lifetimes is necessary. Therefore, copper grids with quadratic spacings of $425 \times 425 \mu\text{m}^2$ and bar widths of $83 \mu\text{m}$ were placed on carbon tape. The 1.5 keV kinetic energy beam was magnetically focused and scanned over an area of about 4 mm^2 . In step widths of $30 \mu\text{m}$, a total number of 2544 single PALS spectra has been obtained within a total measurement time of 8 hours.

The resulting two-dimensional average positron lifetime map is shown in Fig. 1. The copper grid on top of the carbon tape is nicely resolved. The measurements yield a beam spot size of $D = (180 \pm 10) \mu\text{m}$ (FWHM).

This experiment paves the way for the final implementation of the SPM. We expect the SPM to become a world-wide unique instrument, considerably extending PALS measurements for materials sciences.

J. Mitteneder et al., Micrometer positron beam characterization at the scanning positron microscope interface; J. Phys. Conf. Ser., 791(1), 012006 (2017)

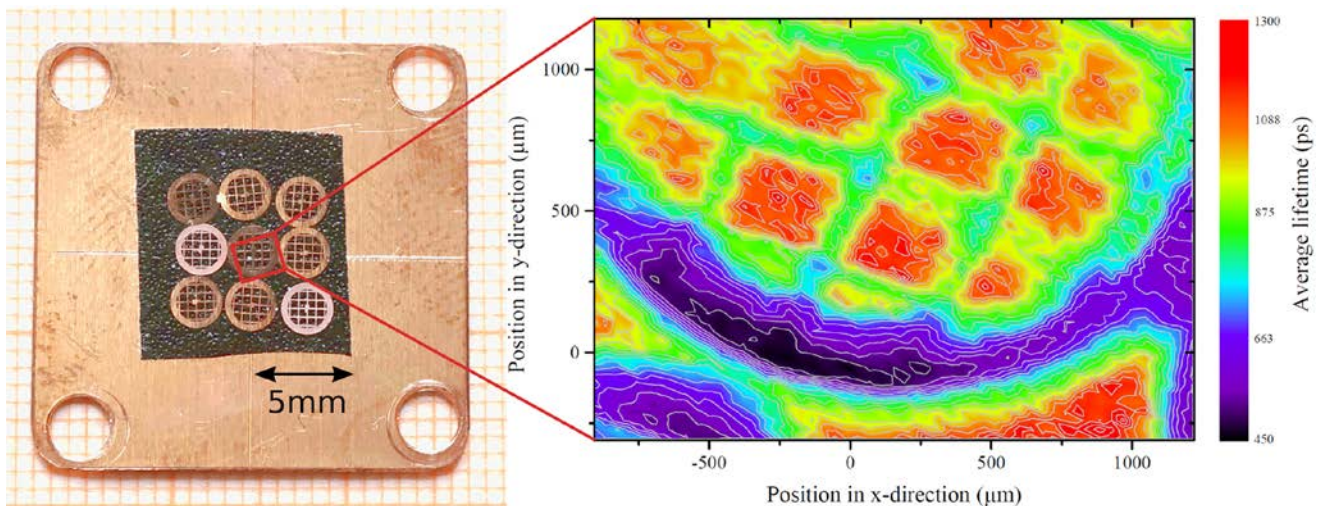
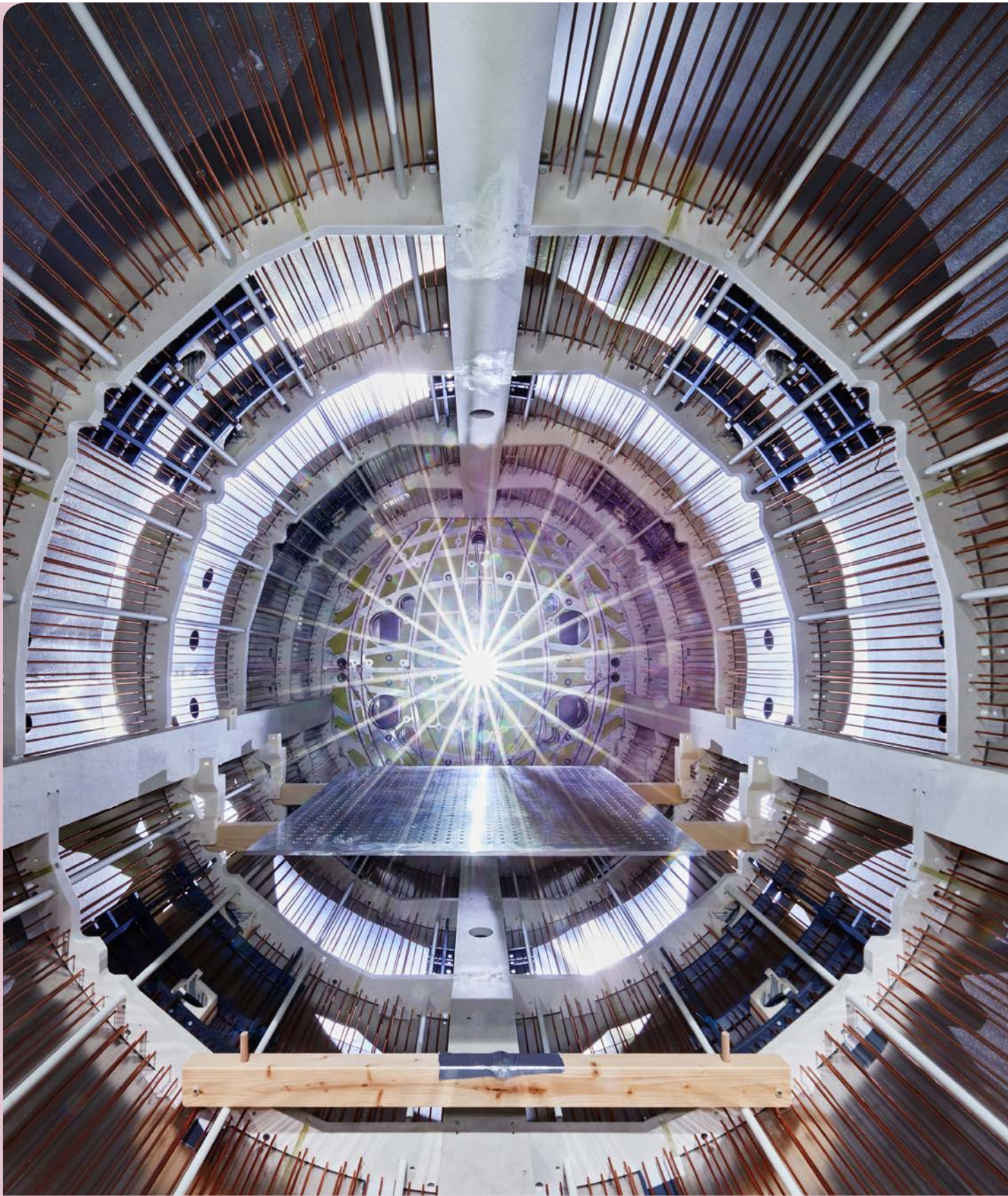


Figure 1: Photo of the test sample (copper grid on carbon tape) and average positron lifetime map obtained: The lifetime map shows 2544 pixels. Each pixel represents a positron annihilation lifetime spectrum. The average lifetime in the carbon tape (red) is much higher than in the copper (violet). A measurement time of 8 seconds per spectrum is sufficient to differentiate between the materials. The whole picture was obtained within 8 hours.

The experiment for the measurement of the neutron electric dipole moment in the new neutron guide hall east.



Instrumental Upgrades & Services

News from the instruments

C. Hugenschmidt¹, V. Hutanu^{2,3}, T. Keller⁴, P. Link¹, J.-F. Moulin⁵, A. Ostermann¹, Zsolt Revay¹, M. Schulz¹, E. Vezhlev², N. Walte⁶

¹Heinz Maier-Leibnitz Zentrum (MLZ), Technische Universität München, Garching, Germany; ²Jülich Centre for Neutron Science (JCNS) at MLZ, Forschungszentrum Jülich GmbH, Garching, Germany; ³Institute of Crystallography, RWTH Aachen at MLZ, Garching, Germany; ⁴Max-Planck-Institut für Festkörperforschung, Stuttgart, Germany; ⁵German Engineering Materials Science Centre (GEMS) at MLZ, Helmholtz-Zentrum Geesthacht GmbH, Garching, Germany; ⁶Bayerisches Geoinstitut, Universität Bayreuth at MLZ, Garching, Germany

A new detector system, an enhanced sample stage or even the integration of a new experimental method into an instrument, all these improvements are needed to provide excellent measurement conditions and open new possibilities for the users.

More experimental flexibility with a new setup at PGAA

The neutronic part of the instrument remained the same: a pneumatic system (now software controlled) interchanges between a collimator and a focusing neutron guide to switch between medium and high fluxes.

In addition to the earlier 60 % HPGe detector, a new low-energy germanium (LEGe) detector was installed. It only has a reasonable counting efficiency for low-energy gamma rays, although it has outstanding energy resolution. This detector will also be surrounded by a bismuth germanate (BGO) Compton suppressor annulus to lower the spectral base line. The new sample changer has doubled the throughput. It accommodates 16 aluminum frames in a carousel, and a pneumatic system lowers the sample into the irradiation position. The sample chamber can be evacuated, and also rotated, to allow for the best irradiation angle for the samples.

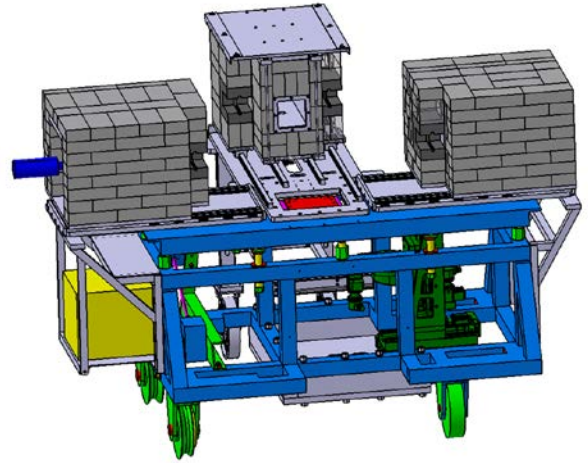


Figure 1: The design of the moveable shielding of the PGAA instrument

The two detector shieldings and the beam stop can be moved on a rail system (Fig 1). The new instrument can now be rapidly modified for different applications, such as standard prompt gamma activation analysis, gamma-gamma coincidence counting in nuclear physics measurements, neutron radiography, prompt gamma activation imaging, or neutron depth profiling.

The software control for the neutron irradiation and the gamma-ray counting has now been unified in a single program in a user-friendly way, and is compatible with the control system at the FRM II.

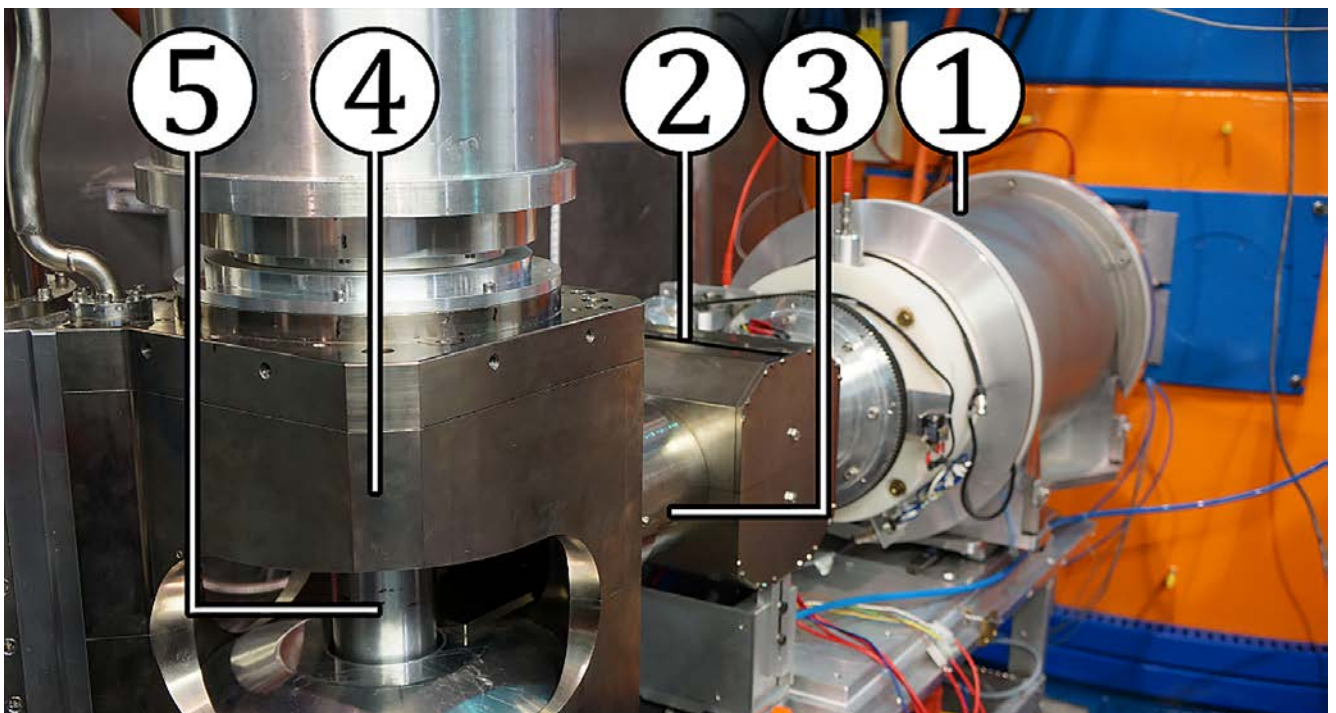


Figure 2: New setup for polarized neutron diffraction in magnetic field at POLI with 1) Polarizer, 2) Spin flipper, 3) Guide field, 4) HTS magnet and 5) Cryostat.

New Setup for polarized neutron diffraction in a magnetic field at POLI

The **P**olarisation Investigator (POLI), operated by RWTH Aachen in cooperation with JCNS at the MLZ, is dedicated to the investigation of the complex magnetic structures of single crystals and their behavior under varying external conditions such as temperature, pressure and magnetic or electric fields.

In addition to the available spherical neutron polarimetry in the zero field and non-polarised diffraction under extreme conditions, the instrument POLI was extended by the addition of a setup for polarized neutron diffraction in a magnetic field. It uses the new high T_c superconducting magnet with a maximum field of $B_{max} = 2.2 T$, manufactured by HTS 110 New Zealand.

Due to the large openings of the HTS magnet, giving a maximal 150° horizontal and 40° vertical access to the scattered beam, the setup can be operated in two different modes: It can either be used with a lifting counter for out-of-plane flipping ratio measurements, or with the Decpol for in-plane uniaxial polarization analysis. Moreover, the wide openings and large sample area allow a cryostat to be inserted for sample temperatures between 40 mK and 500 K, or the use of a pressure cell in the magnetic field.

The beam polarization and analysis is achieved by ^3He spin-filter cells (SFC). In general, the combination of high magnetic fields and ^3He SFCs is seen as difficult, since the stray fields of the magnet can depolarize the Helium gas in the cells. However, for the HTS magnet, the stray fields are rather low due to its iron yoke. Thus, the μ -metal shielding of the SFCs is sufficient to compensate for the stray field, and no polarization losses were observed.

Since the magnet was not originally planned for polarized neutron diffraction, it has symmetric field geometry and, thus, the stray field flips the field direction in the beam path very close to the surface of the yoke of the magnet. To avoid depolarization of the neutrons in this zero-field region, a dedicated guide field was developed to connect the field in the polarizer to the main field in the magnet without disturbing the neutron polarization. The guide consists of two main parts. The first is a Mezei flipper optimized for the hot neutrons, shielded from the stray field of the magnet by a thick iron box, and placed into a homogeneous guide field of around 30 G, produced by permanent magnets. This part is located directly after the polarizer (pos.2 in Fig. 2). The second is the connection between the flipper and HTS magnet. It consists of two iron poles that pass inside the magnet and guide its main field toward the flipper to suppress the zero point. These flat poles are shielded by an iron cylinder and mounted directly onto the magnet yoke (pos. 3 in Fig. 2).

The individual parts of the guide field and the flipper were optimized by finite element simulations using COMSOL Multiphysics® as part of the Bachelor's thesis of Henrik Thoma. The dependence of neutron polarization on the current in the flipping coil, as measured and calculated from the simulation model, is shown in Fig. 3.

In a first test measurement, a high polarization feed-through above 98.5 % over the complete field range of the HTS magnet was reliably obtained. The setup is ready for application, and has already been successfully used in 2016 for first user experiments.

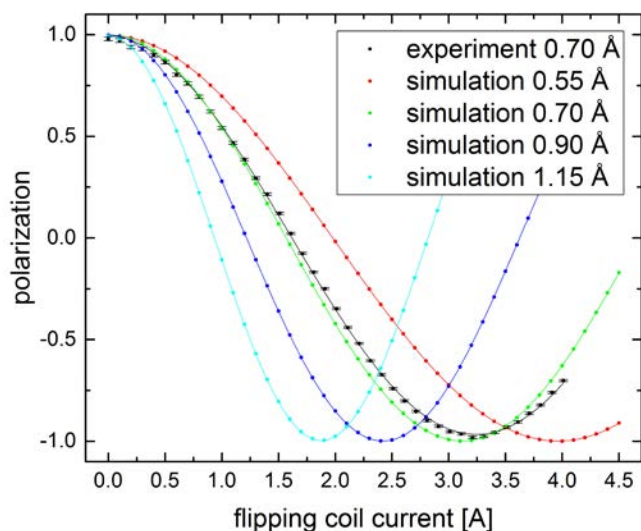


Figure 3: Simulated and measured polarization dependent on the current of the flipping coil for different wavelengths.

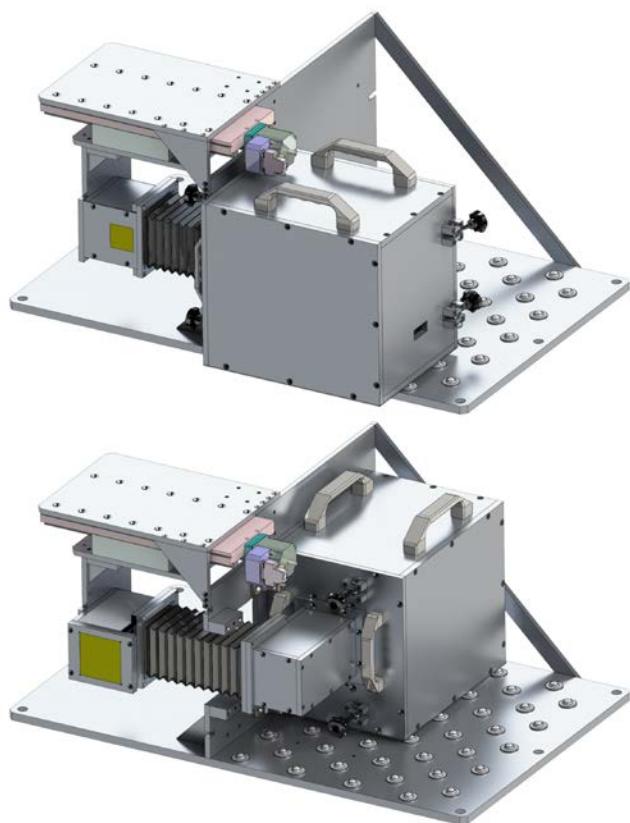


Figure 4: Technical drawing of the new high resolution detector at ANTARES in the one-mirror configuration for best resolution with 6.5 μm pixel size (top). When the camera is rotated by 90° a second mirror can be introduced into the optical path between scintillator and camera to improve the shielding of the detector and reduce the background (bottom).

The new high resolution imaging detector at ANTARES

Recently, a new versatile high resolution neutron imaging detector was installed at the ANTARES beam line at the MLZ. The detector is based on a thermoelectrically cooled scientific CMOS camera (Andor Neo 5.5 with 2560x2160 pixels) which records the optical image of the neutron beam intensity produced on a thin film $\text{Gd}_2\text{O}_2\text{S}$ (Gadox) scintillator of 10 μm thickness. The optical path between the detector and the scintillator is covered by a bellow system and allows for a quick and flexible adjustment of the field of view (FOV) from 14 mm to 64 mm. While in the high resolution mode with a 14 mm FOV and a pixel size of 6.5 μm (Fig. 4 top) only one mirror is used in the optical path, all modes with a FOV larger than 28 mm (Fig. 4 bottom) are realized with two mirrors. This helps to improve the shielding of the detector by avoiding direct sight between the CMOS chip to any parts which are in the beam and might produce gamma radiation. In order to switch between these modes, the box with 5 cm Pb shielding which contains the camera can be rotated by 90°. Additionally, the detector provides an autofocus system to achieve the highest possible resolution.

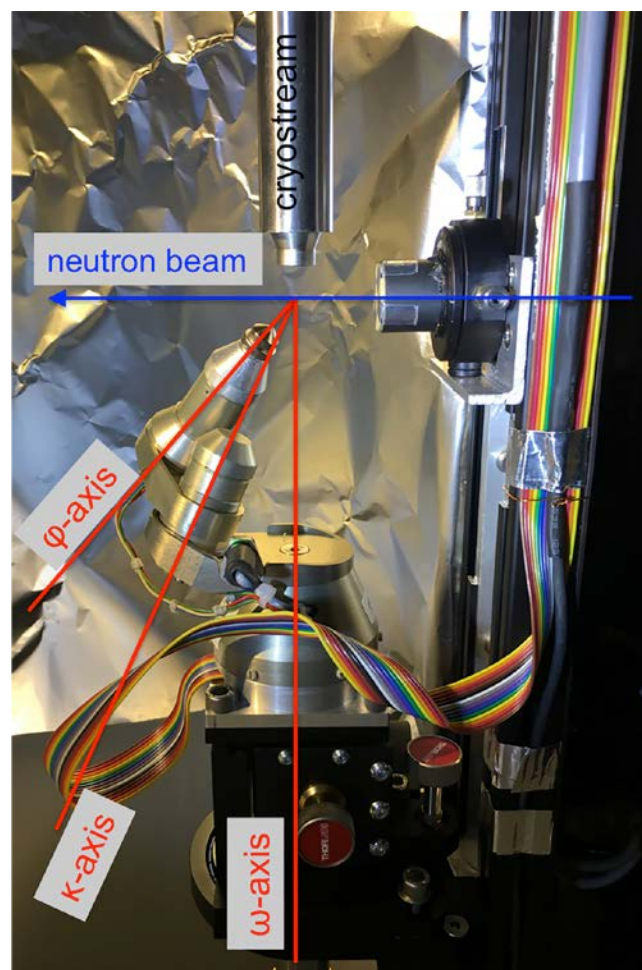


Figure 5: New mini- κ -goniometer at BIODIFF in combination with the N_2 -cryostream set-up.

New mini- κ -goniometer at BIODIFF

Quite recently, a new optional mini- κ -goniometer (MK3, ARINAX, France) was installed at the instrument BIODIFF. This motor driven mini- κ -goniometer consists of a ϕ -axis sitting on a κ -arm. The mini- κ -goniometer is mounted on the ω -axis of the diffractometer with an angle of 24° between the κ - and ω -axis (see Fig. 5). The κ -axis range lies between -10° and 240° with a maximum tilt angle of 48° at a κ -angle of 180°. The new mini- κ -goniometer can be used for room temperature data collection as well as with the N_2 -cryostream set-up of BIODIFF. In combination with the N_2 -cryostream set-up in particular, it allows for the automatic reorientation of the crystal with respect to the neutron beam without the necessity to manually remount the crystals with special cryo-tools. In combination with a new strategy software, the mini- κ -goniometer makes it possible to optimize the data collection, leading to shorter measurement times and an increased data set completeness.

A new polarizing guide for TRISP

After more than ten years of operation, the polarizing neutron guide section of TRISP was dismantled to allow the beam shutter SR5 to be exchanged. This ten meter long polarizing bender was severely activated and could therefore not be reused, although its performance was still good. TRISP was then temporarily installed at its previous position in the experimental hall and returned to full user operation in November 2016. In due course, TRISP will move to the new experimental hall east. To avoid additional costs and activated parts, the new polarizer has to work efficiently in the current provisional position with 10 m spacing between the reactor and monochromator, and in the final location with the 35 m guide length, where parabolic guides have to be used to avoid excessive transmission losses.

The polarizer has now been designed as a cavity type $m = 1.5/5$ of 3.5 m length, with two parallel channels, each with a cross section of $47 \times 97 \text{ mm}^2$ (Swiss Neutronics). In the provisional short version, only one channel of this cavity is used in combination with a straight neutron guide which was produced by the FRM II neutron optics group. For the final long setup, the cavity will be placed in between two parabolic elements. The first diverging parabola ($L = 15 \text{ m}$) reduces the horizontal beam divergence and increases the beam width to 89 mm, followed by the cavity and a converging parabola. This system will show good transmission and beam polarization for the thermal wavelength band 1-4 Å, the maximum polarized monochromatic flux at the sample being around $5 \cdot 10^7 \text{ n/cm}^2 \text{ s}$.

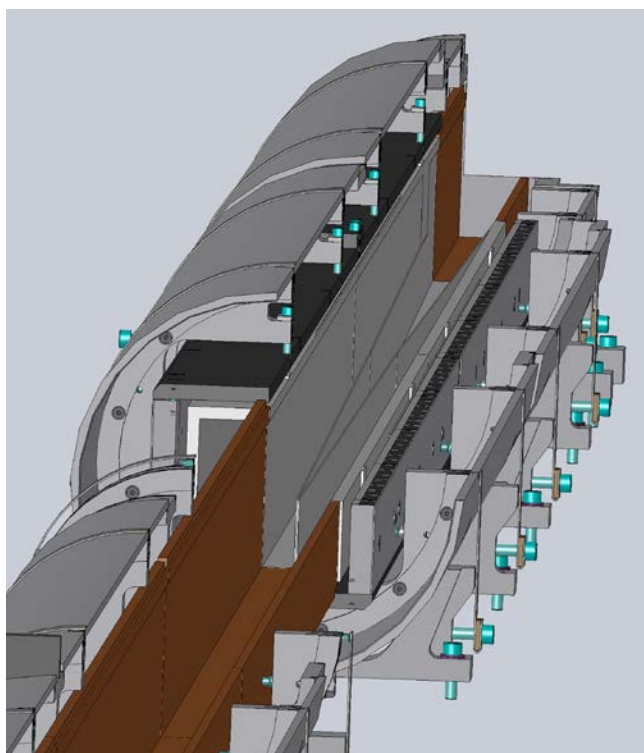


Figure 6: Sketch of the TRISP polarizer (cut). The polarizer has two channels with V-shaped silicon wafers coated with FeSi polarizing supermirrors ($m=5$). The lower critical wavelength is close to 1Å. Permanent magnets supply a vertical field of 0.5 mT. The vacuum system uses a new design based on precise aluminum tubes, which are usually used for pneumatic cylinders.

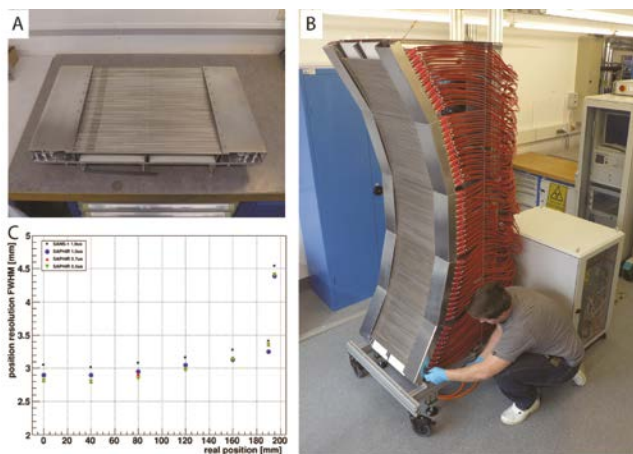


Figure 7: Helium-3 detector system of SAPHiR. (a) Detector segment with 48 position sensitive detectors (PSD). (b) Completed 90° detector bank with five detector segments and a total of 224 PSD. The MPD read-out electronics and the high-voltage modules are positioned behind the PSD. The media supply and the higher-level MCPD modules are integrated in the control cabinet. (c) Measurements of the position resolution reveal a position resolution of 3 mm.

Upgrade of SAPHiR in the neutron guide hall east

In 2016, the final assemblage and testing of the two 90° ^3He detector banks was completed by the FRM II detector group (Fig. 7). The SAPHiR detector system is now almost completed, consisting of four wave-length-shifting-fibre detector segments at the back-scattering region for superior position sensitivity and the helium-3 detector system at 90° to the primary beam (Fig. 8). An external clock synchronises the two detector systems and allows integration of the data. The forward scattering detector bank is currently under construction.

In order to lower the measurement background due to the sample environment, radial collimators were installed between the sample and the back-scattering detectors and the 90° detector banks (Fig. 9). The collimators, supplied by JJ x-ray, have a gauge length of 3 mm to account for the standard SAPHiR sample size; an additional set of collimators with a gauge length of only 1.5 mm was purchased for the 90° detectors to be used for smaller samples used in experiments at higher pressures. The collimators are attached to collimator frames with linear and rotational tables for high-precision adjustment relative to the sample position. A second prototype for the gas chambers to minimize background due to scattering in air between the sample and the main detector banks was built and successfully tested.

A blowout protection was added to the primary anvils, forming an electrically insulated enclosure around the sample environment when the press is closed (Fig. 9). This enclosure prevents the escape of potentially activated material during explosive gasket failure (blowouts) or anvil breaks. Off-line experiments were conducted to develop new anvil geometries that allow the maximum achievable sample pressure to be increased to $> 20 \text{ GPa}$. The SAPHiR instrument is funded by the BMBF, project number 05K16WCA.

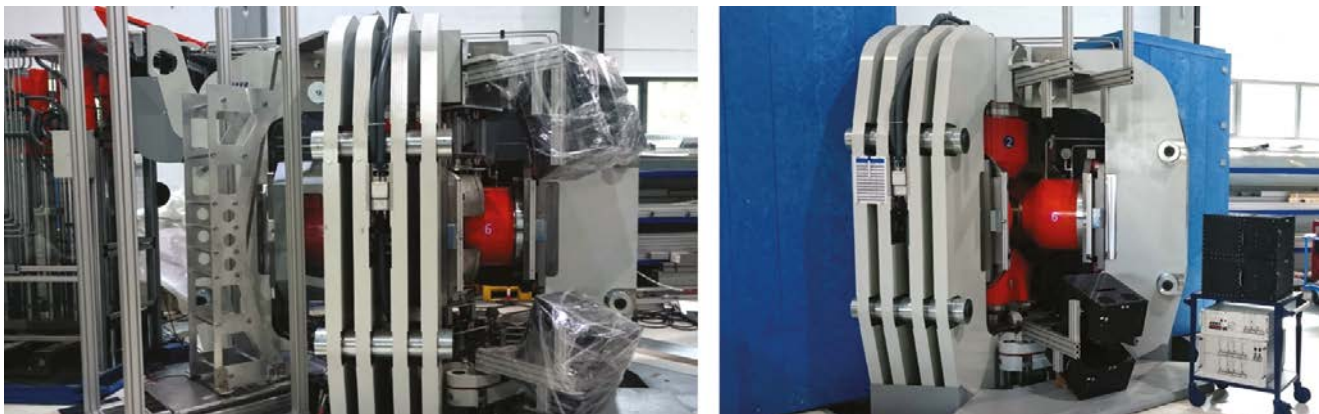


Figure 8: SAPHIR with and without detector shielding (10 cm boron-PE), the 90° detector frame, and the WLSF detector segments (black boxes). The neutron guide will enter the instrument from the right side between the WLSF detectors.

New developments at NEPOMUC

The high-intensity positron beam provided by NEPOMUC is usually extracted at a kinetic energy of 1 keV. In a subsequent section, the brightness of the beam is enhanced by using a so-called remoderation device which basically consists of a tungsten single crystal for stochastic positron cooling. By biasing the tungsten crystal, the energy of the remoderated positron beam is set to 20 eV for most of the experiments.

Using the beam monitors of the NEPOMUC beam line and a retarding field technique, the beam parameters have been changed in order to extract the remoderated positron beam at different energies in a much wider range between 5 and 400 eV. In addition, new settings of the primary beam have been found to produce a low-energy primary positron beam of only 5 eV. Despite the lower phase space density compared to the remoderated beam, such a low energy at an intensity that is still high is estimated to be beneficial i.e. for accumulating a larger number of positrons in a dipole trap for fundamental studies. However, due to transport losses to the multi-purpose open beam port (OP), further improvement to the beam parameters is envisaged for upcoming beam times.

A special device has been set up at the open beam port (OP) for the analysis of the phase space of the positron beam. Hence, we were able to determine the beam properties for the primary and the remoderated positron beams at various energies in order to adjust the injection parameters for the magnetic dipole trap. In a second step the trap, basically comprising a permanent neodymium magnet (0.6 T at its surface) in the center of a vacuum chamber, was installed at the OP. Both the primary and the remoderated positron beams were transported at 5 eV into the confinement region of the dipole field trap using the ExB drift motion between a pair of deflection plates. Compared to previous beam times, the injection efficiency could be increased from 38 % to about 100 %. The lifetime of the positrons trapped in the dipole field was determined to 15 ms. Continuing a collaborative research project (Max Planck Institute for Plasma Physics, Greifswald and Garching, University of Tokyo, Universität Greifswald, Lawrence University, Appleton, USA, and TUM) it is envisaged to create the first positron-electron pair plasma on earth for the first time.



Figure 9: Radial collimators for the 90° detector banks (left) and the backscatter detectors (right). The middle shows the sample position with the primary anvils and the blowout protection.

The Coincidence Doppler Broadening Spectrometer (CDBS) was upgraded with a beam brightness enhancement system in order to facilitate CDB spectroscopy with higher spatial resolution (supported by the BMBF, project no. 05K13WO1). The positron guiding system is realized by a newly designed μ -metal column, optically shielded and comprising several electrostatic lenses and magnetic compensation coils. First, the positron beam is focused onto a 100 nm thin single crystalline Ni(100) remoderation foil before it is accelerated to up to 25 keV onto the sample. A new piezo controlled positioning device allows for spatially resolved defect spectroscopy by scanning the positron beam diameter in an area of 19 x 19 mm. With this setup a positron beam diameter of 50 μ m (FWHM) at the sample position was achieved. The whole experimental setup of the CDBS with two pairs of high purity germanium detectors is shown in Fig. 10.

For temperature dependent measurements with low energy positrons, a heatable sample holder was put into operation at the surface spectrometer. With this new device, positron annihilation induced Auger-electron spectra could be recorded in order to facilitate studies of the surface kinetics up to 1300 K. Hence, surface processes such as surface segregation could be observed as a function of temperature in situ. In addition, depth resolved positron measurements by variation

of the implantation energy have become feasible by increasing the total energy of the beam using a so-called beam elevator (supported by the BMBF, project no. 05K13WO1). The device was further optimized, yielding an overall pulse width of typically 1.66 ns pulses at a repetition rate of 5 MHz. Using an energy elevation of up to 3.5 keV, the transmission efficiency turned out to be about 88 % compared to the intensity of the continuous positron beam. First, energy dependent positron reemission spectra were recorded in order to study the remoderation properties of single crystals of Pd and W.

The interface at the Scanning-Positron-Microscope (SPM, developed at the Universität der Bundeswehr) was further improved in order to adapt the energy of the positron beam delivered from NEPMUC to the W remoderator inside the SPM. To this end, it was demonstrated that the total beam energy can be raised by 1.2 keV by using an energy elevator. In contrast to the beam elevator at the surface spectrometer, the setup of the SPM interface is operated without magnetic guiding fields. To characterize the beam and first positron lifetime measurements, a new sample chamber has been connected to the exit of this SPM-interface. Within first measurements, a pulse width of about 250 ps and a beam diameter of less than 200 μ m were achieved. For details of the present status, see the scientific report on page 44.



Figure 10: Upgrade of the CDB-spectrometer at NEPMUC with the new optical column and an additional remoderation unit for brightness enhancement. Four high purity germanium detectors pointing to the sample center are used to measure the Doppler-broadening of the positron-electron annihilation line.

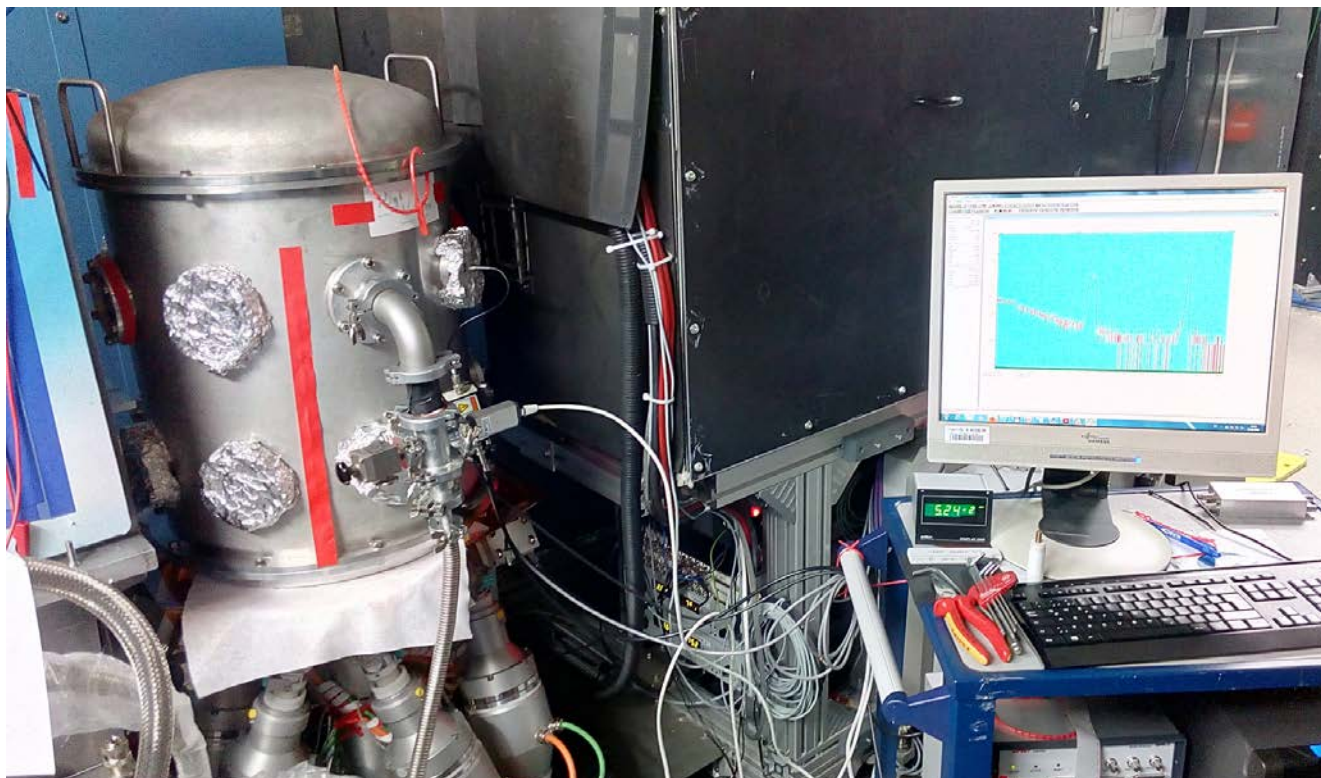


Figure 11: Neutron Depth Profiling spectrometer during test measurements at the reflectometer MARIA.

Neutron depth profiling spectrometer at the beam of MARIA: first measurements

Over the last year, a new Neutron Depth Profiling (NDP) spectrometer has been set up to be used at the focused neutron beam of the reflectometer MARIA at the MLZ (see Fig. 11). The primary aim of the new spectrometer is to explore for the first time Li migration in thin-film batteries in operando on a less than a minute rate with 10 nm depth resolution.

The NDP spectrometer is installed on the sample table of MARIA (neutron guide NL5-N) and the sample, placed in the NDP vacuum chamber, is illuminated by the high-intensity focused cold neutron beam shaped by the collimating slits of MARIA. The charged particles, e.g α -particles emitted from the sample after ${}^6\text{Li}(n,\alpha){}^3\text{H}$ reaction, are detected by a high resolution planar silicon detector(s). The detected energy spectra give information about the depth distribution of the emitting isotopes. The interior of the vacuum chamber is

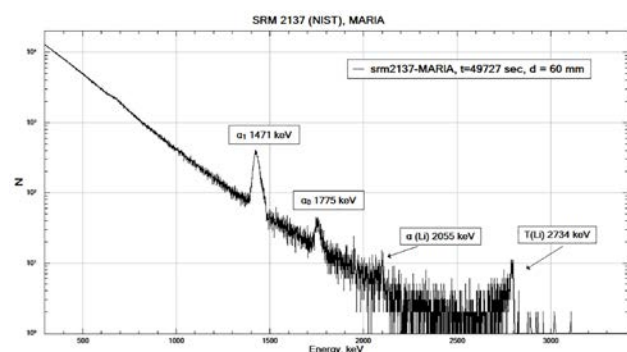


Figure 12. NDP spectra of NIST standard reference material 2137 (Boron implanted into silicon wafer) collected at MARIA in roughly 14h.

constructed in such a way as to minimize any gamma and fast electron background that could appear while an intense neutron beam is penetrating through the chamber. Extensive attempts to reduce the background have been carried out over the last year and have resulted in the suppression of an unwanted signal (coming mainly from gamma rays of different energies) by more than two orders of magnitude.

In Fig. 12, the spectrum collected from a standard NDP sample SRM 2137 (produced in NIST, USA) is shown. The sample consists of natural boron implanted into a silicon wafer with the certified depth profile of the boron distribution in silicon. Such samples are routinely used at NDP facilities around the world for calibration measurements. The results of our measurements are in good agreement with the certified values. Moreover, thanks to an extremely high flux at MARIA and good signal-to-noise ratio at the NDP detecting system, a few additional peaks are observed.

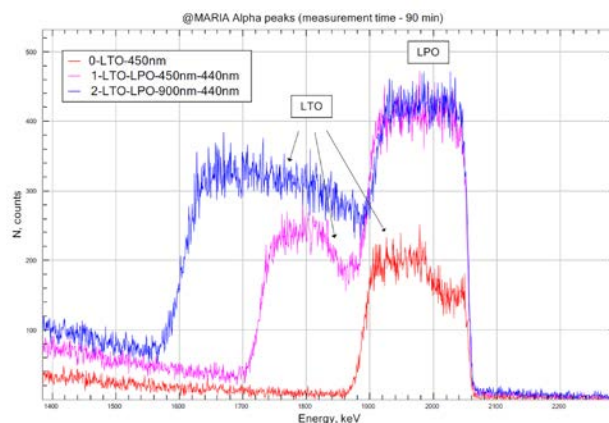


Figure 13: Alpha-peaks from thin-film LTO cathode and LTO cathode plus LPO electrolyte

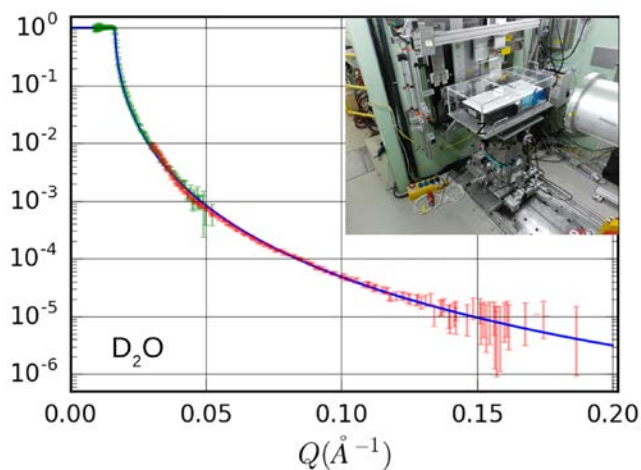


Figure 14: A D_2O reflectivity curve as measured at REFSANS. The inset shows the Langmuir trough on its antivibration table.

As a next step, NDP measurements were carried out with thin-film battery type samples prepared by the group of Prof. P. Notten (TU Eindhoven & Forschungszentrum Jülich). The alpha-peak regions of the NDP spectra of the as-deposited $Li_4Ti_5O_{12}$ (LTO)/ Li_3PO_4 (LPO) dual-layers with different thicknesses are shown in Fig. 13. It is clearly visible that the details of the interfaces can apparently be followed due to the variation of Li-ions concentration in the layers. Moreover, the counting rates achieved at MARIA paved the way for fast measurements at a less than 30 seconds rate.

User experiments with in operando studies of full battery stacks are already scheduled for forthcoming reactor cycles. Also planned for next year is the full implementation of the NDP spectrometer into reflectometer MARIA and reflectometer TREFF (as a test beamline), including operation under the standard MLZ NICOS software. The NDP spectrometer is open for user experiments through the MLZ proposal system.

Upgrades at REFSANS, the horizontal TOF reflectometer

The frame overlap slave chopper has received new disks with two 120deg symmetric windows. Thanks to these, it is now possible to achieve a larger duty cycle and better exploit the continuous neutron flux while keeping the chopper rotation speed low (<4000 rpm). Intensity gains with respect to the previous setup are up to a factor two depending on the wavelength band and desired resolution.

A new detector (DENEX multiwire 3He chamber 680 mm x 500 mm) increasing the available width by 36 %, offering a high detection efficiency at low wavelengths and a small pixel size (2.5 mm x 2.2 mm) has been installed. The increased width facilitates faster and more complete measurements of GISANS patterns. In the case of reflectometry measurements, this makes it possible to accept the full available horizontal divergence (a gain of about 30 % intensity).

On the sample environment front, the large Langmuir trough normally operated at REFSANS has been modified to accommodate a smaller tank, more convenient for studies where only a small amount of material is available.

Support for MLZ from Jülich: engineering and electronics

Romuald Hanslik¹, Hans Kämmerling¹, Daniel Durini², Carsten Degenhardt², and Rainer Bruchhaus³

¹Central Institute for Engineering, Electronics and Analytics, Engineering and Technology (ZEA-1), Forschungszentrum Jülich GmbH, Jülich, Germany; ²Central Institute for Engineering, Electronics and Analytics, Electronic Systems (ZEA-2), Forschungszentrum Jülich GmbH, Jülich, Germany; ³Jülich Centre for Neutron Science at MLZ, Forschungszentrum Jülich GmbH, Garching, Germany

Experts from the Central Institute for Engineering, Electronics and Analytics (ZEA) based at the Forschungszentrum Jülich provide considerable manpower and expertise to support and drive neutron scattering instrument improvement and operation at the MLZ. In 2016, the key project was the construction, manufacture and installation of the completely renovated very small angle scattering diffractometer KWS-3. Most of the work on the thermal time-of-flight spectrometer with polarization analysis TOPAS was carried out within the impressive vacuum chamber installed in the neutron guide hall in 2015. The detector benches, as well as the rail system for the benches, were mounted within the chamber. The high-intensity time-of-flight neutron diffractometer POWTEX successfully underwent the transition from the drawing board of the design engineers and structural designers into manufactured masterpieces of shaped materials and metal. In order to improve on the neutron count rates currently achievable, gain greater mechanical flexibility, operate in magnetic fields of up to several Tesla, and increase the detector space resolution in small angle neutron scattering (SANS) instruments such as KWS-1 or KWS-3 of the MLZ, a new generation of pixelated scintillator detectors could be the new way to proceed. An interesting candidate for the photodetector element in these neutron detectors could be an array of silicon photomultipliers (SiPM), either analog or digital. The main risk identified so far is their radiation hardness, considering thermal or cold neutron irradiation. Thus, in 2016 the radiation hardness of three different SiPM technologies (two analog and one digital) was fully investigated in terms of their dark signal, breakdown voltage, and photon detection efficiency performances under irradiation with cold neutrons.

A considerable workforce to support and drive neutron scattering instrument improvement and operation at the MLZ is located at the Forschungszentrum Jülich in Jülich. The Central Institute for Engineering, Electronics and Analytics, Engineering and Technology (ZEA-1) includes groups of expert engineers engaged in design and construction. In addition, it operates workshops in which parts ranging from tiny μ -sized up to heavy weights of several tons can be precisely machined, handled and assembled. The Central Institute for



Figure 1: High-precision work with the crane was needed to get the new KWS-3 instrument frame into place.

Engineering, Electronics and Analytics, Electronic Systems (ZEA-2) is active in preparing customized detector solutions for the neutron scattering instrument suite at the MLZ. These groups of skillful experts and the large scale infrastructure are key players in enhancing the performance of the neutron scattering instrument to meet the requirements that arise out of the challenges in the various scientific fields.

Renewing KWS-3

KWS-3 is the very small angle scattering diffractometer at the MLZ. It runs on the focusing mirror principle. The central piece of this instrument is the double-focusing toroidal mirror installed in a vacuum chamber. In recent years, the demands of the scientific users have continuously increased. However, it turned out that the existing framework was not stable enough to meet the requirements of the scientists. It was therefore decided to renew the instrument completely. Construction of the new instrument proved to be a real challenge. The floor space available for the instrument in the guide hall between the neutron guides of the small angle neutron diffractometer KWS-2 and the reflectometer REFSANS is very limited (Figs. 1 and 2). However, the engineers from ZEA-1 and JCNS succeeded in building a heavy

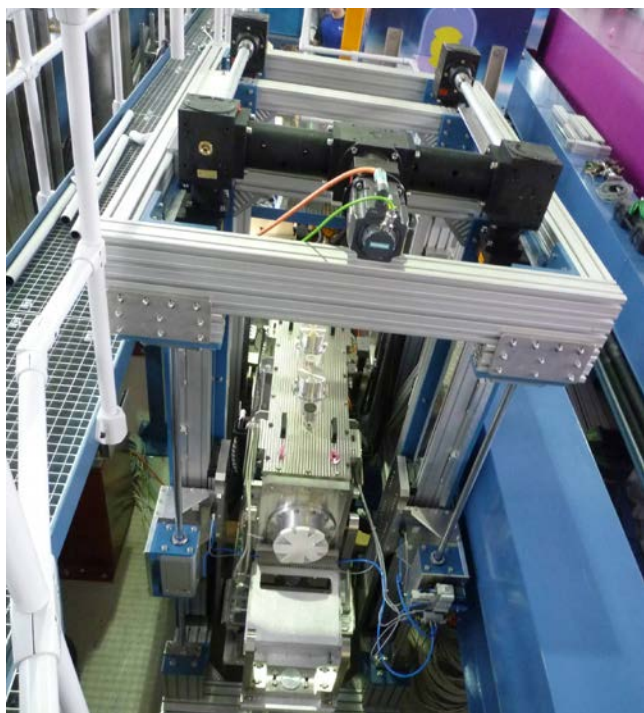


Figure 2: The frame fits exactly between the guides of the adjacent instruments KWS-2 (right) and REFSANS (left).

weight frame of remarkable mechanical stiffness within this limited space. The focusing system was redesigned and mechanically separated from the sample area and the section carrying the detector in order to improve the stability of the focusing system, precision of the mirror positioning system and instrument resolution. The integration of two motorized 4-blade slit systems in front of and behind the mirror and an additional “cleaning” blade below the mirror is intended to improve the signal-to-noise ratio of the instrument. The new design of the mechanical system suppresses the influence of the evacuation steps on the mechanical parts (Fig. 3). Extensive testing over several weeks at the ZEA-1 workshop in Jülich confirmed the reliable operation of the setup before it was transported to JCMS in Garching (Fig. 4).

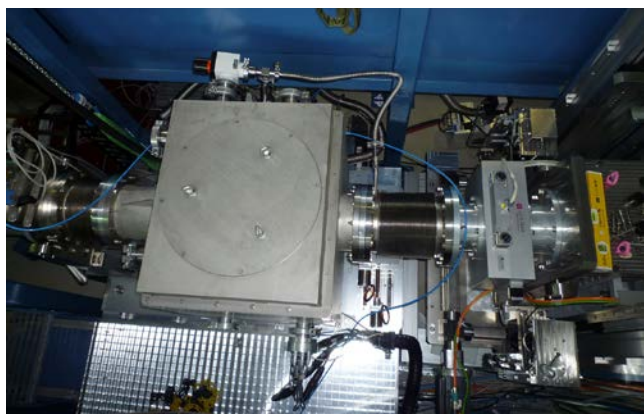


Figure 3: The sample chamber on top of the automatically controlled sample table for loads up to 1000 kg is carefully decoupled mechanically from adjacent instrument components.

A specially designed, automatically controlled, sample table can carry high loads of up to 1000 kg, offering the option of performing experiments with really heavy sample environment equipment such as high-field magnets. More options with respect to mirror chamber movements and sample positioning offer a new flexibility for the experimentalists to



Figure 4: Setup for intensive tests of the instrument functions in the ZEA-1 workshop prior to transportation to JCMS in Garching.

maximise the performance of the instrument. The instrument control software was also renewed. Due to the well-coordinated and timely installation in the guide hall at the MLZ, commissioning of the new KWS-3 was able to begin immediately after the reactor start-up in August 2016. Meanwhile, the instrument is back to routine user operation and the first feedback from the scientists suggests that the rebuild of the instrument will turn out to become a resounding success.

A detector for TOPAS

Following the successful installation of the vacuum chamber of the time-of-flight spectrometer TOPAS in 2015, work in 2016 focused on the interior of the chamber. Key elements of the instrument are 288 high-performance ^3He detector tubes for space resolved neutron detection over a wide angle. Fig. 5 shows a detector box with sixteen ^3He tubes in the workshop prior to testing. To facilitate later maintenance and easy tube exchange, specially designed detector benches and boxes and a rail-system were constructed and manufactured in the Jülich workshops. Meanwhile, these benches and the rail system were mounted inside the chamber (Fig. 6). Another key component of TOPAS is the chopper cascade with the neutron analyser and the magnetic guide field. Fig. 7 shows the assembly in the workshop. In addition, the neutron beam polarization unit was built and successfully tested at the MLZ.



Figure 5: A detector box with sixteen ^3He tubes in the workshop being prepared for testing.

Chopper assembled for POWTEX

The high-intensity time-of-flight neutron diffractometer POWTEX successfully underwent the transition from the drawing board of the design engineers and structural designers into manufactured masterpieces of shaped materials and metal. The first sections, including the wing-shaped doors to open the sample chamber, have been finished and the next steps include the assembly of the parts and mounting of the drives for the tests. POWTEX has a sophisticated neutron pulse shaping system. This includes the double-disc pulse chopper, the overlap chopper and the bandwidth chopper. These choppers were assembled and tested over the course of 2016.

Radiation tests of new SANS detector system

It was recently proposed that a new generation of modular pixelated solid-state scintillator detectors be used in the small angle neutron scattering instruments of the MLZ. These detectors consist of a 1 mm thick Ce-doped ^6Li -glass scintillator covering a pixelated Silicon Photomultiplier (SiPM) based photodetector array. In 2016, the radiation hardness of three different (two analog and one digital) SiPM technologies was investigated in terms of their lifetime if used for this type of application. The figures of interest considered in this study were their dark signals, the breakdown voltages, and photon detection efficiency (PDE) performances under irradiation with cold neutrons. The characterization was carried out at the KWS-1 instrument at the MLZ.



Figure 6: Mounting of the detector benches inside the vacuum chamber of TOPAS.



Figure 7: Assembly of the chopper cascade and the neutron analyser in the workshop.

In order to make an assessment of the overall dose expected in one year of constant operation by the neutron detector of the KWS-1 instrument, the total number of neutrons detected by its current detector in the period between August 2014 and October 2015 has been presented in Fig. 8. The period considered comprises 4 measurement cycles, each consisting of 60 days (and 22 hours a day) as well as all kinds of different neutron scattering experiments. The color scale in Fig. 8 shows the number of neutrons detected per square centimeter. The current photomultiplier tube (PMT) based solid-state scintillation detector using the Anger camera principle has an active area of $60 \cdot 60 \text{ cm}^2$, and consists of 64 PMTs. The total number of cold neutrons (with wavelengths between 4.5 \AA and 12 \AA) detected during the period in question was of the order $9.12 \cdot 10^{10}$. All the measurements were made using the 3.3 cm^2 source aperture. For an upper limit estimation, a source aperture of 5.5 cm^2 and collimation distances shorter than those used in 39% of the experiments performed are considered instead, as this is what is planned to be used for the future “full-power” detector, and the equivalent dose detected, shown in Fig. 8, was scaled up by a factor of 14.2. As can be observed in Fig. 8, the vast majority of scattered neutrons tend to hit the detector in the immediate “high neutron flux” area surrounding the beam-stop, where an equivalent neutron dose of $3.2 \cdot 10^9 \text{ n/cm}^2$ was detected in the relevant period, whereas the rest of the detector detected an equivalent of $2.9 \cdot 10^8 \text{ n/cm}^2$ in total. The area of approximately 1 cm^2 within this region that detected the maximum number of neutrons received an equivalent dose of $7.4 \cdot 10^9 \text{ n/cm}^2$. Thus, we might conclude that the maximum one-year-equivalent dose of cold neutrons impinging on the detector is of order $7.4 \cdot 10^9 \text{ n/cm}^2$, whilst for a 10 year life-time, the neutron dose received will not exceed $7.4 \cdot 10^{10} \text{ n/cm}^2$. Nevertheless, the number of impinging cold neutrons undergoing nuclear reactions in the 1 mm thick ^6Li -glass scintillator is approximately 90 %. This means that the actual maximum neutron dose expected to reach the SiPM photodetectors underlying the scintillator glass are respectively $8.2 \cdot 10^8 \text{ n/cm}^2$ in one year of constant operation, and $8.2 \cdot 10^9 \text{ n/cm}^2$ over a 10-year period.

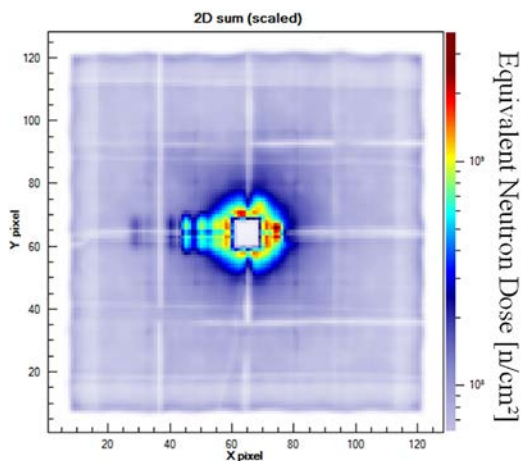


Figure 8: Number of cold neutrons detected over 240 days during all kinds of different neutron scattering experiments by the PMT based scintillation detector installed at the KWS-1 instrument of the MLZ in Garching. The “beam-stop” can easily be seen in the middle of the graph in the form of a white rectangle.

The three different SiPM technologies were irradiated with cold neutrons ($\lambda = 5 \text{ \AA}$) up to a dose of $6 \cdot 10^{12} \text{ n/cm}^2$. Fig 9 shows photographs of the three SiPM arrays mounted on breakout boards and covered by a boron-carbide mask used to define the irradiation region, and simultaneously enabling non-irradiated SiPM detectors to be used for monitoring purposes. The breakdown voltages of SensL (ArrayC-30035-144P-PCB) SiPMs and Hamamatsu (S12642-0808PB-50) MPPCs decreased by about 1 % for a $2 \cdot 10^{12} \text{ n/cm}^2$ cold neutron dose. Similar results were obtained for the Philips Digital Photon Counting DPC-3200-22-44 module also under study, which was irradiated up to a dose of $1.9 \cdot 10^{12} \text{ n/cm}^2$. For the maximum neutron dose to be received by the area of maximum neutron impact of a scintillation neutron detector in one year, the increase in the dark signals was between 20 % and 40 % for all 3 SiPM technologies under study. The increase for a ten-year equivalent neutron dose was between 40 % in the case of Hamamatsu MPPCs and a factor 6.8 for the Philips DPC-3200-22-44 module. However, this will not lead to a significant decrease in neutron detection efficiency or neutron-gamma discrimination. Finally, the photon detection

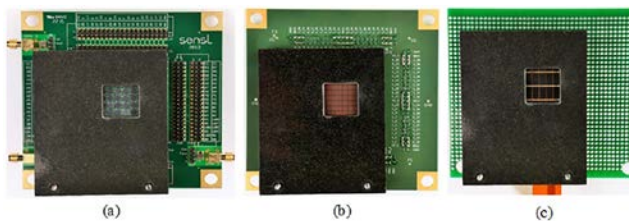


Figure 9: Photographs of the 3 SiPM technologies under investigation, covered by a 6 mm thick boron-carbide plate: (a) SensL 12x12 detector array ArrayC-30035-144P-PCB mounted on a breakout board MicroFB-30035-SMT; (b) Hamamatsu 8x8 MPPC array S12642-0808PB-50 mounted on a break-out board designed for this experiment; (c) Philips DPC3200-22-44 module.

efficiency of the Philips DPC module, monochromatically measured for the wavelength range between 300 nm (ultra-violet) and $1.1 \mu\text{m}$ (near infrared) in 10 nm steps, showed no significant change after irradiation with $1.9 \cdot 10^{12} \text{ n/cm}^2$, and the same result is expected to be obtained in further characterization of the two analog SiPM technologies. The PDE measurements were performed using a customized measurement system, used at the ZEA-2 and depicted in Fig. 10. It consists of a xenon (Xe) short-arc lamp, a monochromator, a certified reference photodiode read out using the lock-in measurement principle, an automatized x, y, z, and ϕ positioning system, and a double stage Peltier element cooling system.

In conclusion, we can state that all three technologies constitute viable sensors for their use in Small-Angle Neutron Scattering detectors in which typical doses of 10^{10} n/cm^2 over ten years of constant operation are expected. Future work in this direction consists of a thorough characterization of a SiPM based solid-state scintillator detector demonstrator in terms of its neutron detection efficiency, spatial resolution, achievable neutron count-rates, neutron-gamma discrimination, and radiation hardness.

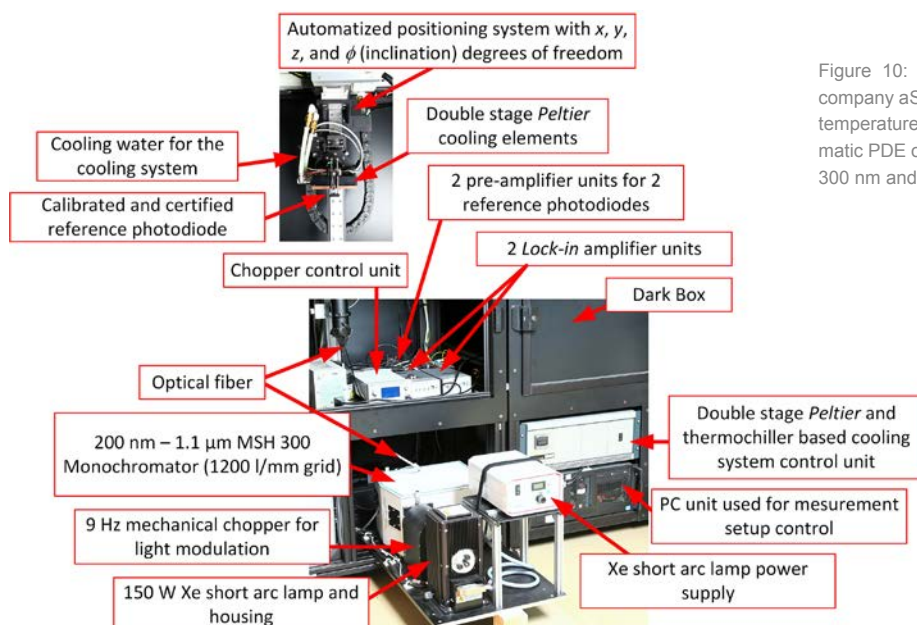


Figure 10: Measurement system custom-developed by the company aSpect Systems GmbH and located at the ZEA-2, for temperature and position sensitive measurement of monochromatic PDE of photodetectors in the wavelength range between 300 nm and $1.1 \mu\text{m}$.

When the instruments operate smoothly ...

R. Bruchhaus¹, J. Krüger², A. Kriele³, P. Link², H. Reithmeier², H. Wenninger², J. Wuttke¹, K. Zeitelhack²

¹Jülich Centre for Neutron Science (JCNS) at MLZ, Forschungszentrum Jülich GmbH, Garching, Germany; ²Physik-Department E13, Technische Universität München, Garching, Germany
³German Engineering Materials Science Centre (GEMS) at MLZ, Helmholtz-Zentrum Geesthacht GmbH, Garching, Germany

The service groups have done a great job. In this context, “nothing to report” is in many cases the best news at all. Nevertheless, in addition to routine operation, the service groups and laboratory facilities work continuously to improve and refurbish the instruments and installations in order to keep up with the best neutron instrumentation world-wide.

Accuracy and care: neutron optics group at work

A major task of the last 4 years, the refurbishment program of the neutron guide system in the Neutron Guide Hall West, has been completed with a final great effort. From the neutron guide NL5 down to the instruments MARIA (NL5-N) and TREFF/ RESEDA (NL5-S), a total of 50 m of neutron guide elements have been replaced by new ones produced by Mirrotron and based on N-BK7 Boron containing crown glass substrate with enhanced thickness to grant long term stability under vacuum. Finally, 16 m of the guide NL1, also with enhanced substrate thickness and 12 m of neutron guide NL2a-o, were produced in house. Their installation completed this long-term project. Besides that, several smaller projects have been carried out: the production of 4 guide elements for the instrument RESEDA and 3 guide elements for the reinstallation of the instrument TRISP following the SR5 plug exchange.

For the SR5 beam-plug exchange, the Neutron Optics group was involved in a twofold capacity. On the one hand, the three beam channels of the new plug had to be equipped with neutron guides. The guide elements made of aluminum metal substrate by Swiss Neutronics were inserted into tight metal housings designed by our Jülich colleagues. The housings are equipped with adjustment levers and locking bolts for fixing inside the beam channels. Employing our laser tracker system, these guide elements have been adjusted precisely to the planned three neutron beam axes and the whole beam plug entered into our precision coordinate system. In a second step, following the successful insertion of the new beam plug into beam tube SR5, the whole beam plug has been adjusted closely to its theoretical position with respect to the general instrumentation coordinate system. For the future installation of the instruments, the final direction of the three new beam axes has been measured and marked.

MLZ project groups

The project groups at the MLZ coordinate activities in the areas of instrument development, commissioning tasks, and technical service. They act as the interface between instrument scientists, technical support groups or companies, and management. The project groups cooperate with the newly formed group for instrument control at the JCNS institutes in Jülich and the Central Institute for Engineering and Technology (ZEA-1) of the Forschungszentrum Jülich in the fields of



Figure 1: Installation of the neutron guide NL5: the left side shows the first elements of the beam splitter dividing NL5 into NL5-S and NL5-N, while the right side gives a view through the casemate wall into the Neutron Guide Hall West with our Laser Tracker system on the beam line.

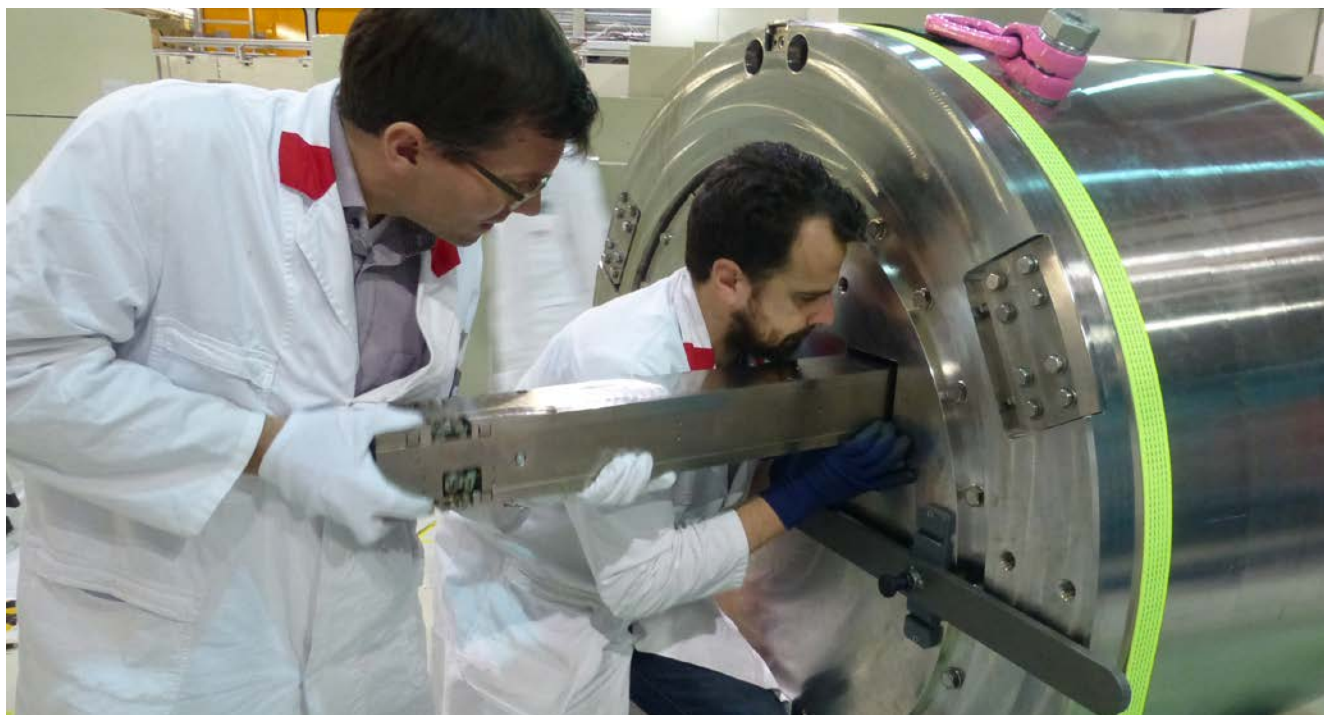


Figure 2: Inserting the metal neutron guide with its adjustment housing into the beam channel of the new beam plug SR5.

electronics and automation, control software, and mechanical engineering.

The most notable projects in 2016 included:

- The new very small angle diffractometer with focusing mirror KWS-3
- The new high resolution detector system and computer hardware at TREFF
- The advanced beam stop at KWS-2
- New sample slits at HEIDI
- NICOS for KWS-1, MARIA, SPHERES, and POLI
- Comfortable hassle-free rollout of software using open SUSE
- Considerable improvements to the SPS software

KWS-3 underwent a major refurbishment and upgrade, including a new mirror-chamber and a new sample table for heavy loads. A completely new motion control system, including new control cabinets as well as new PLC software, was put into place. The new system includes three synchronous AC drives with SINAMICS 120 frequency converters which move synchronously in order to avoid damage to the mechanics. The existing measurement software pyfrid has been adapted to the new electronics. Meanwhile, the instrument is back in normal user operation and offers improved performance, including the option to use the new sample table for heavy environment equipment such as high-field

magnets. All upgrades to the powerline and data circuits on the instruments are critically reviewed with respect to electromagnetic compatibility. As a result, it was possible to achieve considerable improvements in the signal to noise levels on selected instruments.

TREFF is a test beamline instrument operated by the TUM and JCMS. A new high resolution detector system has been introduced for TREFF. In addition to new detector electronics, the old computer hardware has been removed and upgraded with new hardware to state-of-the-art standards.

As well as the new high performance detector at KWS-2, a new variable beam stop has been installed and connected to the instrument control system. The beam stop is fixed to two thin nylon twins to minimize detector area coverage and extrinsic material in the neutron beam. A modern laser beam based positioning system in conjunction with the motion control results in a reliable positioning of the beam stop with high precision to protect the sensitive detector tubes behind the beam stop.

Two new 4-axes apertures were integrated at HEIDI. The motion control system was extended in order to facilitate the operation of this aperture through the existing instrument software.



Figure 3: Before closing the beam tube SR5 the beam plug has been adjusted to its theoretical position and the 3 beam line directions have been established employing our laser tracker system.

An in-house developed system to manage the software repository was implemented. Using the open SUSE build service, the complete software packages needed for the instruments, data evaluation and other functions can be added to the repository. Now, the build process of the appropriate software packages can easily be replicated, and in both the upgrade and downgrade direction. The surface “Marche” is the new tool to operate the instruments from remote sites, including mobile devices. New Compact-PCI systems equipped with CentOS 6 and their own packages have now been set up at all instruments operated by the JCNS.

The migration of JCNS instruments to the new MLZ unified control software stack, Tango and NICOS, is progressing very well. KWS-1, MARIA and SPHERES are operating under NICOS, while for POLI the migration has been partially completed.

Revision and optimization of the SPS-control software is a constant and very important task. The PROFIBUS (Process Field Bus) communication with the host-computer was optimized and the interfaces unified. Now, communication between the different layers of the instrument control is much faster. These improvements have resulted in an improved interplay with the NICOS instrument control software surface. In addition, by improving the SPS stepper software, full use

can be made of the new hardware functions of the recently introduced stepper modules.

Materials science laboratory

Many studies conducted at the neutron instruments require additional laboratory methods not only for sample characterization, but also for complementary information. In the case of the materials sciences, such methods are developed in our materials science laboratory. Studies carried out here range from batteries (in-operando XRD), bulk metals such as Duplex Steel (XRD), Inconel alloys (XRD) and NiMnAl-Heusler alloys (DSC + XRD) to thin films made from Indomethacin (XRR) (see Fig. 4), MBE FeNi/FePtNi films on MgO, MBE SrCoO films on Strontium-oxide substrates (XRR) and ZrN sputter films (XRD) to powders such as Ta₂O₅ (XRD), DySbO (XRD) and Upsalite (DSC) finally to polymers such as AB/BC diblock copolymers embedded with iron nanoparticles and BC/Li polymer hybrid membranes with different Li concentration (DSC).

Organisational software service

The increasing number of organizational tasks, whether they concern our visitor service, the user service or the needs of the reactor operation department, demands the support of modern software tools. In 2016, new software for the FRM II visitors' service was rolled out and replaced the existing manual handling of visits. The software creates accompanying documents for scheduled visits and provides automatic notification by email for visitors' guides. In addition, it offers online tools to plan visits by physics students.

The group was continuously engaged in developing new software applications and services for the reactor operation department, offering a better quality of service and making the existing software systems (such as DoRIS, radiation protection database, archive database and so forth) more attractive.

In spring, the UWEB system, which handles all mandatory briefings, was extended to the last group that had not yet migrated to this online system - the external workers. They can now complete their briefings prior to their arrival at the FRM II. The UWEB system was also updated. It implements improvements in training administration, slide creation and report generation.

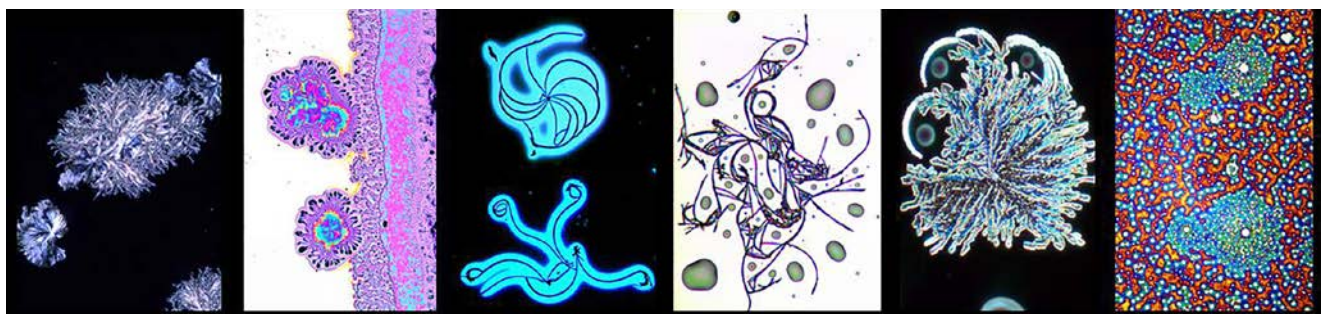


Figure 4: Science and Art - Micrographs of various crystal forms of miscarried Indomethacin thin films.

Instrument control software: NICOS and more

The development of our instrument control software NICOS in 2016 was focused on improving system stability and usability. Around 1300 code changes were performed to that end.

A number of instruments have successfully switched their instrument control software to NICOS: KWS-1, MARIA, POLI, SPHERES, and STRESS-SPEC. The latter originally used CARESS, the same control software as had been used at the V20 instrument, an experimental beamline for the ESS (European spallation source, Sweden) at the HZB (Helmholtz-Zentrum Berlin). Thus, the change in the instrument control software at STRESS-SPEC helped us to support the NICOS installation for the V20 instrument. In collaboration with the Data management, the software group (DMSC), and the CARESS maintainer, we managed to integrate access to the CARESS hardware device drivers into NICOS.

In August 2016, we organized a meeting regarding NICOS in Garching together with the DMSC group of the ESS and some in-kind partners of the ESS (STFC from the UK and PSI in Switzerland).

In a joint effort, the DMSC group integrated the EPICS support into NICOS.

A further topic reflecting international cooperation with other neutron centers is the development of SeCOP (Sample environment Communication Protocol), a task inside the ISSE (International Society for Sample Environment). The corresponding software protocol allows for the integration of sample environments from different centers into the local instrument control software.

Development of a Multi-channel pseudo-random tail pulse generator simulating neutron pulses from a ^3He -filled position-sensitive proportional counter (PSD)

Meanwhile, large-scale arrays of ^3He -filled position sensitive proportional counters (PSD) found widespread use in neutron scattering instrumentation. Installations with up to sever-

al hundreds of PSDs, as in the SAPHiR instrument for Time-of-Flight neutron diffraction and radiography under extreme pressure and temperature conditions, require new tools for developing and testing the corresponding readout electronics and data acquisition systems.

In the MLZ detector group, a multi-channel pseudo-random tail pulse generator, has been developed that can simulate neutron signals randomly distributed in time for up to eight completely independent detectors. These signals can be coupled via capacitors into the inputs of the PSD readout electronics based on the charge division method, thus approximating the charge pulse provided by a PSD.

In order to be able to adapt to the different detector types in use, the generator, which is built according to NIM standards, provides a wide range of settings which can either be controlled via switches on the front panel, or remotely via an USB 2.0 interface.

For each simulated PSD, the tail pulse generator provides two charge signals, namely a “left” and a “right” tail pulse and a corresponding trigger signal. The shape of each charge signal is a voltage step with a rise time (10 %-90 %) that can be chosen between 100ns up to 20 μs followed by an exponential voltage decay with a decay time (100 % - 37 %) that can be set between 5 μs to 1000 μs . The sum U_{sum} of the amplitudes of the “left” and the “right” signal can either be kept constant with a range $U_{\text{sum}} = 0\text{V}$ to $\pm 8\text{V}$, or varied randomly between 0V and U_{sum} . Thereby, the ratio of the amplitudes $U_{\text{left}} / U_{\text{right}}$ can be set constant corresponding to a fixed impact position in the PSD, or varied randomly corresponding to a homogenous illumination of the PSD.

The output pulse frequency can be varied from 10 Hz up to 200 kHz. Operated in random mode, the generator provides true pile-up-handling. In particular, the voltage step of each pulse is independent of the decay of a preceding pulse, thus consecutive pulses will ride up the tail of the decay. In this way, the pulse generator can exactly simulate the sig-

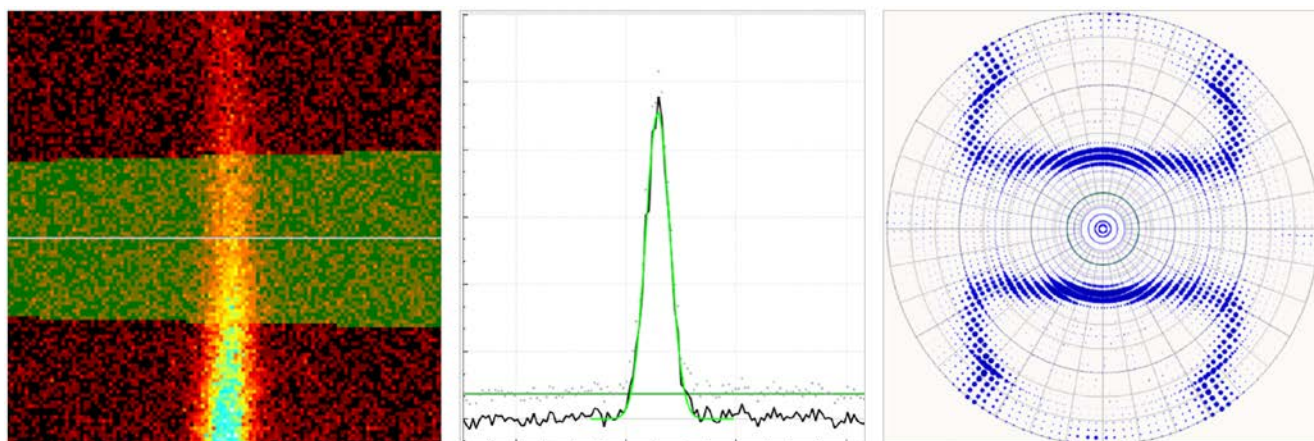


Figure 5: Workflow in STeCa2: A radial slice through a detector image (left) yields a diffractogram (center), which is then fitted, and ultimately contributes one point to the pole figure (right).

nal output of up to eight independent PSDs operated in an instrument at a steady-state neutron source, thus providing a very efficient tool for calibration and testing of the readout electronics and data acquisition in use.

Scientific Computing: Data reduction, visualization and analysis.

Data reduction and visualization for materials diffraction

At the request of those overseeing the instrument, the Scientific Computing Group took over responsibility for the data reduction and visualization software for the materials diffractometer STRESS-SPEC. The stress and texture calculator STeCa by Randau, Garbe, and Brokmeier [J. Appl. Cryst. 2011] provided an excellent starting point. To facilitate maintenance and enable future extensions, we re-engineered the data handling, and moved the visual representation to a separate layer. STeCa2 now offers (1) re-worked numerical algorithms that have vastly increased the speed of processing, (2) variable grouping of multiple detector images, (3) a new user interface designed along the typical flow of data processing, and (4) improved interactivity and visualization of reduced data. Work continues on parallelization to further improve the speed of image handling, and on the dynamic recognition of loaded metadata, as well as on additional features requested by the instrument scientists. STeCa2 is open source, and will be published so that it may also be used at other neutron and X-ray materials diffractometers.

Data analysis for single crystal diffraction

There is a widely felt need for better software for single crystal diffraction. Eric Pellegrini and Laurent Chapon of the ILL therefore embarked upon the development of a new comprehensive software package, called NSXTool. It is capable of automatic peak search and indexing, unit cell and space group determination, integration of peak intensities, and calculation of various statistics such as R-factors as measures of data quality. The software supports multiple detector geometries and data formats. In February 2016, we joined this effort. We adapted NSXTool to work with data from BioDiff,

and we are contributing to the core code. There are plans to support additional instruments in the near future, as well as to incorporate new features such as automatic intensity rescaling for merged datasets.

Data reduction and visualization for time-of-flight

The first MLZ Mantid tutorial was held on June 30th and July 1st, 2016. Twenty participants got a general overview of Mantid and learned how to use it for TOFTOF and DNS data reduction. At TOFTOF, Mantid is now in routine operation. For novice users, there is now a friendly Graphical User Interface (GUI). More experienced users can export their workflow to Python batch scripts, which they can then freely modify. For DNS in diffraction mode, a simple GUI prototype has been implemented and tested by some users. For the TOF mode, basic data reduction is ready, and will be tested and fine-tuned as soon as data become available.

Simulation and fit of grazing-incidence scattering

Work on the GISAS software BornAgain continued through 2016. The GUI now allows the user to import data, set regions of interest, mask unwanted areas, define the model of the sample, select fit parameters and perform two-dimensional fits. The simulation core was extended to include the specular peak. Roughness calculations were extended beyond the small-fluctuation limit. All polyhedral form factors were reimplemented using a generic form that provides full accuracy near singularities. The Python interface to BornAgain is now also accessible from Python 3. In November 2016, we held the First BornAgain School and User Meeting in Garching, which attracted thirty participants. In addition to that, we provided extensive hands-on tutorials at the GISAXS2016 conference in Hamburg.

The Infrastructure group

As one of our major projects to supply the new neutron guide hall east (UYM) with neutrons, the replacement of the plug JMA05 was realized in the spring of 2016. This is described in more detail in a separate report within this issue.



Figure 6: Smoking heads at the BornAgain school.



Figure 7: View into the neutron guide hall east with a spotlight on the planned building structure along its east side.

Besides this, the technical and regulatory planning for the supply of the neutron guide hall east with technical infrastructure is still work in progress. One of the related sub-projects is a large-scale building structure along the east side of the neutron guide hall east, which serves as an access and exit path to all of the new instruments and creates space for e.g. the instrument's measuring cabins (Fig. 7). In addition to that, half of this building structure also serves as housing for all of the instruments to be operated later at NEPOMUC. Here, the technical and regulatory planning will be finished by the beginning of 2017, and the building structure will be able to be installed after application to and approval by the authority.

On the other hand, one of our instrument specific contributions in the neutron guide hall west is taking shape at the instrument KOMPASS. Here, the mechanical structures and radiation shields for the KOMPASS beamline between its velocity selector and the connection to the instrument N-REX was completely assembled during the course of this year. The radiation shield of this instrument section consists of a layer structure of lead and borated PE, which were pre-assembled in a first step towards modular units within the neu-

tron guide hall east. Subsequently, these were transported to the instrumental area of KOMPASS at the neutron guide hall west, where the modular units were finally assembled to form the 1st part of the KOMPASS beamline. Left and right panel of Fig. 8 compare the shielding design and the fully assembled shielding, respectively.

By contrast, after its operating life at ANTARES I, the shielding of the old instrument shutter was the pilot project of the FRM II in order to generate a container suitable for final waste disposal. As such, the stakeholders had to call on a lot of staying power, as shown by the sequence of the following milestones: the tender for the project was issued in spring 2013, the processes for the treatment and packing of the radioactive component was applied by the Federal Office for Radiation Protection in spring, 2014, and their authorization was granted in spring, 2015. The component was then treated and packed in a container suitable for final waste disposal by the external partner (EWN), and this was completed in spring, 2016. It is worth mentioning that this is the first container suitable for final waste disposal from the public sector.

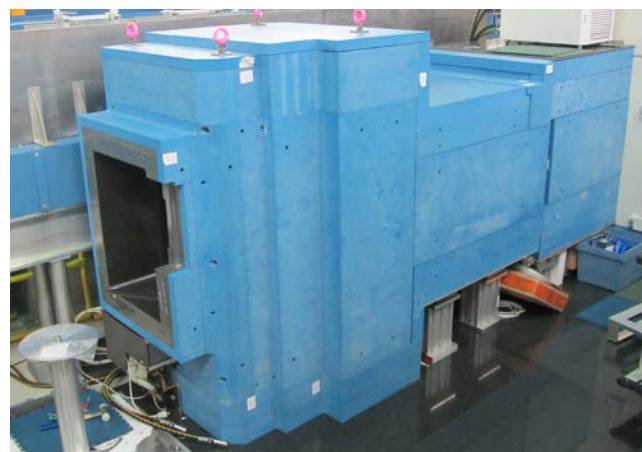
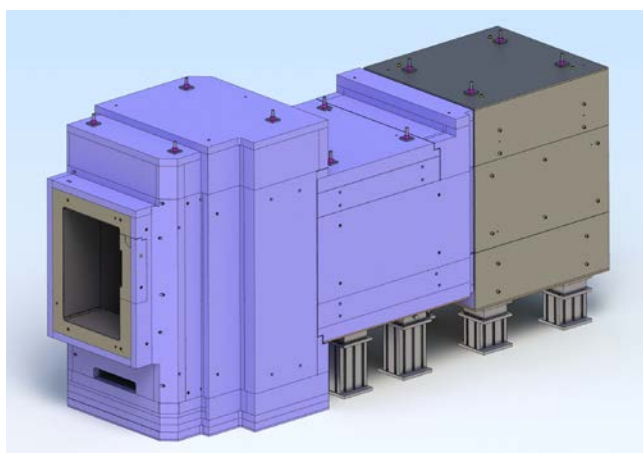


Figure 8: Shielding design (left) and the fully assembled shielding (right) of the 1st part of the KOMPASS beamline.

Exchanging the plug JMA05 in the beam tube SR5 at FRM II

E. Calzada, H. Reithmeier

Heinz Maier-Leibnitz Zentrum (MLZ), Technische Universität München, Garching, Germany

Following preparatory work that was both extensive and labour-intensive, the exchange of the plug JMA05 in the beam tube SR5 at the FRM II was finally accomplished in the spring of 2016. This very demanding task is a vital prerequisite to providing the new instruments TOPAS, POWTEX and SAPHIR, as well as TRISP, with thermal neutrons of the required intensity at their planned destination in the neutron guide hall east.

The plug JMA05 has a shielding as well as a shutter function. It provides the necessary shielding effect when turned to the 'closed' position, or connects the neutron source with the instrument TRISP when turned to the 'open' position. The plug weighs approximately 12 tons. Since it was not accessible for measurements prior to the hot phase, all planning for approval and working steps connected to those concerned with radiation protection and waste disposal in particular, were based exclusively on Monte-Carlo simulations.

The exchange of the plug JMA05 consisted of the following four more or less individual projects:

Manufacture of the new 3-channel plug:

The new 3-channel plug JMA05 was designed at the Forschungszentrum Jülich by the Central Institute for Engineering, Electronics and Analytics (ZEA) - Engineering and Technology (ZEA-1) in close cooperation with the quality control office of the FRM II.

A great deal of effort was invested in the construction and manufacture of this new plug, not simply to satisfy its functional requirements but also to optimize it with respect to a reduction in its later in-use activation through the careful selection of materials with low impurities (in particular, the low cobalt content of the materials used), and through the predictive usage of neutron absorbers at the most exposed surfaces. All this, together with the complicated documentation involved, which formed part of the quality control also monitored by the expert consulted by the approving authority,



Figure 1: Remote demounting of the magnetic field guide surrounding the neutron guide of the instrument TRISP.

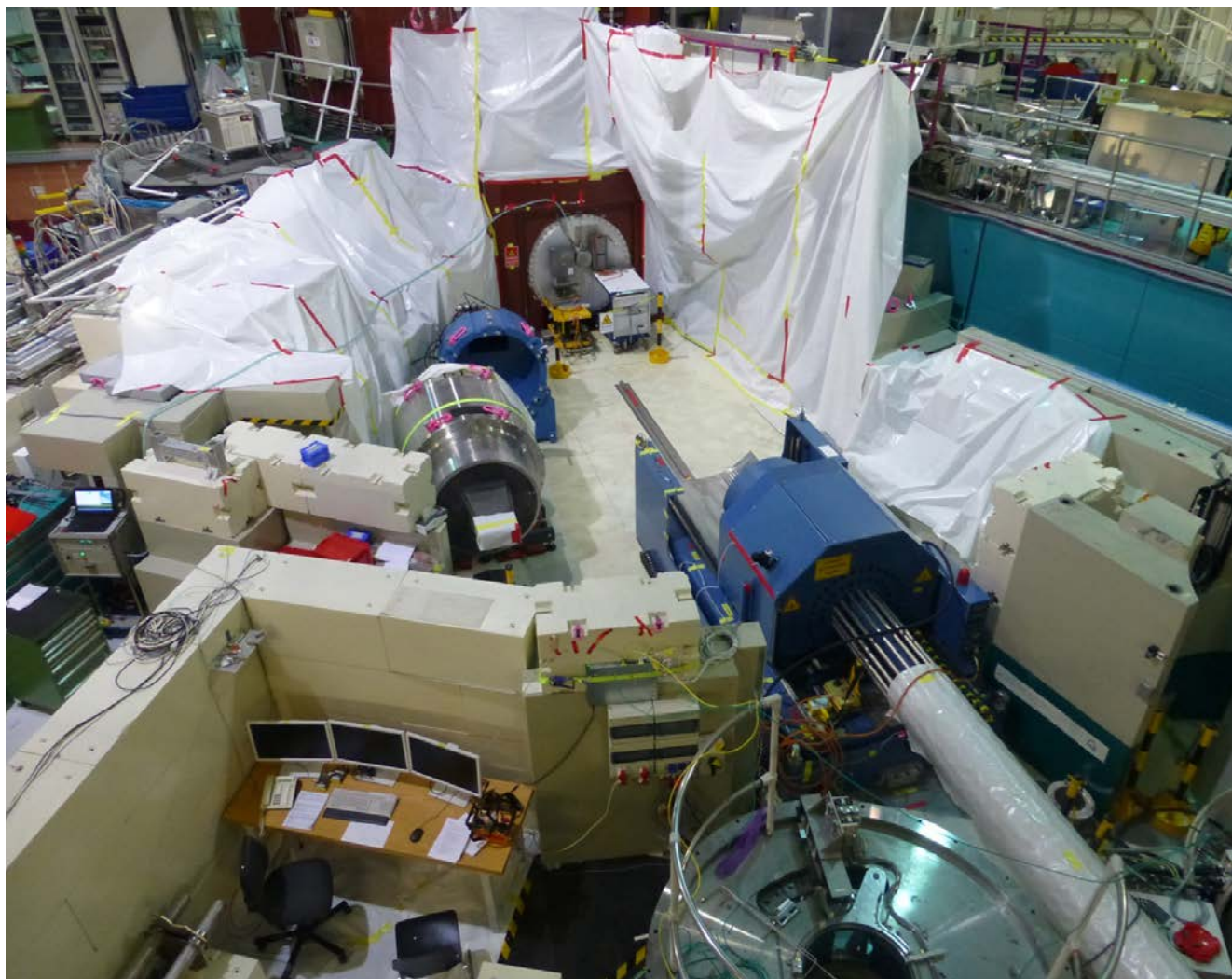


Figure 2: The final setup for the work shortly before the removal of the old plug JMA05.

wrapped up the meticulous work carried out by the engineers of Forschungszentrum Jülich (ZEA-1). The new plug and related components were delivered between 8th January and 15th March.

Establishing the working area

The working area in the experimental hall required to change the plugs is normally occupied by the permanent set-up of the instrument TRISP.

The first step in the hot phase of the project was a complete disassembly in order to make the beam tube 5 accessible.

Since the Instrument TRISP is a very large three axes spin echo spectrometer, this task involved, in particular, demounting approximately 200 tons of shielding elements. In addition, due to a substantial activation of its cobalt-coated neutron guides during its 10 years in operation, the demounting of the instrument had to be done very carefully and with foresight. This also included the development of special tools suitable for remote manipulation with the help of several cameras.

Fig. 1 shows the extremely careful demounting of the magnetic field guide which was secured by a multitude of screws around the neutron guide, an exercise which really tried the patience of the demounting team of the instrument TRISP.

Changing the plugs

Once the necessary space had been cleared, all the components of the new plug were transported in front of the beam tube 5 (SR5) and it was fully assembled there. After that, it could be fully and precisely measured by the neutron optics group engineers, particularly with respect to the position of the beam axes. Also, the in-piles and neutron guides corresponding to the three channels of the new plug could be installed, adjusted to their designated positions and - once again - precisely measured, with respect to the position of the beam axes.

Simultaneously, in another building, the planned strategy for changing the plug JMA05 was carefully being thought through by means of a dedicated setup for cold tests, and a strict list of actions to be implemented was developed and

optimized. The final step of the optimization was carried out under the critical eye of the approving authority and their consulting experts.

Following the transportation and installation of the setup for the work in the experimental hall, the technical and organizational radiation protection measures were implemented. Meanwhile, authorization for the handling of radioactive waste was granted by the Federal Office for Radiation Protection (22th March 2016) as well as approval for realizing the measures of the consulting expert from the approving authority (1st April 2016). Given this, the working team was ready to carry on with changing the plugs between 4th and 8th April 2016. For this most critical period, we relied on a small and well-trained crew of only 4 operators assisted and controlled by 2 radiation protection colleagues. Although each operator was assigned to a specific job, it was part of the safety framework that each operator was also able to undertake each of the tasks.

Technically speaking, the main working tool that allowed the most critical steps in the replacement of plug JMA05 to be remotely controlled was the so-called 'StrahlRohr-Wechselmaschine' (SRWM), which is a special machine dedicated to the replacement of heavy, and possibly hot, components within or near the biological shielding of the FRM II. This, together with a two-winged shielding door that is also remote-controlled, the moveable ceiling crane in the experimental hall and complete visual monitoring of the most

important parts of the working area via eight video cameras, enabled us to realize the critical steps by remote control from the well-shielded control console.

Once the old 2-channel JMA05 plug had been removed from the beam tube SR5 with the SRWM, the shielding door was closed to reduce radiation from the reactor. Then, the most active frontal part of the old plug, the "nose", was shielded with the help of a crane-mounted bottle-shaped shielding element which made the radioactive plug on the SRWM accessible for stages in the work to be carried out close to the plug. This bottle was specially designed for the task and, besides its shielding function, it also served as a lifting device and was suitable for transportation and final waste disposal. The old plug was then separated into two parts as its weight was greater than the loading capacity of the bridge crane, and both parts were lifted to the area of the north gate to be handed over to the disposal project team.

The SRWM was now free to be loaded with the new 3-channel plug JMA05. For this, the new plug was positioned in front of the SRWM with the help of air cushions mounted at its transport frame and carefully adjusted to fit the SRWM, so that the plug could be pulled onto the SRWM. It is interesting to note that the difference between the largest diameter of the plug and the diameter of the beam tube SR5 is only 4 mm in total, so that even a small skew discrepancy could have posed a significant problem.

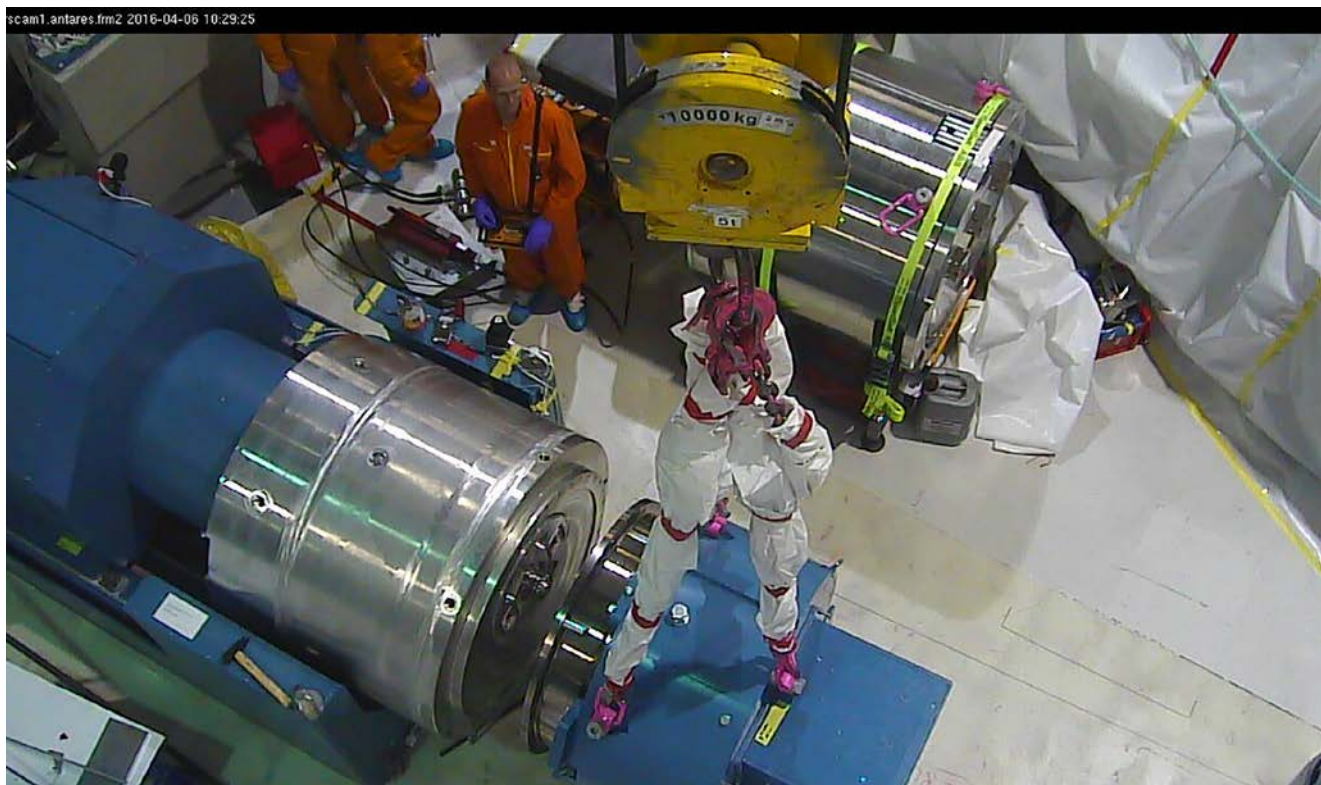


Figure 3: the old plug JMA05 after its removal from the beam tube SR5 and after its separation into its two main parts. Here, the frontal part is shielded by the bottle-shaped shielding element and fastened prior to being lifted by the crane.



Figure 4: The new plug JMA05 after its successful assembly in the beam tube SR5. This represented the end of the hot phase of the replacement of plug JMA05.

This point was the start of the hot phase of the assembly of the new plug into the beam tube SR5, which was again completely under remote control. The process for the assembly was the same as that described above, but in reverse order. Finally, the new plug was assembled at the first attempt and without any difficulty.

After this hot phase, the new plug was carefully adjusted to its final position and once again precisely measured in terms of the position of the beam axes by the neutron optics group engineers. Subsequent to this, the proper functioning of the new plug was verified and the system of the beam tube SR5 was completed over several weeks by the mounting of the related systems, such as e.g. the neutron windows and the helium purging. Again, the essential steps were part of the quality control also monitored by the expert consulted by the approving authority.

Disposal of the 2-channel plug and the radioactive components of TRISP

After handing over the components to the disposal project team in the area of the north gate, the dose values were measured and samples taken in accordance with the processes authorized by the Federal Office for Radiation Protection, the consulting expert of the regulatory authority being present. The components were then packed ready for

transportation to the external partner (GNS), where the radioactive waste is treated and packed in containers suitable for final waste disposal. Due to a matter of form, in order to comply fully with the regulatory requirements, transport to the external partner occurred 1 to 3 weeks after the transport containers had been packed. The last two of these containers included the two parts of the old plug JMA05 and were removed from the FRM II on 26th April 2016.

Conclusion

We see pursuing a zero-error strategy with strict adherence to a task list, which had been meticulously drawn up and optimized during lots of cold tests, as the basis for the success of this demanding project. No less important is the team spirit of the highly motivated crew who were eager to face new challenges, to contribute and exchange ideas in frank and open discussions, and to show respect for each other.



Reactor & Industry

Operating, enhancing and maintaining the FRM II in 2016

A. Kastenmüller

Forschungs-Neutronenquelle Heinz Maier-Leibnitz (FRM II), Technische Universität München, Garching, Germany

Only 120 service days were planned for 2016 as a longer break had been requested by our partner, JCNS, in order to replace the shielding plug of the SR5 beam tube (see page 66). The reactor was operated with cycles 39 and 40 for a total of 119.9 days in that year and thus achieved an excellent availability for work of 99.9 %.

Long maintenance break

While exchanging the shielding plug, four thimbles in the moderator tank were replaced by newly manufactured spare parts. This had become necessary since, at the end of October 2015, a small leakage had been detected in one of these thimbles, which required at least the exchange of the temperature measuring tube affected. As a precaution, the two additional temperature measuring tubes and the identical thimble of the start-up neutron source were replaced as part of this operation. In addition, the longer maintenance pause afforded the opportunity to replace the converter plates of the converter facility for the instruments MEDAPP and NECTAR for the first time (see Fig. 1), and to completely overhaul the cooling pumps of the facility.

The fuel cycles in 2016

Cycle 39 was started on schedule on 19 July after the 9-month maintenance break. There were no planned or unplanned interruptions during the cycle; the shutdown took place on 18 September, 2016, when the maximum burnup of the fuel element of 1200 MWd was reached.

Cycle 40 was also started according to plan on 17.10.2016 and interrupted once by a scram on 21.11.2016 due to a voltage drop in the external power grid. Since the cold source did not warm up during this scram, it was already possible to restart the FRM II on the following day. The cycle ended on 18.12.2016 when the uppermost position of the control rod was reached, at a burnup of the fuel element of 1198.4 MWd.

In accordance with the reporting criteria, two events had to be reported to the regulatory body. While examining the thimbles in the moderator tank, which were identical to the thimble that showed the small leak in 2015, findings were also made on the inner wall of the tube. Although the small leakage was not a reportable event, the findings in the oth-

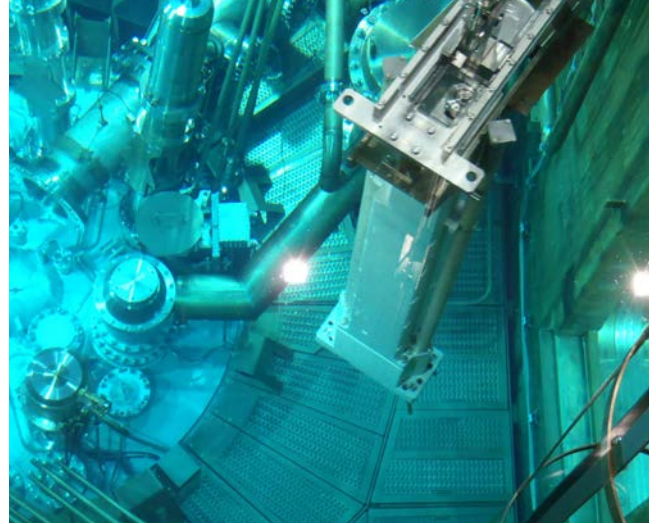


Figure 1: Intensive works for exchanging the converter plate facility for the medical application MEDAPP and instrument NECTAR.

er thimbles hinted at a systematic cause for these findings. Such a systematic cause is a reportable event, even without additional leaks in the other thimbles. As a result, all four identical thimbles were exchanged for newly manufactured parts (see Figs. 2 and 3), and an extensive examination of the findings themselves, of possible causes, and the precautions to be taken against a repetition were carried out on the parts that had been removed.

The second event was a defective battery in the uninterrupted power supply (UPS), which is doubly redundant. It was detected during a functional test at the UPS system at the end of the maintenance break: one of the two UPS failed due to this defect in the battery. The UPS are used as emergency power supplies for the cooling pumps of the converter facility during 300 s after the shutdown of the reactor. They had not been necessary during the maintenance break, and one of the two power supplies would have been available automatically, without restriction and on demand to guarantee the cooling of the converter plates. The battery in question, consisting of nine maintenance free lead accumulators, one of which was defective, was replaced by a complete set of new accumulators in the ongoing maintenance break. No further investigations were undertaken at the power supply, as the maintenance free batteries were far short of their maximum life span according to the manufacturers' data, and this appeared to be a singular defect.

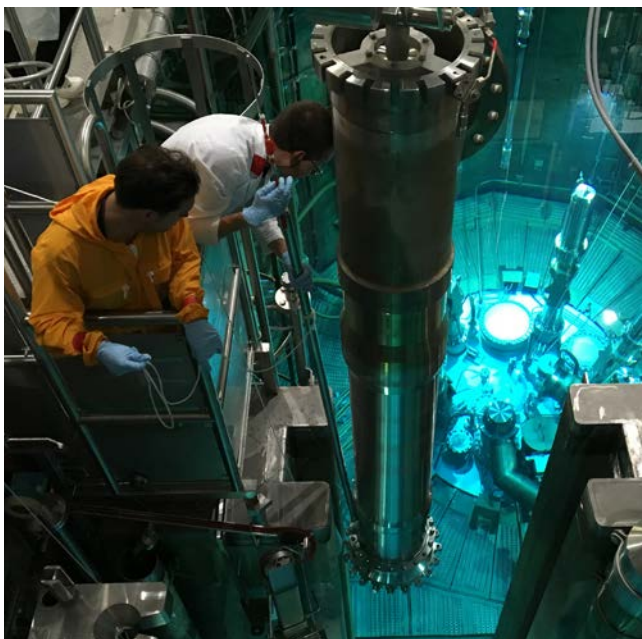


Figure 2: For changing two of the four thimbles the central channel of the fuel element had to be removed.

Safety checks and further tasks

In 2015, a periodic safety review (PSR) was carried out for the first time, 10 years after the start of routine operation, and the relevant extensive documents were submitted to the supervisory authority on time. In 2016, feedback and inquiries were received from the TSO experts on various parts of these documents, which had to be processed in part with the involvement of external companies. It is to be expected that extensive and time-consuming work on the completion of the PSR will still be necessary in 2017 in order to meet all the additional requirements of the TSO experts.

Further measures were taken to clear and prepare the construction site for a workshop and office building for the FRM II, and a laboratory and office building for the Forschungszentrum Jülich.

At the same time, FRM II staff are also partly involved in other projects such as the dismantling of the FRM (old) and related preparations, the planning of the dismantling of a former cyclotron accelerator located within the site and also in the operation of the infrastructure for the lab licensed according to § 9 AtG for nuclear fuel development in the Industrial User Center (IAZ).

In 2016, a total of 3.6 tons of silicon for semiconductors were doped, and several radioisotopes, among them Lu-177 for pancreatic cancer, were produced in the irradiation facilities of the FRM II.

The high level of safety at the FRM II was able to be sustained, and even enhanced, thanks to a total number of 1808 periodic in-service inspections, onsite inspections by independent experts from the regulatory body covering 18 different subject areas, as well as 30 modifications to the facility that had to be referred to the regulatory body.



Figure 3: The thimbles in the reactor pool were exchanged for newly manufactured parts.

Fabrication of monolithic U-Mo plates for the EMPIrE experiment

F. Alder, D. Bach, B. Baumeister, H. Breitzkreutz, T. Chemnitz, T. Dirks, T. Huber, W. M. McCollough, Ch. Reiter, Ch. Schwarz, J. Shi, Ch. Steyer, T. Zweifel, W. Petry

Forschungs-Neutronenquelle Heinz Maier-Leibnitz (FRM II), Technische Universität München, Garching, Germany

The EMPIrE (European Mini-Plate Irradiation Experiment) program is a joint European/US irradiation project designed to gather pivotal information on high-density low-enriched uranium-molybdenum research reactor fuels. To this end, EMPIrE will focus on the verification of manufacturing techniques for coating mini-sized (19 x 82.5 mm) dispersion and monolithic fuel. As part of the monolithic fuel branch, the FRM II fuel conversion group has developed, established and successfully applied a new process for the deposition of a 20 µm zirconium diffusion barrier between the U-Mo core and the aluminum cladding of fuel plates (see Fig. 1). This process step is located between the bare U-Mo fabrication by BWX Technologies Inc. (USA) and the fuel plate manufacturing by AREVA NP (CERCA, France), followed by the irradiation test in the Advanced Test Reactor (ATR) at the Idaho National Laboratory (INL, USA).

Infrastructure & Equipment

The working group “Hochdichte Kernbrennstoffe” operates an individualized double glovebox system for the safe handling and treatment of nuclear fuel under inert atmosphere in the nuclear fuel laboratory of the FRM II. One glovebox is licensed for wet-chemical work with a wide range of ac-

ids, bases and solvents. The other glovebox incorporates a multi-purpose vacuum PVD (Physical Vapor Deposition) device which offers the possibility of varying a large number of process parameters (see Fig. 2). The coating process itself is controlled by a continuously developed PLC system optimized towards a safe and stable operation for reproducible results. The entire equipment is integrated in the laboratory safety system.

Process development

One of the main development focuses of the fuel conversion group has been the application of a dense and homogeneous zirconium coating to bare U-Mo foils. The layer properties had to be adapted for proper adhesion to the U-Mo substrate and qualified for the subsequent fuel plate production process at AREVA using the C2TWP process developed by CEA, CERCA and TUM in the past, and optimized for PVD-coatings. Therefore, a continuous process of production, examination and parameter optimization has been established between the FRM II and AREVA. Bare U-Mo foils were delivered by BWXT, coated by TUM with varying parameters and then processed with C2TWP by AREVA. The impact of these variations has been examined by ultrasonic testing, x-ray analysis and optical and electron microscopy.



Figure 1: Cross-section of an uncoated (A) and coated (B) U-Mo core. The coating layer shows high homogeneity and follows the surface structure of the U-Mo core well.



Figure 2: A member of the group handling uranium inside the coating glovebox.

Two aspects have been identified as crucial for successful coating: the preparation and cleaning of the bare U-Mo and the coating parametrization. The cleaning step should remove any residues from the foil production process as well as the natural oxide layer ($\text{UO}_2\text{-U}_3\text{O}_8$) from the U-Mo surface. In a detailed study, mechanical, chemical and physical cleaning procedures have been investigated. An alkaline wet-chemical cleaning process has been identified as an appropriate first cleaning step. Subsequently, the uranium is rinsed with deionized water and dried with pressurized high-purity argon. Volatile residues from the wet-chemical process are removed by high-vacuum. Finally, directly before the coating process starts, the foils are treated with a low-pressure argon plasma, where argon ions bombard the uranium foil, removing the remaining impurities and activating the surface for the coating (see Fig. 4). The parameters studied for the coating process include working gas pressure, working distance, substrate heating and cooling as well as the application of a biasing voltage to the substrate to accelerate ions to the surface during the layer growth process.



Figure 4: A burning plasma during the cleaning process of the uranium foil.

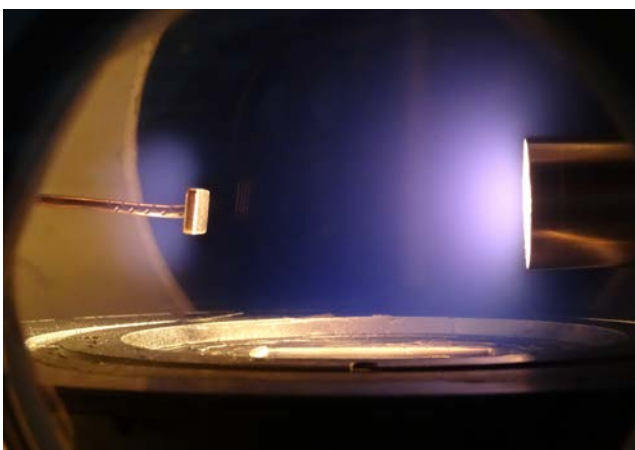


Figure 3: Preparation experiment for the industrialization of the coating process.

Production of the irradiation plates

After two test sets using stainless steel surrogates and three using depleted uranium, the final coating of the irradiation plates with high-purity reactor-grade zirconium was successfully performed on low enriched uranium (LEU) in mid-2016. Due to the high safety and quality requirements for nuclear fuel, the whole production process was monitored by a comprehensive quality assurance program according to NQA-1, including materials procurement, pre-defined working routines and the documentation of all relevant data. Subsequently, cladding was applied by C2TWP at AREVA in the fall of 2016, where twice the number of required plates passed the final conformance test, i.e. fulfilled the specification for irradiation in ATR. By transporting the irradiation fuel plates to the irradiation facility by the end of 2016, the monolithic production program for the EMPIrE project has been successfully completed.

Outlook

In parallel to the EMPIrE irradiation test, the group is already preparing the upscaling and industrialization of the process for foils with the dimensions required for fuel elements for the FRM II (~ 700 x 60 mm). Therefore, an advanced full-size coating device inside a new glovebox is currently being implemented.

The Ultra-Cold Neutron Source at the FRM II begins its non-nuclear test phase

A. Frei¹, W. Adler¹, F. Becker¹, C. Bocquet¹, F. Cristiano¹, T. Deuschle², S. Paul³, J. Schilcher¹, S. Wenisch¹, S. Wločka¹

¹Forschungs-Neutronenquelle Heinz Maier-Leibnitz (FRM II), Technische Universität München, Garching, Germany; ²Maier-Leibnitz-Laboratorium der Ludwig-Maximilians-Universität München und der Technischen Universität München, Garching, Germany; ³Physik Department E18, Technische Universität München, Garching, Germany.

Precision experiments using ultra-cold neutrons (UCNs), such as the search for a possible electric dipole moment (EDM) of the neutron or the measurement of the lifetime of the free neutron, require high UCN densities. Stronger UCN sources are presently being developed worldwide, based on the principle of superthermal UCN production and using cryo-converters made of solid deuterium (sD_2) or superfluid helium. At the FRM II, a UCN source with a sD_2 converter and sH_2 pre-moderator, placed at a distance of ~ 60 cm from the central fuel element inside the horizontal, through going beam tube SR6, is currently under construction. It can generate UCN densities of $\sim 10^4$ cm^{-3} in up to four connected experiments. These densities are more than two orders of magnitude higher compared to the currently strongest UCN source at the ILL.

to the closed supercritical He-loop. The converter contains 12.5 mol of solid hydrogen (sH_2) as a pre-moderator (volume ~ 250 cm^3) to pre-cool the incoming thermal neutron flux ($\sim 10^{14}$ $cm^{-2}s^{-1}$) to an effective neutron temperature of ~ 40 K. The sD_2 UCN converter (maximum amount 12.5 mol) is frozen to the outer surface of the converter vessel by re-sublimation of D_2 gas to the solid phase. The pre-moderated incoming neutrons can enter the sD_2 converter, where they excite solid state excitations (mainly phonons) of the crystal lattice. Solid ortho-deuterium has excited states in the energy range of 2-20 meV, so that by populating one single excited state via neutron scattering at the crystal lattice, the incoming neutron almost loses its total initial energy, and is converted into the energy regime of ultra-cold neutrons. The UCNs generated by this process can leave the sD_2 converter, are guided to the SR6 beam port exit in the experiment hall, and fed into connected experiments.

The central part of the UCN source is the converter vessel, a double walled toroidal shaped aluminium cap piece, which is cooled by a continuous flux of a closed supercritical helium cooling loop. The necessary cooling power of 1.0 kW at 5 K is supplied by two cold boxes (AirLiquide Helial 2000)

In the course of the last year, a test setup of all the important components of the UCN source has been installed at the Maier-Leibnitz-Laboratory (MLL). Three vessels, one filled with liquid nitrogen and two with gaseous helium, have been set up outside, south of the MLL building (see Fig. 1).



Figure 1: Newly built housing to the south of the MLL for the He-compressors of the UCN-source, with two helium gas tanks (on the left) and a liquid nitrogen tank (on the right).

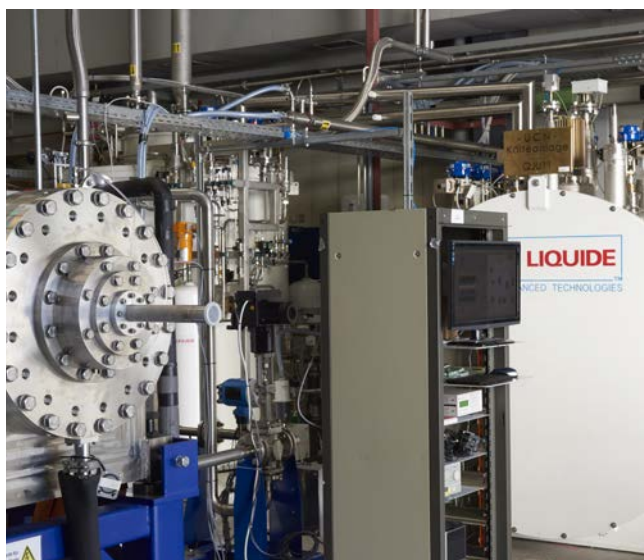


Figure 2: Right: Third cold box of the UCN cooling machine, housing two vessels containing liquid helium and a pump to drive the supercritical helium loop, which cools the converter. Left: End of test beam tube SR6 with the UCN converter inside and connected to the third cold box.

A hall, 70 m² wide and 3.70 m high made out of wood houses the two compressors (electrical power 250 kW each) of each cold box accompanied by two oil separators and water filled circuits to cool the compressors. A small cooling tower next to the compressor hall removes the heat produced from the water cooling circuits. The helium cooling machines themselves are located inside the Maier-Leibnitz-Laboratory. Two conventional cooling machines with a power of 500 W at 5 K each remove the heat from a closed cooling cycle of supercritical helium. Each machine expands the previously

compressed helium using seven heat exchanger stages (the first stage precooled with liquid nitrogen) and two expansion turbines to produce liquid helium in two vessels in the third cold box (see Fig. 2). The liquid helium is then used to cool a closed loop of supercritical helium via two heat exchangers. This closed loop, which is driven by a special pump, is connected by cryogenic transfer lines to a small vessel inside the SR6 beam tube housing the solid deuterium and the solid hydrogen.

A 1:1 rebuild of the beam tube SR6, where all the converter parts of the UCN source stay, has been set up (see Fig. 3). The helium cooled converter vessel is placed in the middle, inside the beam tube SR6. For non-nuclear tests, the heat input of the FRM II to the converter is simulated by several heating devices.

Now that all these systems are in place, the UCN source has embarked on its non-nuclear test phase. In these tests, all parameters relevant to operating the cooling machines and all necessary auxiliary systems will be varied and optimized in order to freeze out deuterium and hydrogen in a dedicated way, using the simulated nuclear heat load of the FRM II. After the tests, which will take approximately one year, the whole cooling machine, together with the helium and liquid nitrogen vessels, will be transferred to the FRM II, and all the other parts of the source and auxiliary systems will be built and installed.

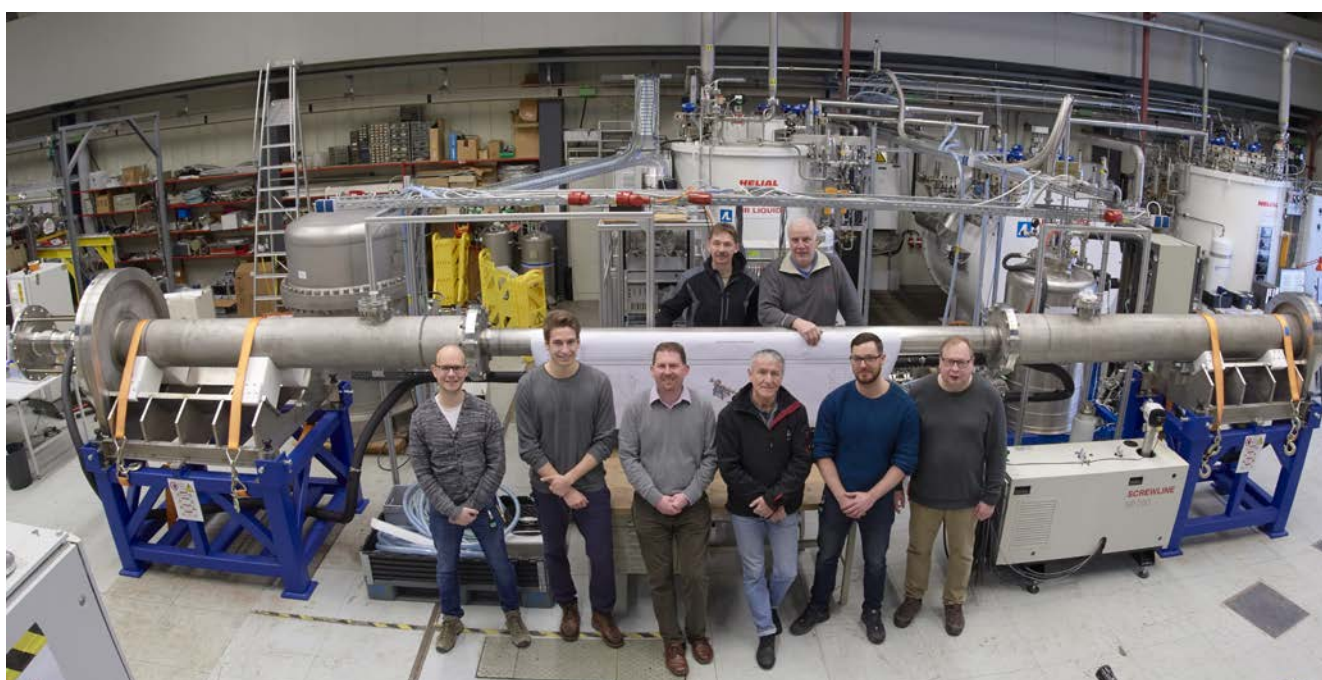


Figure 3: The UCN team (from left to right: S. Wlokka, F. Becker, A. Frei, T. Deuschle, C. Bocquet, J. Schilcher, S. Wenisch, W. Adler) in front of a 1:1 rebuild of the SR6 beam tube of the FRM II.

Figures, numbers and information about visitors, events, staff and publications are presented in the chapter Facts & Figures.

The year in pictures



January 2016

During the maintenance break, the old beam plug at the neutron guide SR5 was exchanged for a new one with three instead of two beam channels. It had been manufactured at the Forschungszentrum Jülich by the Central Institute for Engineering, Electronics and Analytics (ZEA) – Engineering and Technology (ZEA-1) during 2015. The installation was supervised and performed by E. Calzada (FRM II) and his group.

April 20th

The “Lüscher Seminar” for teachers of natural sciences took place in Zwiesel, Bavarian Forest, for the 40th time. It is designed with the utmost care by its scientific directors, Prof. Winfried Petry (1st row, 2nd from left) and Prof. Peter Müller-Buschbaum (first row, right) from TUM, and is always in tune with current research. The topic for the anniversary seminar was “Biophysics”.



May 25th

In late summer, the newly constructed light weight hall was completed. It houses the material of the dismantled interior of the Atomic Egg. The clearance box destined to perform radiation measurements on the dismantled material will also be integrated into the new hall. The radiation protection certifies the dismantled material as suitable for full or restricted release. The construction measures 20 x 20 m and is located on the premises of FRM II close to the Atomic Egg.

May 31st

Within the framework of the International Diplomats Program (IDP), 12 diplomats from North Africa, the Middle East and South and Southeast Asia were invited to the FRM II to become better acquainted with Germany from different perspectives. The IDP is an innovative dialogue and meeting platform, which covers a wide range of topics ranging from German-speaking aspects to European and global issues.



June 2nd

Visit of an international delegation from the EURATOM Supply Agency (ESA) which included the ESA director-general Stamatios Tsalas (2nd from the right) and the head of the Nuclear Fuel Market Observatory Sector, Remigiusz Baranczyk (in the middle), who were interested in gaining deeper insights into the use of uranium at the FRM II.

June 22nd

At the invitation of the Federal Ministry for the Environment, Nature Conservation, Building and Nuclear Safety (BMUB), a delegation of the German-French Commission on questions of safety in nuclear facilities (DFK) came by to visit the FRM II and were shown around by the technical director, Dr. Anton Kastenmüller (2nd from left).





July 12th

Physics can also taste very sweet – this is one of the things that 19 pupils from grade 3 of the elementary school Garching Ost learned during their visit to the Research Neutron Source Heinz Maier-Leibnitz. They made an atom model from toothpicks and marshmallows and exercised their skills as neutron scatterers at a neutron ball toss.

August 30 - September 1st

During the summer vacation, 12 female pupils aged 10 to 12 spent three days in a workshop organized by the Gerd-Stetter Foundation, the TUM Physics Department and the MLZ. They learned a lot about light, neutrons and their applications. Technique and programming were also features of the workshop in the annual TUM programme “Girls do tech”.

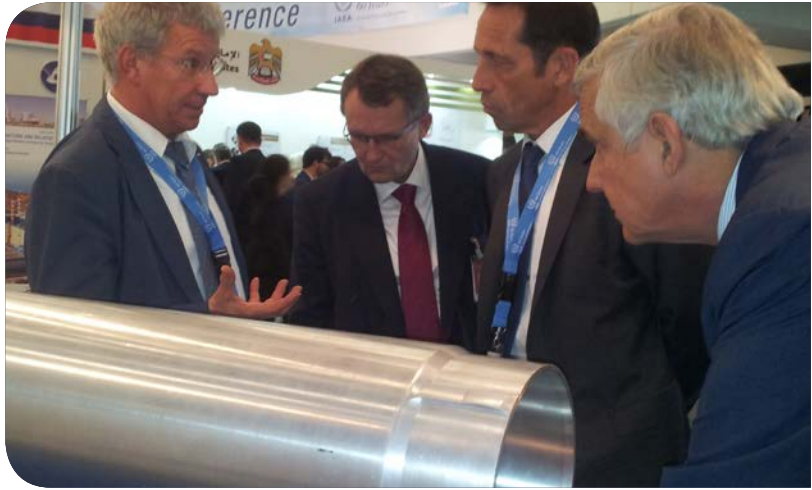


September 10th

The MLZ is one of the exhibitors at the Garching Autumn Days, a regional trade fair. The total sum this year: 85 exhibitors, 30 degree heat, and the majority of Garching's residents in the centre in the shade. Nevertheless, the visitors had many questions about neutrons and enjoyed the fact that they were able to ask them all, while their children were busy with tossing the neutron balls or watching moving lego instrument models.

September 26th - 30th

The MLZ had the honour of representing Germany at the 60th General Assembly of the IAEA at the UN headquarter in Vienna, Austria. A large number of visitors came by to ask questions, especially in regard to the German nuclear power phase-out and the design of the FRM II's compact core, which was as an exhibit at the booth.



October 22nd

Significantly more than 10,000 visitors came to the Open Day on the Garching campus, enjoying at pleasant temperatures and bright sunshine. Thanks to improved planning and dedicated staff, more visitors than usual were able to visit the research neutron source, namely 557. The MLZ booth was always full to capacity.

November 2nd

After ten years of service, the administrative director Dr. Klaus Seebach (right), retired in November 2016 and was succeeded by Johannes Nußbickel, who shares with Klaus Seebach a long and distinguished background in industry..

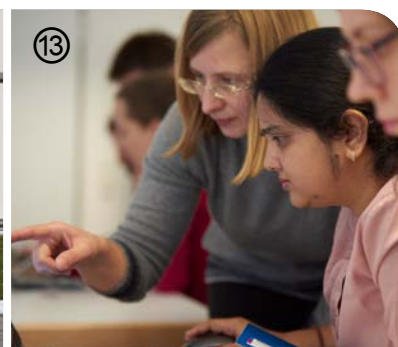


Workshops, Conferences and Schools

①	Neutrons in Research and Industry, weekly seminar	11 January – 19 December	Garching, TUM
②	Workshop “Fitting the spin wave spectrum using SpinW”	25 – 26 February	Garching, TUM
③	Workshop “Materials Analysis Using Diffraction” (MAUD)	21 April	Garching, MLZ
④	11 th International Conference on Polarised Neutrons for Condensed Matter Investigations (PNCMI)	4 – 7 July	Freising, JCNS
⑤	Conference “Neutrons for Energy”	18 – 21 July	Bad Reichenhall, MLZ
⑥	F-Praktikum Practical Training for TUM students	25 – 30 July	Garching, MLZ, TUM
⑦	Conference “50 Years of Neutron Backscattering”	2 – 3 September	Garching, MLZ, ILL, ISIS



⑧	20 th JCNS Laboratory Course – Neutron Scattering	5 – 16 September	Garching / Jülich, JCNS
⑨	VDI-TUM-Expertenforum “Industrial Workshop on high performance materials – challenges for non-destructive testing”	15 September	Garching, TUM
⑩	ESS Satellite Meeting	16 September	Garching, MLZ
⑪	JCNS Workshop 2016 hosting FLIPPER on single-crystal diffraction with polarized neutrons and Neutron Scattering from magnetic systems	3 – 10 October	Tutzing, JCNS
⑫	Workshop on SoNDe Application in Neutron Detection	17 – 19 October	Freising, JCNS
⑬	1 st Born Again School and User Meeting	21 – 22 November	Garching, MLZ
⑭	F-Praktikum Practical Training for TUM students	12 – 17 December	Garching, MLZ, TUM



Awards

June 2nd

Samantha Zimnik was awarded with the Laura Bassi price of the Technical University of Munich for her outstanding scientific achievements in the field of surface physics at the positron source NEPOMUC.



December 7th

In recognition of his commitment to the Campus Choir Garching (CCG), the Technical University of Munich was awarded the Karl Max von Bauernfeind Medal to Franz Michael Wagner of the FRM II (left).

May 10th

Dr. Tanja Huber was awarded the Karl Wirtz Prize of the German Nuclear Society (KTG) for her doctoral thesis “Thermal Conductivity of High Density Uranium-Molybdenum Fuels for Research Reactors”.

**September 7th**

Experimental physicists Prof. Dr. Christian Pfeleiderer (right) and Prof. Dr. Peter Böni (left) from the physics department of TUM were awarded the European Physical Society's prestigious Europhysics Prize. They got the prize for the “discovery of a skyrmion phase in manganese silicon” and shared it with three theoretical physicists: Prof. Alex Bogdanov (Dresden), Prof. Achim Rosch (Cologne) and Prof. Ashvin Vishwanath (Berkeley).

September 21st

KFN chair Prof. Dr. Tobias Unruh (right) and Prof. Dr. Winfried Petry (left) awarded once again a Garching neutron researcher the Wolfram Prandl Prize for young scientists in the field of research involving neutrons: Dr. Anatoliy Senyshyn. He won the prize for his outstanding research in the field of lithium-ion batteries, which he observed at atomic level in live hook-up.



From science to media: the public relations office

C. Kortenbruck, A. Voit, B. Tonin, C. Niiranen, C. Hönl

Heinz Maier-Leibnitz Zentrum (MLZ), Technische Universität München, Garching, Germany

We have been successful in our aim of keeping the neutron source and the MLZ in the limelight, both locally and internationally. We sallied forth and presented the neutron source at many venues and were rewarded with valuable feedback, including requests for radio interviews, film projects and talks.

Collaboration with and for pupils and students

The first few talks within the framework of our new pupils' programme took place and, together with the Gerda-Stetter foundation and the TUM physics department, we organized a three-day hands-on practical workshop aimed exclusively at girls at the TUM ("Mädchen machen Technik"). In addition, collaboration with the Gymnasium in Garching that traced the history of the "Atom-Ei", the first research reactor in Germany, resulted in an impressive documentary made by the students, which is also available on YouTube. The Lüscher-Seminar, a yearly workshop for physics teachers, celebrated its 40th anniversary in 2016 and we were asked to design the celebration brochure. Prof. Petry and Prof. Müller-Buschbaum have been organising this two-day workshop in Zwiesel, in the Bavarian Forest, for several years now which is always rich in information about new methods and actual research results.



Figure 1: Astroblogger Ricardo Garcia de Soto came by and made some video interviews with scientists at the MLZ.

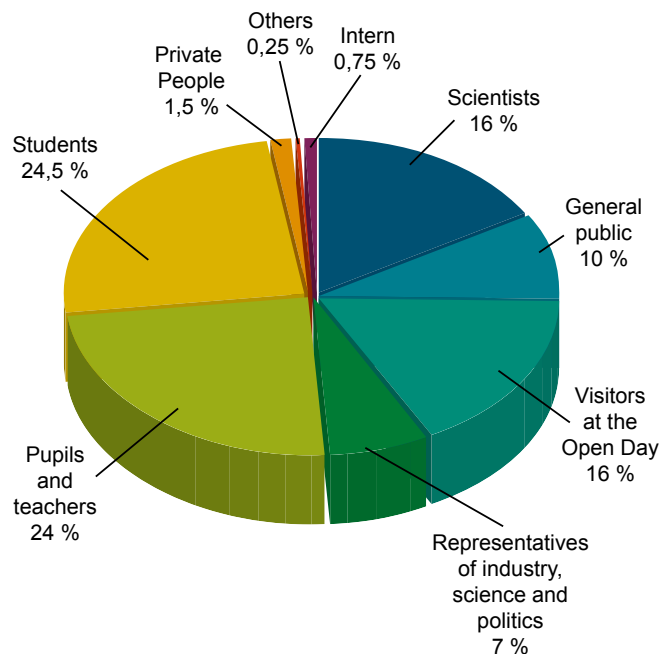


Figure 2: Our visitors in 2016 divided in several categories: almost half of them are young people, either pupils or students.

More visitors than in previous years

Seminars and courses for students at the TUM are listed online and, in 2016, we arranged to offer a new tool allowing students to book an open guided tour every month. Since its launch, the online registration has attracted many more students (24,5 % of all visitors) to the FRM II (see Fig. 2). In total, 3337 people visited the neutron source in 2016, more than in any previous year. The open day alone attracted 557 visitors. Credit is due to our scientists, students and other staff members who have escorted the visitors with so much enthusiasm.

Media relations

A Munich theatre company (Volkstheater) was interested in a film shoot for one of their series on physics (see Fig. 3). It was quite innovative, involving a mixture of films, interviews and small simple experiments, and ending with a humorous discussion with the physicist, Prof. Harald Lesch, well-known to television audiences. We also welcomed to the FRM II photographers who wanted to take photographs on their own account, mainly for exhibitions. The advantage for us was a lot of new attractive pictures which we were able to use to enhance our press releases and web news. We also had two radio interviews with Deutschlandfunk, one dealing with the

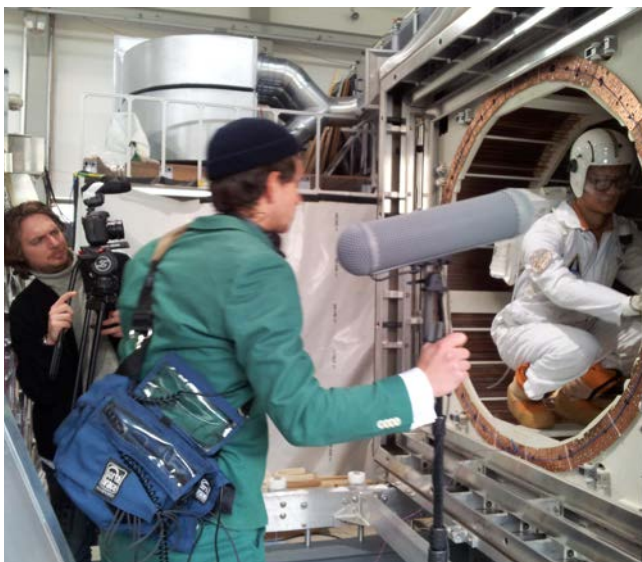


Figure 3: Even a theatre company chose the FRM II for some spectacular shootings for their production about physics in the Volkstheater Munich.

planned ^{99}Mo test facility and the other with the planned conversion of the FRM II to lower enrichment fuel. Both will be broadcasted in early 2017. Furthermore, an established video blogger from Argentina came as a guest and shot some movies about his tour of the FRM II (see Fig. 1). The completed film has not yet been published.

In 2016 we published 52 news reports on our two web pages, compared to 37 in 2015. In a few cases, contributions originated from partner institutions, mainly from the Forschungszentrum Jülich. Since February, we have also been running a facebook page (www.facebook.com/frmII) which has attracted quite a lot of attention in this short time (60 likes). In total, we have accumulated 114 media reports focusing on the FRM II and MLZ in 2016, 28% of which featured scientific topics.

Additionally, we produced three new English flyers for molybdenum-99 production, fuel conversion and industrial applications.

Collaboration with other institutions

Sebastian Mühlbauer gave a talk in the “Science for everybody” series of weekly sessions at the Deutsche Museum, Munich, which was very well attended. The model making department of the museum is currently building a model of the FRM II’s reactor pool. Both these collaborations will be followed up in the course of the next few years.

Collaboration with the physics department has also grown over the last few years and is now very close and supportive. Examples are the online booking tool for TUM students, the common workshop in the TUM programme for pupils and young students as well as the Open Day in October. This



Figure 4: The 12 girls in the workshop “Physics and technics made easy” had a lot of fun and information during the three day workshop during the summer vacation.

year we initiated an additional visitors’ survey to get more information about what our visitors would like to see, learn and do. The results were much as anticipated, but nevertheless reassuring: The visitors would welcome the chance to talk to scientists, to see even more labs and discuss with researchers what is going on in research. In the final analysis, they are very happy with the guided tours (grade 1,5) and the opportunity to learn more about the FRM II.

Special events

In the summer and autumn of 2016, the FRM II participated in two trade fair exhibitions, presenting a stand: locally at the two-yearly Garching autumn days and internationally as a German representative at the IAEA General Assembly in Vienna. On both occasions the audience was very interested and enthusiastic.

The year as seen from the User Office

R. Bucher¹, F. Carsughi¹, C. Hönl², I. Lommatzsch², C. Niiranen², B. Tonin²

¹Jülich Centre for Neutron Science (JCNS) at MLZ, Forschungszentrum Jülich GmbH, Garching, Germany; ²Heinz Maier-Leibnitz Zentrum (MLZ), Technische Universität München, Garching, Germany



One gets the impression of a quiet year at the User Office. No big events, but a lot of small changes and new ideas on how to improve the service for our users!

NMI3 discontinued

The *Integrated Infrastructure Initiative for Neutron Scattering and Muon Spectroscopy* NMI3 was a consortium of 18 partner organisations from twelve countries and included eight facilities. In addition to Joint Research Activities aimed at developing new techniques and methods as well as schools and workshops for future generations of users, transnational access was funded. This Access Programme gave European users access to all relevant European research facilities free of charge. Furthermore, at the MLZ, two people per experiment were allowed to hand in their travel, accommodation, and subsistence costs, and ask for reimbursement. The result was something to be proud of: Some hundred experiments between 2012 and 2016 could be covered by the funding of 1.63 Mio €.

The question then arose: what to do now after the end of the project? An average of 40% of our experimenters come from European countries outside Germany. In order to ensure future access for them, the collaboration partners of the MLZ decided to step in. The budget is limited as users from German universities are also granted financial support by the MLZ – therefore, only one person can now be reimbursed for all costs. We are convinced that, in this way, we can support as many experiments as possible. During the two cycles in 2016, more than 30 experiments benefitted from this!



Figure 1: Winfried Petry, Scientific Director of the MLZ, welcomes the referees warmly.

News from the review process

In 2016, only one proposal round took place. This was due to the shutdown necessitated by the exchange of the beam plug and the shifting of the restart. This time, the review panels met at a new location. Since the first joint MLZ review in 2012, the meeting had been held in Ismaning, at the Comundo Conference Centre. Unfortunately, this facility closed at the end of 2015 and a new venue had to be found for all seven panels. We discovered what we were looking for at Munich airport, saving all participants a lot of travel time. All enjoyed the productive time there!

During this review, a waiting list of proposals was established. This means that a few proposals to be carried out at each instrument were selected by the referees to cover the possibility that accepted proposals had already been measured. This helps to prevent gaps in the instrument time schedule and, therefore, prevents a waste of neutrons. We were happy when we received positive feedback from the users!

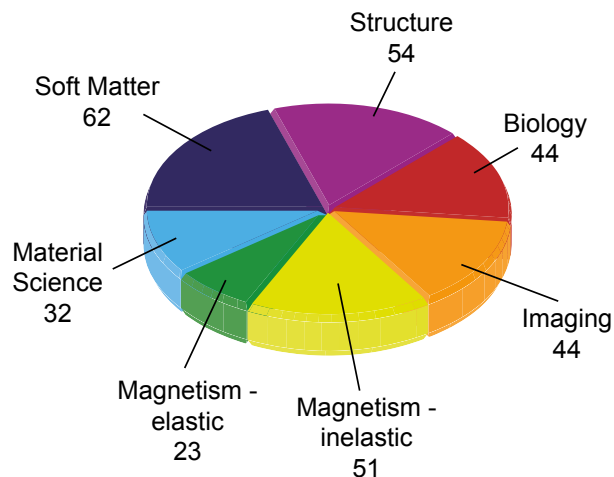


Figure 2: Distribution of proposals to the review panels.

For this 21st proposal, a total of 310 proposals were submitted. The panels covering *Soft Matter*, *Structure*, and *Magnetism inelastic* dealt with most of them, followed by *Biology* and *Imaging* with an equal number of proposals, while *Material Science* and *Magnetism elastic* attracted the smallest number.

The proposers requested 2012 beam days of which only 1181 could be allocated. Almost 60% – that is to say 183 proposals – were accepted and the proposers received an

invitation to carry out their experiments. Since the MLZ houses one of the two existing neutron sources in Germany, it was not surprising that the majority of proposers were working at German institutions and universities. However, 82 proposals from other EU countries showed that there is also a high demand and the decision to support those users financially even after the end of NMI3 was a good one!

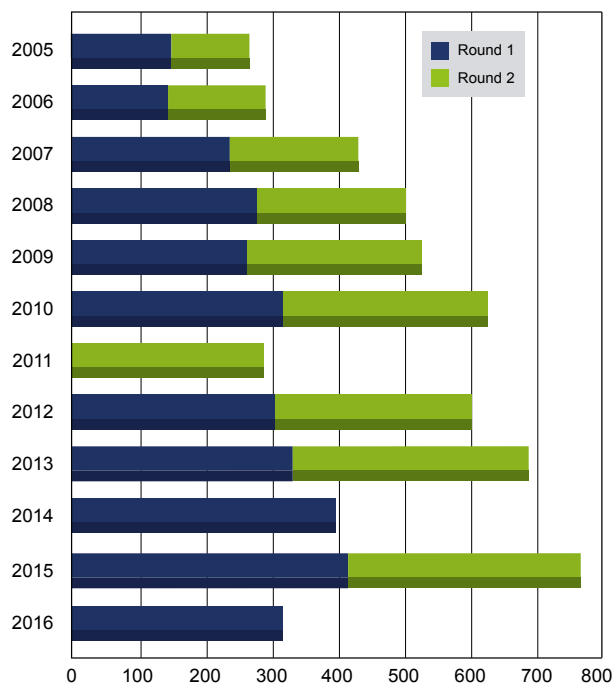


Figure 3: Overview: All submitted proposals since 2005.

More comfort for users

New users and those who visit us only rarely, in particular, often feel a little bit lost on arrival. In order to make their situation more comfortable, we set up the *User Liaison* this year. Each working day at half past eight in the morning, the User Office welcomes and accompanies them to the Radiation Protection Office after providing some general information about the site and things like lab coats etc. After a successful check-in at Radiation Protection, we hand the user over to the local contact – the experiment can now start!

Mobile User Office

Two conferences invited us to attend in 2016. In March, the annual *Spring Meeting of the Condensed Matter Section (SKM)* of the *Deutsche Physikalische Gesellschaft (DPG)* was held in Regensburg. We were happy to meet many of the 5027 participants at our booth there! We were able not only to present the possibilities at Garching, but also advertise the special focussed section “Magnetism as seen by neutrons” organised by scientists of the MLZ. Five speakers tempted the audience by sharing ideas about the breadth of the field as well as the diversity of methods and their impact on recent research.

In September, Kiel called for a visit. The *German Conference on Neutron Scattering* attracted more than 200 researchers engaged in experiments with neutrons for three days of inspiring talks and fruitful discussions. And last, but by no means least, a visit to our booth there!

Saying ‘bye to the blog

In February 2014, we started blogging from the User Office *Always on Fridays*. The reason for it was the start of a six-month maintenance break – we wanted to keep our users updated about the ongoing work. Although it had been planned to stop writing once we restarted in August 2014, we continued because the feedback was very positive and we enjoyed telling stories once a week: We introduced the animals living on site (two ducks and our cat), witnessed the rescue of a snake, showed internal processes at the MLZ, dug deep into the archives of the old neutron source FRM, gave information about a sudden shutdown, blogged from conferences and events we participated in, and explained the exchange of the beam plug during the last long break.

When neutrons were back after that break in July 2016, we decided to stop because many new tasks made demands on our time. The blog is now history - one eye laughing, the other crying.



Figure 4: Impressions from the Spring Meeting at Regensburg – we reported “live” from the conference in our blog.

Organisation

FRM II and MLZ

The Forschungs-Neutronenquelle Heinz Maier-Leibnitz (FRM II) provides neutrons for research, industry and medicine and is operated as a Corporate Research Centre by the Technische Universität München (TUM). The scientific use of the FRM II, with around 1000 user visits per year, is organized within the “Heinz Maier-Leibnitz Zentrum” (MLZ).

The chart below shows the overall network comprising the neutron source FRM II and the MLZ, as well as the funding bodies and the scientific users performing experiments at the MLZ addressing the grand challenges of our todays society.

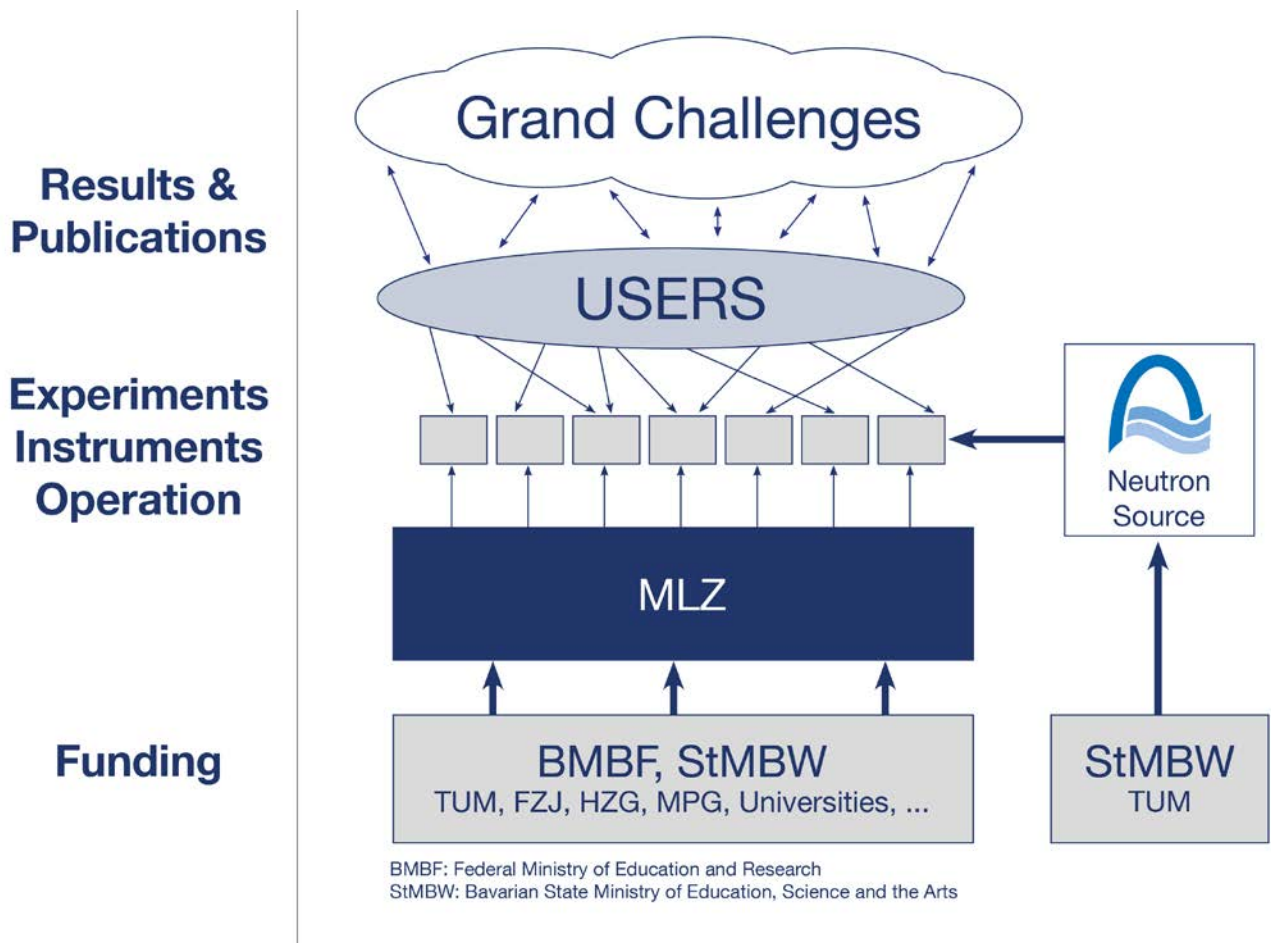


Figure 1: The neutron source FRM II and the user facility MLZ.

Scientific Director MLZ, FRM II

Prof. Dr. Winfried Petry

Technical Director FRM II

Dr. Anton Kastenmüller

Scientific Director MLZ, HGF

Prof. Dr. Thomas Brückel

Administrative Director FRM II

Johannes Nußbickel

Scientific Cooperation at the Heinz Maier-Leibnitz Zentrum (MLZ)

The Heinz Maier-Leibnitz Zentrum with its cooperation partners Technische Universität München (TUM), Forschungszentrum Jülich (FZJ) and Helmholtz-Zentrum Geesthacht (HZG) is embedded in a network of strong partners including the Max Planck Society (MPG) and numerous university groups exploiting the scientific use of the Forschungs-Neutronenquelle Heinz Maier-Leibnitz. The organizational chart of the MLZ is shown below.

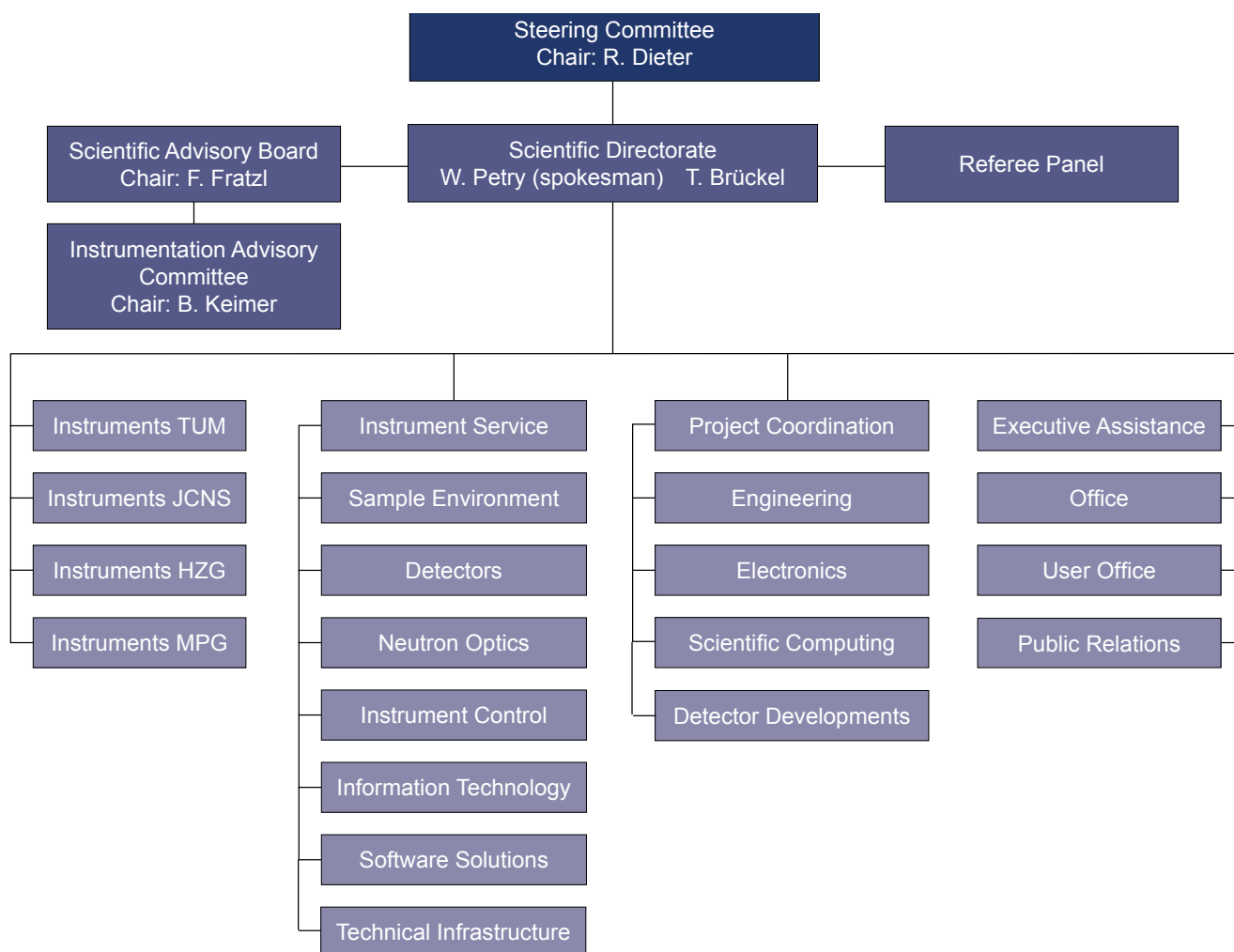
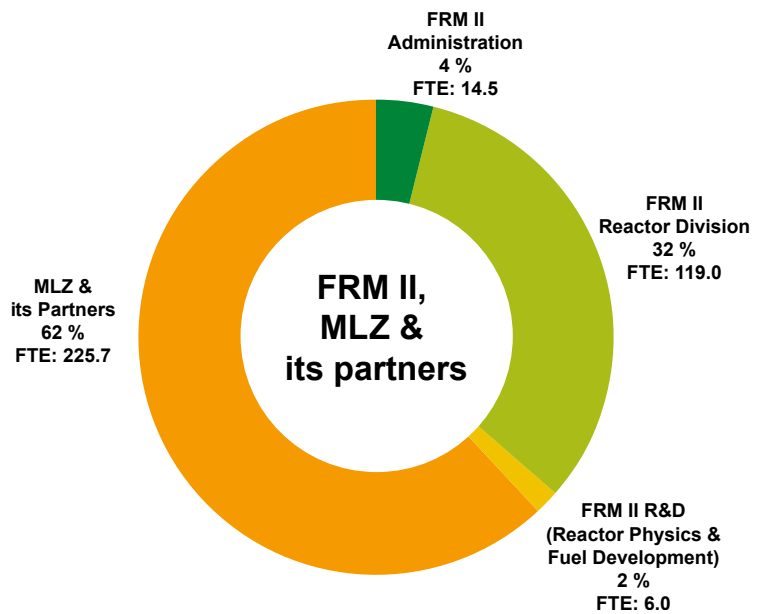
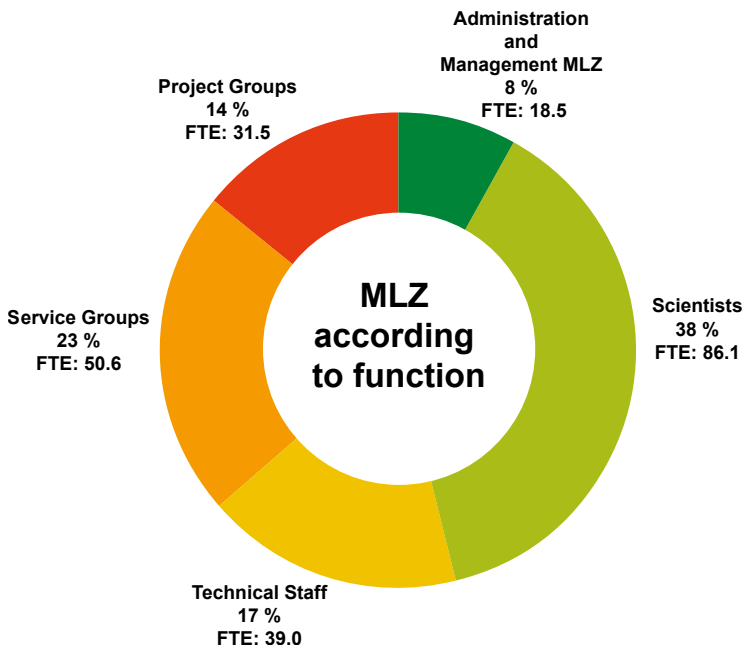
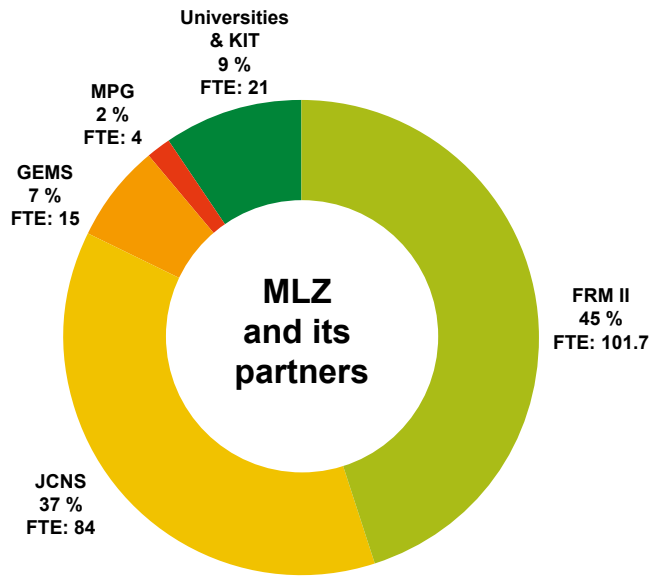


Figure 2: Organisational chart MLZ.

Staff

The charts below show the staff of MLZ and FRM II. The staff of MLZ according to its share among the partners with a detailed view according to the function within the MLZ is depicted as well.

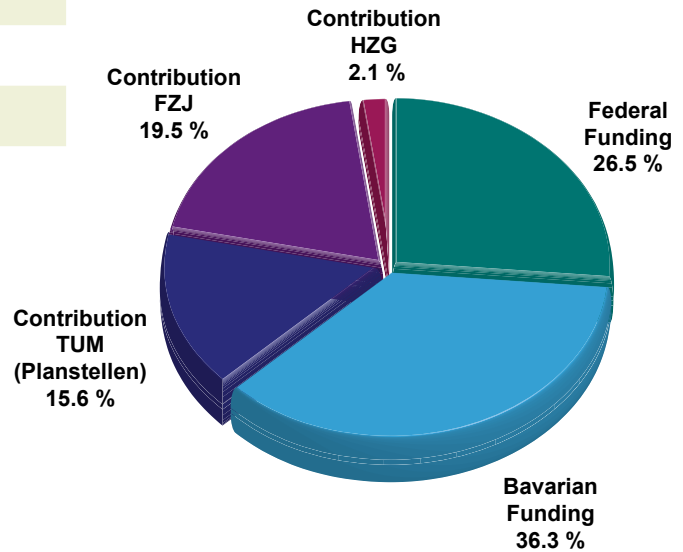


Budget

The tables and charts below show the revenue and expenses in 2016.

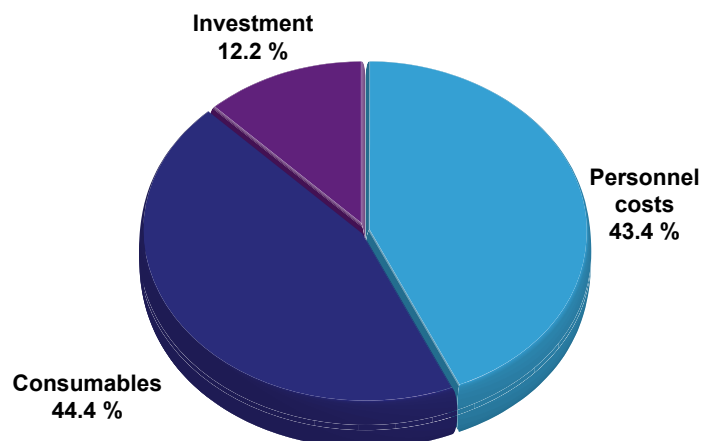
Revenue 2016

Federal Funding	16.700.000 €
Bavarian Funding	22.850.470 €
Contribution TUM (Planstellen)	9.804.852 €
Contribution FZJ	12.278.184 €
Contribution HZG	1.320.000 €
Total	62.953.506 €



Expenses 2016

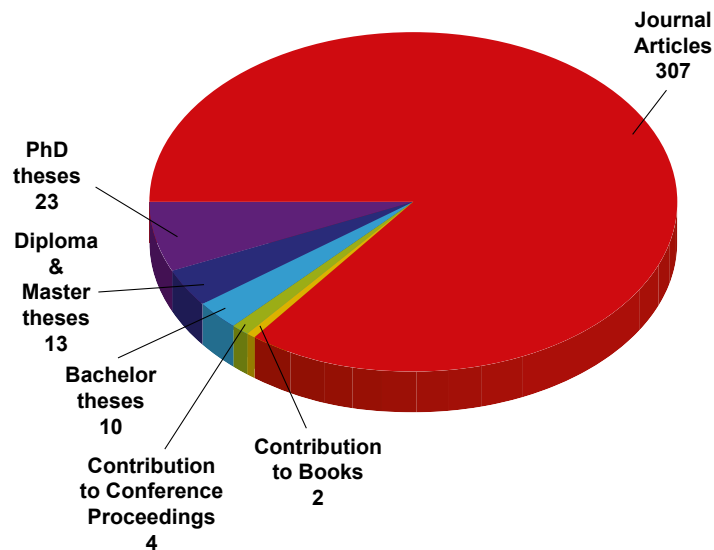
	TUM (€)	FZJ (€)	HZG (€)	Total (€)
Personnel costs	15.363.107	8.546.473	1.355.000	25.264.580
Consumables	21.582.123	3.964.887	311.000	25.858.010
Investment	4.923.875	2.032.985	119.000	7.075.860
Total	41.869.105	14.544.345	1.785.000	58.198.450



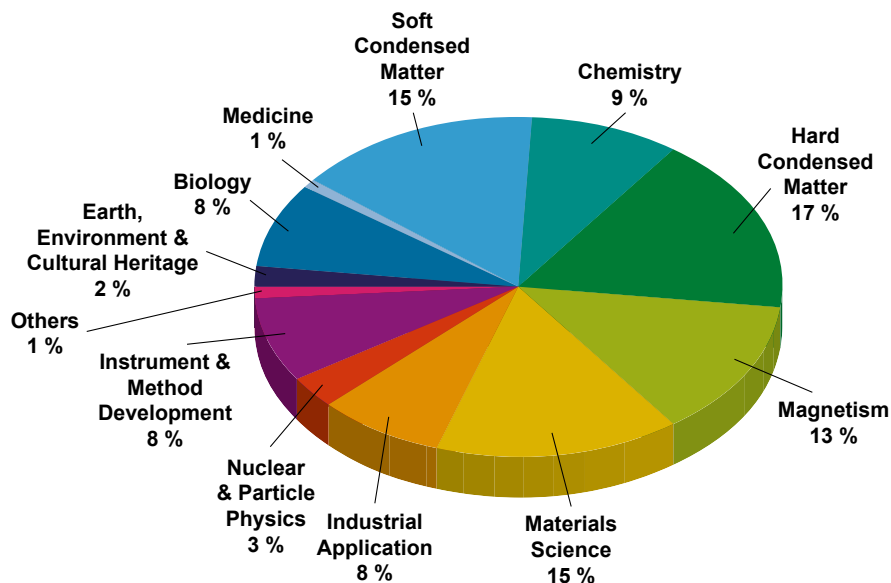
Publications & Theses

In 2016, we received notice of a total of 313 scientific publications, including journal articles, contributions to books and conference proceedings (<https://impulse.mlz-garching.de/> and figure below). Furthermore, in total 46 theses supervised by staff of the scientific cooperation partners were completed in 2016.

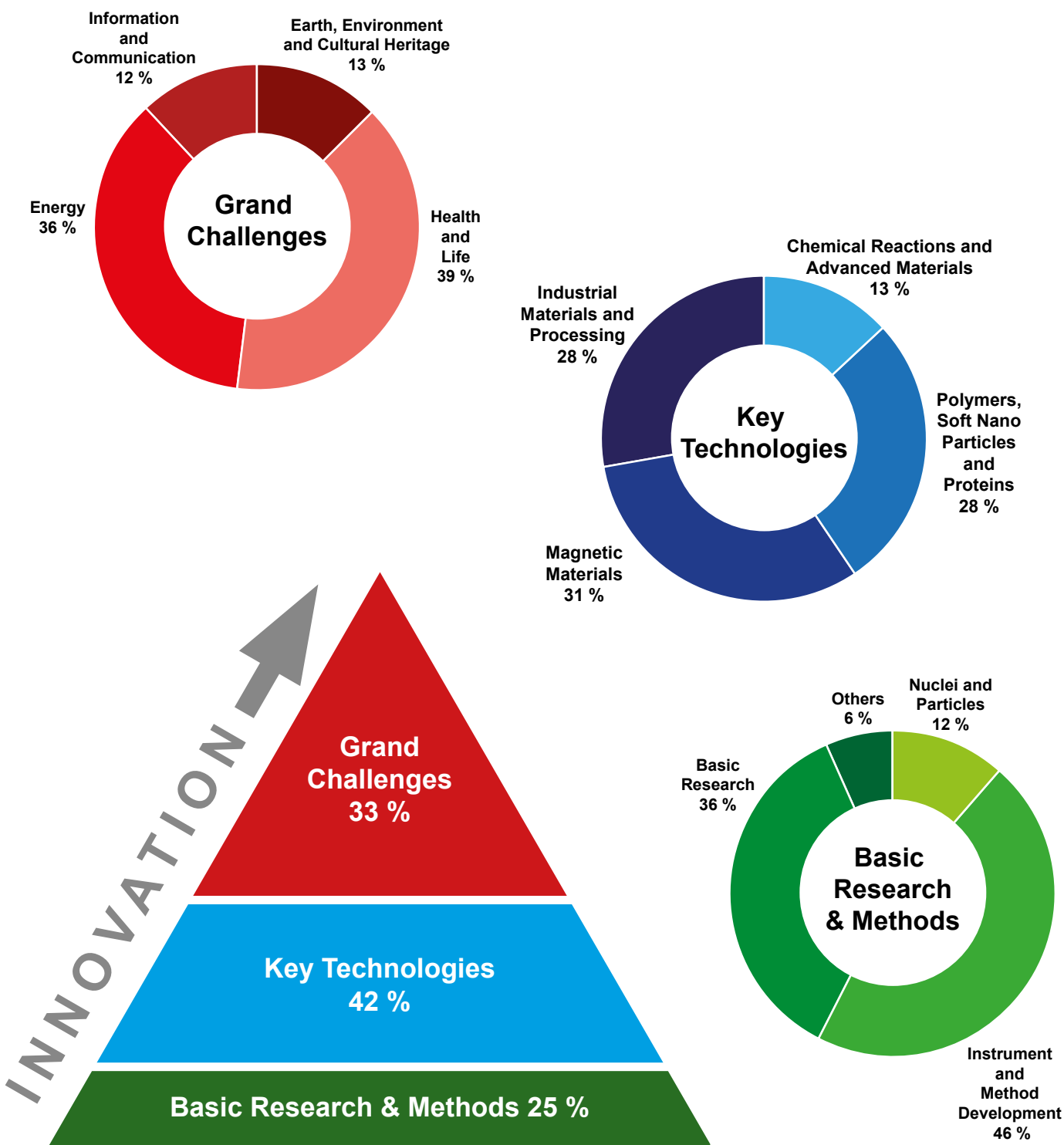
In 2016 more than 220 PhD theses, based on experiments at the MLZ and including external users, were either ongoing or completed. Of these, about 150 are under the direct supervision of staff at the MLZ and its collaboration partners. About 82 % of the doctoral students come from German universities, 16 % come from other universities in Europe and 2 % from the rest of the world.



The next figure shows the classification of the journal articles by Scientific Area (several tags per journal article are possible):



The journal articles at the MLZ can be classified according to a pyramid: from Basic Research & Methods (25 %) required to tackle the Key Technologies (42 %), which address directly the Grand Challenges of our today's society (33 %). The circular charts represent the individual subjects being dealt within these three categories.



Organisation

Steering Committee

Chair

Dr. Ralph Dieter
Federal Ministry of Education and Research

Prof. Dr. Sebastian Schmidt
Board of Directors of Forschungszentrum Jülich GmbH

Members

MRin Dr. Ulrike Kirste (Vice Chair)
Bavarian State Ministry of Education, Science and Arts

Guests

Prof. Dr. Winfried Petry, Scientific Director of the MLZ,
representing TUM

Albert Berger
Senior Executive Vice-President
Technische Universität München

Prof. Dr. Thomas Brückel, Scientific Director of the MLZ,
representing HGF institutions

Thomas Frederking
Member of the Executive Board of
Helmholtz-Zentrum Berlin GmbH

Dr. Anton Kastenmüller
Technical Director ZWE-FRM II,
Technische Universität München

Prof. Dr. Dr. h.c. mult. Wolfgang A. Herrmann
President
Technische Universität München
represented by Prof. Dr. Thomas Hofmann
Vice-President
Technische Universität München

Johannes Nußbickel
Administrative Director ZWE-FRM II,
Technische Universität München

Prof. Dr. Wolfgang Kaysser
Member of the Executive Board of Helmholtz-Zentrum
Geesthacht GmbH

Dr. Klaus Seebach
Former Administrative Director ZWE-FRM II,
Technische Universität München

Prof. Dr. Stephan Paul
Technische Universität München
Physics-Department E18

Dirk Schlotmann
Forschungszentrum Jülich GmbH

RD Petra Lörz
Technische Universität München, ZWE-FRM II



Figure 1: Steering Committee from left to right: K. Seebach, J. Nußbickel, W. Kaysser, S. Paul, Th. Frederking, Th. Hofmann, P. Lörz, A. Berger, R. Dieter, Th. Brückel, U. Kirste, A. Kastenmüller, W. Petry, S. Schmidt, and D. Schlotmann.



Figure 2: Scientific Advisory Board from left to right: A. Blank, J. Rädler, B. Keimer, C. Rüegg, A. Arbe, H. Abele, C. Alba-Simionesco, W. Paul, W. Petry, Th. Brückel, and W. Stirling, as well as the scientists P. Hering and C. Schaffer.

Scientific Advisory Board

Chair

Prof. Christiane Alba-Simionesco
Laboratoire Léon Brillouin,
CEA, Centre de Saclay

Prof. Dr. Wolfgang Paul
Institut für Physik,
Martin-Luther-Universität Halle-Wittenberg

Members

Prof. Dr. Hartmut Abele
Atominstitut der Österreichischen Universitäten
Technische Universität Wien

Prof. Dr. Joachim O. Rädler
Department für Physik
Ludwig-Maximilians-Universität München

Prof. Dr. Arantxa Arbe
Unidad de Física de Materiales
Facultad de Química, San Sebastián

Prof. Dr. Walter Reimers
Institut für Werkstoffwissenschaften und -technologien
Technische Universität Berlin

Alejandro Javier Guirao Blank
Volkswagen AG, Wolfsburg

Prof. Dr. Christian Rüegg
Paul Scherrer Institute, Villigen and University of Geneva

Prof. Dr. Dirk Johrendt
Department Chemie und Biochemie
Ludwig-Maximilians-Universität München

Prof. William Stirling
Institute Laue-Langevin, Grenoble

Prof. Dr. Bernhard Keimer
Max-Planck-Institut für Festkörperforschung, Stuttgart

Prof. Dr. Metin Tolan
Beschleuniger- & Synchrotronlabor
Technische Universität Dortmund



Figure 3: Instrumentation Advisory Committee from left to right: M. Müller, A. Ioffe, M. Diaz, M. Russina, B. Keimer, Th. Brückel, W. Petry, C. Pappas, F. Ott, H. Ronnøw, and J. Neuhaus.

MLZ Instrumentation Committee

Chair

Prof. Dr. Bernhard Keimer
Max-Planck-Institut für Festkörperphysik, Stuttgart

Members

Maria Teresa Fernandez Diaz
Institute Laue Langevin, Grenoble

Dr. Ulli Köster
Institute Laue Langevin, Grenoble

Dr. Eberhard Lehmann
Paul Scherrer Institute, Villigen

Dr. Frédéric Ott, PhD
Laboratoire Léon Brillouin, CEA Saclay

Prof. Dr. Catherine Pappas
Delft University of Technology, Delft

Prof. Dr. Henrik Ronnøw
Ecole Polytechnique Fédérale de Lausanne

Dr. Margarita Russina
Helmholtz-Zentrum Berlin für Materialien
und Energie GmbH

Evaluation of Beam Time Proposals: Members of the Review Panels

Prof. Arantxa Arbe,
Unidad de Fisica de Materiales
Facultad de Quimica, San Sebastián

Dr. Matthew Blakeley
Institut Laue-Langevin (ILL), Grenoble

Dr. Victor Bodnarchuk
Joint Institute for Nuclear Research
Frank Laboratory of Neutron Physics, Dubna

Dr. Laszlo Bottyan
Institute for Particle and Nuclear Physics,
Hungarian Academy of Sciences, Budapest

Prof. Roberto Brusa
Facoltà di Ingegneria, Dipartimento di Fisica
Università degli Studi di Trento

Prof. Dr. Roberto Caciuffo
Institute for Transuranium Elements
Joint Research Center, Karlsruhe

Dr. Monica Ceretti
Institut Charles Gerhardt
Université de Montpellier 2

Dr. Niels Bech Christensen
Institute of Physics
Technical University of Denmark, Roskilde

Dr. Pascale Deen
European Spallation Source (ESS ERIC), Lund

Dr. Sabrina Disch
Department of Chemistry
University of Cologne

Dr. Cecile Dreiss
King's College London

Prof. Dr. Stefan Egelhaaf
Lehrstuhl für Physik der weichen Materie
Heinrich-Heine-Universität Düsseldorf

Prof. Dr. Helmut Ehrenberg
Institut für Angewandte Materialien
Karlsruher Institut für Technologie (KIT), Karlsruhe

Dr. Tom Fennell
Laboratories for Solid State Physics Neutron Scattering
Paul Scherrer Institute, Villigen

Dr. Peter Fouquet
Institut Laue-Langevin (ILL), Grenoble

Dr. Victoria Garcia-Sakai
STFC Rutherford Appleton Laboratory, Didcot

Prof. Giacomo Diego Gatta
Dip. Scienze della Terra „Ardito Desio“
Università degli Studi di Milano



Figure 4: The MLZ Review Panels ready for discussions during their meeting on June 30th and July 01st, 2016.

Prof. Dr. Rupert Gebhard
Abteilung Vorgeschichte
Archäologische Staatssammlung München

Dr. Jens Gibmeier
Institut für Angewandte Materialien,
Karlsruher Institut für Technologie (KIT), Karlsruhe

Dr. Arsène Goukassov
Laboratoire Léon Brillouin
CEA, Centre de Saclay

Dr. Christian Grünzweig
Paul Scherrer Institute, Villigen

Dr. Thomas Hauss
Helmholtz-Zentrum Berlin für Materialien
und Energie GmbH

Prof. Dr. Stephen Hayden
HH Wills Physics Laborator
University of Bristol

Dr. Paul Henry
European Spallation Source (ESS ERIC), Lund

Dr. Klaudia Hradil
Röntgenzentrum
Technische Universität Wien

Dr. Nikolay Kardjilov
Helmholtz-Zentrum Berlin für Materialien
und Energie GmbH

Dr. Reinhard Kremer
Max-Planck-Institut für Festkörperforschung, Stuttgart

Prof. Christian Krempaszky
Fakultät für Maschinenwesen
Technische Universität München

Prof. Jeremy Lakey
Institute for Cell and Molecular Biosciences
University of Newcastle

Prof. Dr. Martin Lerch
Institut für Chemie
Technische Universität Berlin

Dr. Reidar Lund
Department of Chemistry
University of Oslo

Dr. Sandrine Lyonnard
CEA, Grenoble

Prof. Dr. Andreas Magerl
Kristallographie und Strukturphysik
Universität Erlangen-Nürnberg, Erlangen

Dr. Andreas Michels
Faculté des Sciences, de la Technologie et
de la Communication
Université de Luxembourg

Prof. Dr. Peter Müller-Buschbaum
Physik-Department E13
Technische Universität München

Prof. Dr. Tommy Nylander
Physical Chemistry
Lund University



Figure 5: Venue of the MLZ Review Panels' meeting at Munich airport.

Dr. Esko Oksanen
European Spallation Source (ESS ERIC), Lund

Dr. Alessandro Paciaroni
Dipartimento di Fisica
Università degli Studi di Perugia

Prof. Dr. Luigi Paduano
Chemistry Department
University of Naples "Federico II"

Prof. Dr. Oskar Paris
Montanuniversität Leoben

Prof. Dr. Wolfgang Paul
Institut für Physik
Martin-Luther-Universität Halle-Wittenberg

Dr. Oleg Petrenko,
University of Warwick

Dr. Thilo Pirling,
Institut Laue-Langevin (ILL), Grenoble

Dr. Navid Quresh
Institut Laue Langevin (ILL), Grenoble

Dr. Florin Radu
Helmholtz-Zentrum Berlin für Materialien
und Energie GmbH

Dr. Stéphane Raymond
CEA, Centre de Grenoble

Prof. Dr. Günther Redhammer
Materialforschung und Physik
Universität Salzburg

Dr. Sarah Rogers
STFC, Rutherford Appleton Laboratory, Didcot

Dr. Stéphane Rols
Institut Laue-Langevin (ILL), Grenoble

Dr. Matthias Rossbach
Forschungszentrum Jülich GmbH

Dr. Margarita Russina
Institut Weiche Materie und
Funktionale Materialien
Helmholtz-Zentrum Berlin für
Materialien und Energie GmbH

Dr. Michael Sattler
Department Chemie
Technische Universität München

Dr. Harald Schmidt
Institut für Metallurgie
Technische Universität Clausthal

Prof. Dr. Andreas Schönhals
Bundesanstalt für Materialforschung
und -prüfung, Berlin

Dr. Torsten Soldner
Institut Laue-Langevin (ILL), Grenoble

Prof. Dr. Wolfgang Sprengel
Institut für Materialphysik
Technische Universität Graz

Dr. Jochen Stahn
ETH Zürich and Paul Scherrer Institute, Villigen

Dr. Peter Staron
Institute of Materials Research
Helmholtz-Zentrum Geesthacht GmbH

Dr. Ross Stewart
STFC, Rutherford Appleton Laboratory, Didcot

Dr. Oliver Stockert
Max-Planck-Institut für chemische
Physik fester Stoffe, Dresden

Dr. Pavel Strunz
Nuclear Physics Institute, Rez near Prague

Dr. Anne Stunault
Institut Laue-Langevin (ILL), Grenoble

Dr. Laszlo Szentmiklosi
Center for Energy Research, Hungarian
Academy of Science, Budapest

Prof. Kristiaan Temst
Nuclear & Radiation Physics Section
Katholieke Universiteit Leuven

Prof. Dr. Katharina Theis-Broehl
Hochschule Bremenhaven

Prof. Dr. Regine von Klitzing
Institut für Chemie, Stranski-Laboratorium für
Physikalische und Theoretische Chemie
Technische Universität Berlin

Partner institutions

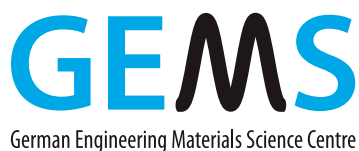


Bayerisches Geoinstitut
 Universität Bayreuth
www.bgi.uni-bayreuth.de



Georg-August-Universität Göttingen

- Institut für Physikalische Chemie
www.uni-pc.gwdg.de/eckold
- Geowissenschaftliches Zentrum
www.uni-goettingen.de/de/125309.html



German Engineering Materials Science Centre GEMS
 Helmholtz-Zentrum Geesthacht GmbH
www.hzg.de/institutes_platforms/gems/



Jülich Centre for Neutron Science JCNS
 Forschungszentrum Jülich GmbH
www.jcns.info



Karlsruher Institut für Technologie

- Institut für Angewandte Materialien –
Energiespeichersysteme (IAM-ESS)
www.iam.kit.edu



Ludwig-Maximilians-Universität München

- Sektion Kristallographie
www.lmu.de/kristallographie
- Fakultät für Physik Physik
www.softmatter.physik.uni-muenchen.de



MAX-PLANCK-GESELLSCHAFT

Max-Planck-Institut für Festkörperforschung, Stuttgart
www.fkf.mpg.de



RWTH Aachen

- Institut für Kristallographie
www.xtal.rwth-aachen.de
- Institut für Anorganische Chemie
www.ac.rwth-aachen.de



Technische Universität Clausthal

- Institut für Werkstoffkunde und Werkstofftechnik
www.iww.tu-clausthal.de



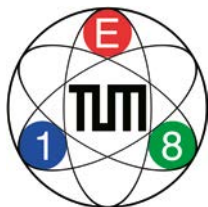
Technische Universität Dresden

- Institut für Festkörperphysik
www.tu-dresden.de/mn/physik/ifp



Technische Universität München

- E13 – Lehrstuhl für Funktionelle Materialien
www.e13.physik.tu-muenchen.de



Technische Universität München

- E18 – Lehrstuhl für Experimentalphysik I
www.e18.ph.tum.de



E21
Arbeitsgebiet stark
korrelierte Elektronensysteme

Technische Universität München

- E21 – Lehrstuhl für Neutronenstreuung
www.e21.ph.tum.de



Technische Universität München

- Exzellenzcluster „Origin and Structure of the Universe“
www.universe-cluster.de



Klinikum rechts der Isar

Technische Universität München

- MRI - Klinikum Rechts der Isar
www.med.tum.de



RCM
Radiochemie München

Technische Universität München

- RCM - Radiochemie München
www.rcm.tum.de



TECHNISCHE
UNIVERSITÄT
WIEN
Vienna University of Technology

Technische Universität Wien

Neutronen- & Quantenphysik

Forschungsbereich am Atominstitut Wien

Arbeitsgruppe Abele

<http://ati.tuwien.ac.at/forschungsbereiche/nqp/home/>

der Bundeswehr
Universität  München

Universität der Bundeswehr München

- Institut für Angewandte Physik und Messtechnik
www.unibw.de/lrt2

Universität zu Köln



Universität zu Köln

- Institut für Kernphysik
www.ikp.uni-koeln.de
- II. Physikalisches Institut
www.ph2.uni-koeln.de

Imprint

Publisher

Technische Universität München
 Forschungs-Neutronenquelle
 Heinz Maier-Leibnitz (FRM II)
 Lichtenbergstr. 1
 85747 Garching
 Germany

Phone: +49.89.289.14966
 Fax: +49.89.289.14995
 Internet: www.mlz-garching.de
 EMail: mlz@mlz-garching.de

Editorial Office, Design and typesetting

Ramona Bucher
 Connie Hesse
 Elisabeth Jörg-Müller
 Christine Kortenbruck
 Andrea Voit

Editors

Henrich Frielinghaus
 Robert Georgii
 Michael Hofmann
 Olaf Holderer
 Peter Link
 Wiebke Lohstroh
 Andreas Ostermann
 Björn Pedersen
 Anatoliy Senyshyn
 Olaf Soltwedel
 Yixi Su

Photographic credits

Wenzel Schürmann, TUM:
 cover back page, 4 (bottom 1st, 3rd and 4th from left), 71, 76, 77 (top and bottom), 83 (bottom), 84 (7, 8, 10, 12), 85 (all pictures), 86 (top), 99

Bernhard Ludewig:
 4 (large image), 9, 47, 79

Wolfgang Filser:
 10 (top and bottom)

Andreas Heddergott, TUM:
 cover front page, 11 (top and bottom), 86 (bottom)

Astrid Eckert, TUM:
 87 (middle)

Tobias Zolles, TU Vienna:
 12 (bottom)

Suzanne Hangx:
 13 (top)

Sebastian Mast:
 10/11 (background), 12/13 (background), 43

Marita Haller:
 80 (middle)

Editors and authors:
 other images



Heinz Maier-Leibnitz Zentrum (MLZ)

www.mlz-garching.de

DOI: 10.14459/2017md1352771

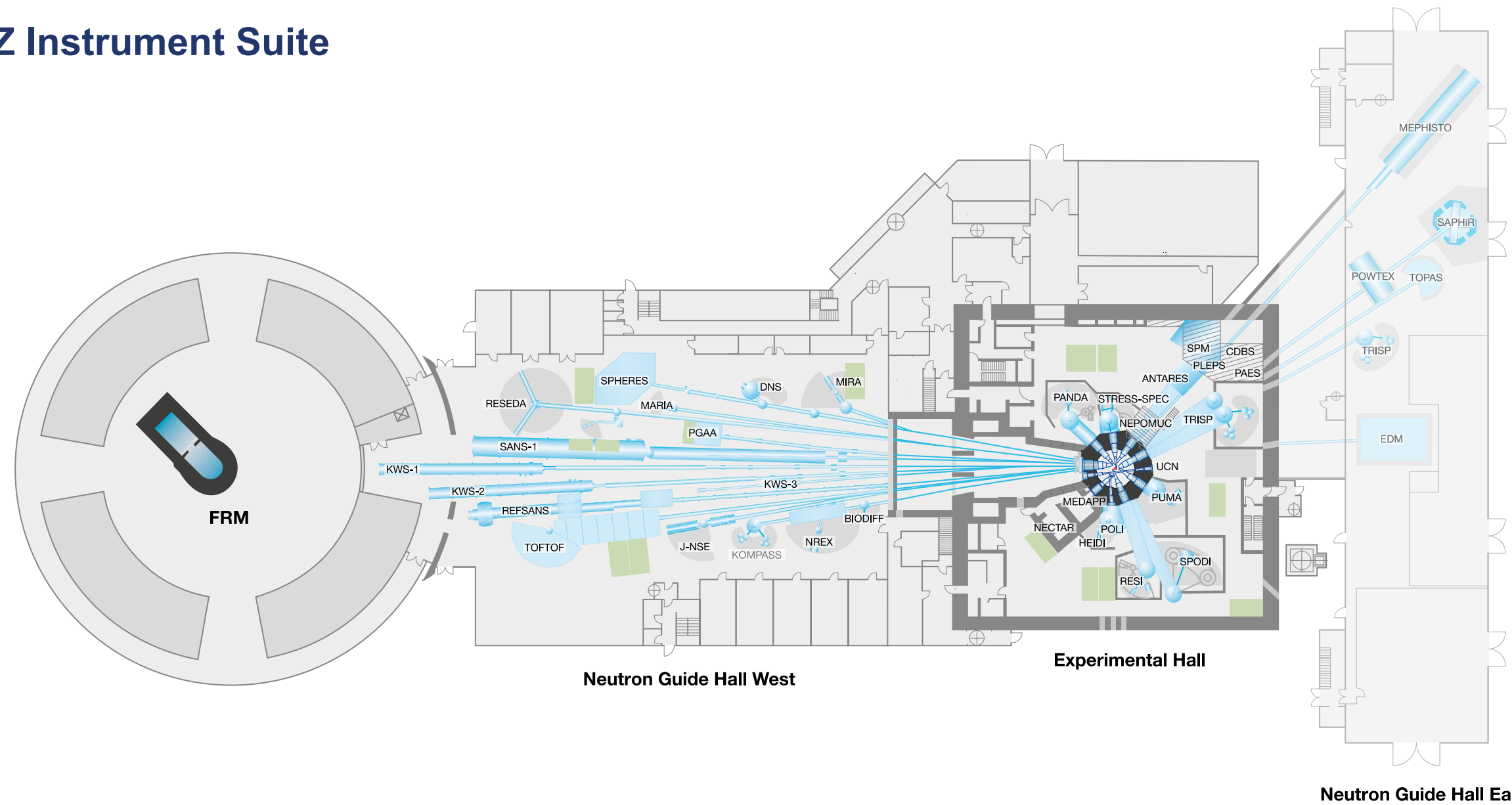
Front page:

Lithium ion cells are one of the big topics in MLZ research in 2016.

Back page:

Construction works for the new center of the campus behind the Atomic Egg.

MLZ Instrument Suite



Instrument	Description	Neutrons	Operated by	Funding	Instrument group at MLZ
ANTARES	Radiography and tomography	cold	TUM	TUM	FRM II
BIODIFF	Diffractionmeter for large unit cells	cold	TUM, JCNS	TUM, FZJ	FRM II, JCNS
DNS	Diffuse scattering spectrometer	cold	JCNS	FZJ	JCNS
HEIDI	Single crystal diffractometer	hot	RWTH Aachen	FZJ	JCNS
J-NSE	Spin-echo spectrometer	cold	JCNS	FZJ	JCNS
KOMPASS*	Three axes spectrometer	cold	Uni Köln, TUM	VF	FRM II
KWS-1	Small angle scattering	cold	JCNS	FZJ	JCNS
KWS-2	Small angle scattering	cold	JCNS	FZJ	JCNS
KWS-3	Very small angle scattering	cold	JCNS	FZJ	JCNS
MARIA	Magnetic reflectometer	cold	JCNS	FZJ	JCNS
MEPHISTO**	Instrument for particle physics, PERC	cold	TUM	TUM, DFG	FRM II
MIRA	Multipurpose instrument	cold	TUM	TUM	FRM II
MEDAPP	Medical irradiation treatment	fast	TUM	TUM	FRM II
NECTAR	Radiography and tomography	fast	TUM	TUM	FRM II
NEPOMUC	Positron source, CDBS, PAES, PLEPS, SPM	-	TUM, UniBw München	TUM	FRM II
NREX	Reflectometer with X-ray option	cold	MPI Stuttgart	MPG	MPI Stuttgart
PANDA	Three axes spectrometer	cold	JCNS	FZJ	JCNS

Instrument	Description	Neutrons	Operated by	Funding	Instrument group at MLZ
PGAA	Prompt gamma activation analysis	cold	Uni Köln	TUM	FRM II
PUMA	Three axes spectrometer	thermal	Uni Göttingen, TUM	VF, TUM	FRM II
POLI	Single-crystal diffractometer polarized neutrons	hot	RWTH Aachen	VF, FZJ	JCNS
POWTEX*	Time-of-flight diffractometer	thermal	RWTH Aachen, Uni Göttingen, JCNS	VF, FZJ	JCNS
REFSANS	Reflectometer	cold	GEMS	VF, HZG	GEMS
RESEDA	Resonance spin-echo spectrometer	cold	TUM	TUM	FRM II
RESI	Single crystal diffractometer	thermal	LMU	TUM	FRM II
SANS-1	Small angle scattering	cold	TUM, GEMS	TUM, HZG	FRM II, GEMS
SAPHIR*	Six anvil press for radiography and diffraction	thermal	Uni Bayreuth	VF	FRM II
SPHERES	Backscattering spectrometer	cold	JCNS	VF, FZJ	JCNS
SPODI	Powder diffractometer	thermal	KIT	VF, TUM	FRM II
STRESS-SPEC	Materials science diffractometer	thermal	TUM, TU Clausthal, GEMS	TUM, HZG	FRM II, GEMS
TOFTOF	Time-of-flight spectrometer	cold	TUM	TUM	FRM II
TOPAS*	Time-of-flight spectrometer	thermal	JCNS	FZJ	JCNS
TRISP	Three axes spin-echo spectrometer	thermal	MPI Stuttgart	MPG	MPI Stuttgart
UCN*	Ultra cold neutron source, EDM	ultra-cold	TUM	TUM, DFG	FRM II

*construction
 **reconstruction
 VF: instrument construction funded by "BMBF-Verbundforschung" (Collaborative Projects)